



HAL
open science

Modelling of multi-electronic processes occurring during atomic collisions

Stylianos Passalidis

► **To cite this version:**

Stylianos Passalidis. Modelling of multi-electronic processes occurring during atomic collisions. Chemical Physics [physics.chem-ph]. Sorbonne Université, 2022. English. NNT : 2022SORUS017. tel-03622169

HAL Id: tel-03622169

<https://theses.hal.science/tel-03622169>

Submitted on 28 Mar 2022

HAL is a multi-disciplinary open access archive for the deposit and dissemination of scientific research documents, whether they are published or not. The documents may come from teaching and research institutions in France or abroad, or from public or private research centers.

L'archive ouverte pluridisciplinaire **HAL**, est destinée au dépôt et à la diffusion de documents scientifiques de niveau recherche, publiés ou non, émanant des établissements d'enseignement et de recherche français ou étrangers, des laboratoires publics ou privés.



SORBONNE UNIVERSITÉ

THÈSE

Modélisation de processus
multielectroniques au cours de
collisions atomiques

par

Stylios PASSALIDIS

pour obtenir le grade de

Docteur de l'université Sorbonne Université

Laboratoire de Chimie Physique-Matière et Rayonnement

École doctorale 388: Chimie Physique et Chimie Analytique de

Paris Centre

soutenue le 27 janvier 2022

devant le jury composé de:

| | |
|--|--------------------|
| M. Bernard PONS, Université de Bordeaux | Rapporteur |
| M. Emmanouil P. BENIS, University of Ioannina | Rapporteur |
| Mme. Emily LAMOUR, Sorbonne Université | Présidente |
| Mme. Eleonora LUPPI, Sorbonne Université | Examinatrice |
| M. Amine CASSIMI, Université de Caen Normandie - CEA | Examinateur |
| M. Alain DUBOIS, Sorbonne Université | Directeur de thèse |



SORBONNE UNIVERSITÉ

THESIS

Modelling of multi-electronic
processes occurring during
atomic collisions

by

Stylios PASSALIDIS

*submitted in fulfilment of the requirements for the degree of
Doctor of Sorbonne Université*

Laboratoire de Chimie Physique-Matière et Rayonnement
École doctorale 388: Chimie Physique et Chimie Analytique de
Paris Centre

defended on 27 January 2022

in front of the jury composed by:

| | |
|--|--------------------|
| M. Bernard PONS, Université de Bordeaux | Reporter |
| M. Emmanouil P. BENIS, University of Ioannina | Reporter |
| Mme. Emily LAMOUR, Sorbonne Université | President |
| Mme. Eleonora LUPPI, Sorbonne Université | Examiner |
| M. Amine CASSIMI, Université de Caen Normandie - CEA | Examiner |
| M. Alain DUBOIS, Sorbonne Université | Director of thesis |

In memory of
Thanos Tazes

Acknowledgements

First and foremost I would like to thank my advisor Alain who has guided me for the last three years with great patience. I would like to thank him for insisting on scientific and pedagogic details which I would never observe by myself and keeping me constantly alert and motivated. Thank you for everything you have taught me and the new way, to approach research and science, you have provided me.

Additionally, I would like to thank Richard and Stéphane for all their advices and mostly the small talks we have had during the many beers we drunk in and outside the lab. Moreover I want to thank Jérémie and Camille for our fruitful discussions and their encouraging and last but not least, David, without whom LCPMR might not exist, for the time he allotted.

A huge thanks to the friends I made here in Paris, especially to Anthi, Manos, Sofia and Giorgos. A special acknowledgement to my friends and colleagues Basile and Anthony for the discussions and mostly the relaxing time we have had during the last three years. Nevertheless I would like to thank for all the fruitful and relaxing time spent with Selma, Tsveta, Lucia, Bastien, Valentin, Hina, Sonia, Pierre-Louis and all the students that passed by Bureau 111 during the last years.

A special thank-you to Mina for her patience and the encouraging as well as to Mary, Stavros, Maria and Anna for all the moments, happy and difficult, we have shared in rue des Couronnes alongside our flat.

Finally, I want to express my huge gratitude to my mom Ntina, my dad Yannis and my brother Stathis for their timeless and endless support during all these years in any way as well as their patience for the quite many times I've been crabby.

SORBONNE UNIVERSITÉ

Résumé

Faculté des Sciences et Ingénierie

École doctorale 388: Chimie Physique et Chimie Analytique de Paris Centre

Doctorat

Modélisation de processus multielectroniques au cours de collisions atomiques

Les processus électroniques se produisant lors des collisions entre atomes et molécules, neutres ou ionisées sont, d'une part, des événements intéressants à l'échelle atomique, mais jouent également un rôle important dans la dynamique de nombreux milieux complexes, comme, par exemple, les plasmas froids ou chauds (oxydation, fusion thermonucléaire magnétique). Bien que ces processus soient maintenant bien compris et modélisés lorsqu'ils impliquent un seul électron actif, ce n'est pas le cas pour les transitions impliquant plusieurs électrons actifs ou lorsque les corrélations électroniques statiques et dynamiques jouent un rôle important. Pour interpréter les résultats des expériences de diffusion en laboratoire et fournir des données atomiques pertinentes pour la modélisation et le diagnostic des milieux complexes mentionnés ci-dessus, il est important de développer des méthodes et des codes permettant de calculer les sections efficaces des processus électroniques susceptibles de se produire dans des conditions données. Ces sections efficaces dépendent fortement de la vitesse relative entre les partenaires de la collision. On peut classer les collisions en trois "régimes" en fonction du rapport entre la vitesse du projectile v_P et la vitesse classique v_e des électrons actifs situés sur la cible. Le domaine intermédiaire correspond à un rapport $v_P/v_e \approx 1$ et concerne le domaine le plus complexe à étudier car tous les processus sont quasi équiprobables et couplés entre eux. Les études dans ce régime de vitesse nécessitent des traitements non perturbatifs très lourds en ressources informatiques. C'est le domaine dans lequel se situe notre travail.

De nos jours, les processus à 1 électron actif, tels que la capture, l'excitation et l'ionisation d'un unique électron, peuvent être considérés comme bien compris et modélisés pour les systèmes à un (et quasi un) électron (par exemple $H^+ - H(1s)$, $H^+ - Na(3s)$). Au contraire, ceci n'est pas le cas pour les transitions impliquant plusieurs électrons actifs et quand les corrélations électroniques statiques et dynamiques jouent un rôle crucial. Dans de tels systèmes, il est probable que i) un grand nombre de canaux soient couplés et ii) la corrélation électronique joue un rôle important, de sorte que l'utilisation de l'approximation des électrons indépendants est exclue. La compréhension et la modélisation des processus de collision impliquant de multiples électrons actifs constituent donc toujours un défi. En particulier, dans la région d'énergie d'impact intermédiaire, où les approches perturbatives ne peuvent pas être utilisées pour décrire la physique sous-jacente en raison des couplages forts entre les divers canaux ouverts et les effets de corrélation électronique. Par conséquent, des approches semi-classiques, non perturbatives et multi-électroniques restent nécessaires.

Dans le cadre de cette thèse, nous appliquons une approche semiclassique non perturbative pour décrire les processus multi-électroniques se produisant lors de collisions ion-atome non-relativistes. Le traitement est semiclassique dans la mesure où le mouvement relatif cible-projectile est décrit classiquement par des trajectoires rectilignes uniformes. En revanche, la dynamique électronique est traitée de manière quantique, en résolvant de manière non perturbative l'équation de Schrödinger dépendant du temps (TDSE). Dans notre équipe, plusieurs codes ont été développés pour résoudre la TDSE. Leur utilisation a été fortement axée sur la prise en compte d'un très grand nombre de canaux ainsi que de tous les couplages entre ces derniers. Ces codes correspondent à plusieurs milliers de lignes écrites en Fortran et peuvent être appliqués pour de nombreux systèmes de collisions. Ils sont également les seuls à pouvoir traiter des systèmes de collisions jusqu'à quasi quatre électrons actifs. Au cours de ce travail, nous avons étudié plusieurs systèmes de collision au regard de certains

besoins en diagnostic de plasma (collision $\text{Li}^{2+} - \text{H}$) et en relation avec des investigations expérimentales très récentes (collisions ions héliumoïdes C^{4+} , O^{6+} , F^{7+} -He et collisions C^{3+} -He). En parallèle, nous avons développé un code permettant de construire les états électroniques à inclure dans le code de collision, car cette étape préalable est extrêmement importante pour décrire au mieux les systèmes considérés mais aussi pour optimiser les calculs qui sont extrêmement consommateurs en CPU et en mémoire.

Dans le chapitre 2, le contexte théorique de l'approche semiclassique utilisée est brièvement présenté. Elle aboutit à la TDSE, également appelée équation eikonale dans ce contexte. Suit la description de la méthode semi-analytique adoptée pour résoudre la TDSE et qui aboutit à un ensemble d'équations différentielles couplées à résoudre numériquement. Nous décrivons ensuite les orbitales de type gaussiens (GTO) que nous adoptons pour développer la fonction d'onde totale, ainsi que l'algorithme utilisé pour optimiser ces bases.

Dans le chapitre 3, la capture et l'excitation ont été étudiées dans les collisions $\text{Li}^{2+} - \text{H}(1s)$ en utilisant l'approche SCAOCC à deux électrons actifs présentée dans le chapitre 2. L'utilisation de grandes bases, permettant l'évaluation de sections efficaces, totales et sélectives par état, bien convergées, est présentée dans un large domaine d'énergie, 0,1- 250 keV/u. Les résultats actuels sont en accord avec les données expérimentales et les calculs théoriques précédemment disponibles dans leur domaine d'énergie respectif. Notre étude étend les calculs aux énergies d'impact aussi basses que 0,1 keV/u où l'on observe que la capture à $n=2$ domine et détermine la section efficace totale de capture. Les résultats pour les différentes sous-couches montrent que les états triplets deviennent dominants avec une section efficace jusqu'à plus de mille fois plus grande que les états singulets pour la capture, à la fois sur les couches $n=2$ et $n=3$. Des calculs indépendants et des travaux expérimentaux seraient utiles pour valider les sections efficaces calculées dans cette gamme d'énergie. De plus, nous avons étudié l'effet d'asymétrie de spin que nous avons découvert pour le

transfert vers les états P et non présents pour les états S et D . Un modèle type Oppenheimer-Brinkman-Kramers (OBK) a été développé pour les besoins de la compréhension de ces effets pour des vitesses élevées. Des calculs supplémentaires pour différents projectiles hydrogénoïdes présentent la même asymétrie de spin, qui semble donc de nature générale et non accidentelle. Cette série de résultats valide le modèle OBK développé au cours de cette thèse, validant l'interaction entre le couplage à deux électrons et à deux centres, qui explique l'asymétrie, et le couplage direct, qui implique la modification du projectile.

Dans le chapitre 4, nous avons étudié les processus mono- et bi-électroniques, à savoir la simple capture et le transfert-excitation qui se produit dans des collisions entre des ions héliumoïdes ($Z_P = 6, 8$ et 9) et des atomes d'hélium aux énergies d'impact de l'ordre du 1 MeV/u . Plus précisément, nous avons principalement étudié la production d'états doublement excités $1s2l2l' \ ^{2S+1}L$ après le transfert d'un électron de la cible au projectile initialement dans l'état fondamental $1s^2 \ ^1S$ ou dans des états métastables $1s2s \ ^1,^3S$. Ces derniers ont été étudiés en relation avec des études expérimentales réalisées à l'aide d'un spectromètre d'électron Auger à 0° installé dans les installations de l'accélérateur Demokritos en Grèce. L'originalité et la complexité de ce travail sont liées à la description théorique de systèmes comportant jusqu'à trois sous couches ouvertes, ce qui entraîne la présence d'un grand nombre de niveaux d'énergie et la nécessité d'utiliser un traitement non monoélectronique. Dans ce but, nous avons utilisé une approche de close coupling avec trois électrons actifs pour décrire, aussi bien que possible, les états des projectiles considérés. Nous avons analysé la dépendance en énergie des sections efficaces de plusieurs de ces états doublement excités pour différents ions projectiles et extrait les mécanismes responsables de ces processus. En particulier, la production par excitation-transfert d'états $1s2p^2 \ ^2D$ à partir de l'état fondamental du projectile a été étudiée de manière très détaillée, en comparant les résultats de calculs étendus avec ceux à bases limitées, incluant tous les couplages entre les états ou

négligeant certains d'entre eux, notamment les interactions électron-électron à deux centres.

Pour la première fois, nous avons été en mesure de valider, avec un traitement *ab-initio*, le processus de transfert-excitation résonant, caractérisé par un pic net dans les spectres et modélisé par le passé par un processus Auger inverse. Une seconde structure apparaissant à des énergies d'impact plus faibles et interprétée qualitativement comme des processus de transfert et d'excitation successifs et indépendants a été observée dans nos résultats, mais ce modèle a été rejeté au profit d'un mécanisme corrélé complexe uniquement observable dans les calculs non perturbatifs. Ces derniers ont clairement été montrés comme étant essentiels pour décrire la dynamique de ces systèmes de collision malgré le domaine de haute énergie considéré.

Finalement, nous avons obtenu un bon accord avec les données expérimentales disponibles, en particulier pour le projectile de carbone, mais, pour le fluor, la comparaison était moins pertinente puisque dans l'étude expérimentale relativement ancienne, la composition des faisceaux n'était pas clairement définie. Les résultats pour l'oxygène ont été présentés pour une comparaison future avec une campagne de mesures et d'analyse des données en cours.

Dans le chapitre 5 les processus de transfert-excitation et transfert simple ont été étudiés pour les collisions $C^{3+} - He$ dans une large gamme d'énergie, couvrant les régimes bas, intermédiaire et haut. Les sections efficaces relatives pour la production d'états $C^{2+}(1s^2 2l 2l')$ sont en excellent accord avec des données expérimentales très récentes, alors que des études théoriques précédemment publiées ne permettent pas de reproduire les résultats expérimentaux. En se concentrant sur les deux états de capture les plus importants $C^{2+}(1s^2 2s 2p \ ^{1,3}P)$, le rapport des sections efficaces $R = \ ^3P / \ ^1P$ s'est avéré augmenter d'environ 0,5 à environ 3,6 pour des énergies croissantes, en accord presque parfait avec les résultats de l'équipe de Lanzhou jusqu'à 50 keV/u, au-delà duquel l'expérience n'a pas pu être réalisée. Les calculs restreints à 2 électrons ne donnent pas

des résultats similaires dans tout le domaine d'énergie considéré, montrant la nécessité d'inclure les deux électrons sur la cible He et l'échec de l'approximation du cœur gelé lorsqu'on se concentre sur des observables très détaillés, comme le rapport R .

En considérant l'avenir du présent travail, on peut imaginer plusieurs voies de développements intéressants. En premier lieu, l'achèvement de certaines des investigations présentées dans cette thèse et qui ont été développées dans le cadre de collaborations avec des expérimentateurs. En effet, il existe encore quelques défis et points d'interrogation dans les études des chapitres 4 et 5. Il est nécessaire d'aborder d'autres systèmes et d'autres processus de collision pour généraliser les conclusions tirées des travaux actuels, ainsi que qu'approfondir nos connaissances des processus mis en jeu. Les expériences qui ont toujours le dernier mot sont très importantes dans ce contexte. Dans un deuxième temps, un effort important devrait être fait pour optimiser le code encore mieux qu'il ne l'est actuellement. En effet, les calculs que nous avons présentés dans cette thèse représentent plusieurs dizaines de milliers d'heures de calcul (sur des stations de travail à 56 threads). L'optimisation de parties spécifiques du code (en utilisant des GPU par exemple), ainsi que l'optimisation de la stratégie de parallélisation utilisée dans la version actuelle, seraient d'un grand intérêt. Une deuxième direction d'optimisation, très importante, correspond à la description des états impliqués dans la dynamique : cela peut être fait en codant l'automatisation de l'optimisation des bases GTO, pour obtenir de meilleurs états propres et valeurs propres avec un plus petit nombre d'orbitales. En effet, les ressources informatiques (CPU et mémoire) nécessaires pour effectuer les calculs suivent approximativement une loi en N^n , où N est le nombre de GTO et n le nombre d'électrons actifs, ce qui rend assez difficile l'extension du code aux systèmes comportant plus de 4 électrons. Le développement du code dans cette direction est un défi et impose des recherches supplémentaires sur de nouvelles approches mathématiques et de programmation.

A moyen et long terme, l'avenir des développements théoriques en physique atomique et moléculaire et en chimie physique, concerne les domaines d'application dans lesquels les collisions jouent un rôle essentiel. Les systèmes de collision concernant principalement les sciences de la vie et la production d'énergie propre seront à coup sûr les plus intéressants. Cela nécessite la description de systèmes neutres ou ionisés multi-électroniques et multicentriques en interaction avec des perturbations fortes et rapides, également intégrés dans des environnements spécifiques. En ce qui concerne les sciences de la vie, des progrès significatifs doivent être réalisés dans la description des processus électroniques impliquant des molécules, et en particulier la molécule d'eau qui constitue plus de 70% de la masse corporelle humaine. Concernant les dispositifs à plasma de fusion, une nouvelle direction intéressante serait d'incorporer un environnement magnétique (mais aussi électrique) dans lequel les collisions ont lieu dans ces systèmes complexes. Dans ce contexte, mais aussi à des fins plus générales concernant les atomes et les ions lourds, l'inclusion du couplage spin-orbite sera un défi en physique des collisions ion-atome/molécule. Enfin, n'oublions pas que pour pouvoir traiter des systèmes aussi complexes, il faut des approximations et des modèles. Le développement et le test de ces derniers sur des systèmes de collision de référence "simples" sont très intéressants et constituent toujours des perspectives originales de recherche fondamentale.

Contents

| | |
|--|-------------|
| Acknowledgements | v |
| Résumé | vii |
| List of Figures | xvii |
| List of Tables | xxi |
| 1 Introduction | 1 |
| 2 The non perturbative semiclassical atomic orbital close-coupling approach | 11 |
| 2.1 Introduction | 11 |
| 2.2 Impact parameter method - The eikonal equation | 12 |
| 2.3 Solution of the eikonal equation in Hilbert space | 16 |
| 2.3.1 The electronic wave function | 17 |
| 2.3.2 The coupled differential equation system | 19 |
| 2.4 Implementation | 22 |
| 2.4.1 Gaussian Type Orbitals (GTO) | 23 |
| 2.4.2 The evaluation of one- and two-electron integrals | 27 |
| 2.4.3 The solution of the ODEs | 28 |
| 3 Li^{2+} - H collisions: State selective cross sections and spin effects | 29 |
| 3.1 Introduction | 29 |
| 3.2 Calculation details | 30 |
| 3.3 Results and discussion | 32 |
| 3.3.1 Electron capture | 32 |
| 3.3.2 Spin anisotropy effect | 41 |
| 3.3.3 Electron excitation | 51 |
| 3.4 Conclusion | 53 |

| | | |
|----------|---|------------|
| 4 | Multielectronic processes in helium-like ion – He collisions | 55 |
| 4.1 | Introduction | 55 |
| 4.2 | Transfer-Excitation | 56 |
| 4.2.1 | Resonant Transfer-Excitation | 58 |
| 4.2.2 | Non-Resonant Transfer-Excitation | 59 |
| 4.3 | The C^{4+} - He collision system | 59 |
| 4.3.1 | Calculation details | 60 |
| 4.3.2 | Results and discussion | 62 |
| 4.4 | The F^{7+} - He collision system | 77 |
| 4.4.1 | Calculation details | 78 |
| 4.4.2 | Results and discussion | 79 |
| 4.5 | The O^{6+} - He collision system | 88 |
| 4.5.1 | Calculation details | 88 |
| 4.5.2 | Results and discussion | 89 |
| 4.5.3 | Projectile excitation to $2s2p\ ^{1,3}P$ | 92 |
| 4.6 | Conclusion | 95 |
| 5 | C^{3+} - He collisions: State selective cross sections at low and intermediate energies | 97 |
| 5.1 | Introduction | 97 |
| 5.2 | Calculation details | 98 |
| 5.3 | Results and discussion | 99 |
| 5.3.1 | Single electron transfer & transfer-excitation cross sections | 99 |
| 5.3.2 | Spin statistics on production of $C^{2+}(1s^22s2p\ ^{1,3}P)$ | 101 |
| 5.3.3 | Two-electron versus three-electron close-coupling approach | 104 |
| 5.4 | Conclusion | 108 |
| 6 | Conclusions and future work | 111 |
| | Appendices | 115 |
| A | Gaussian Type Orbitals basis sets | 117 |
| A.1 | Li^{2+} - H collision system | 117 |
| A.2 | Z^{Z-1} - H collision systems (spin effect study) | 119 |
| A.3 | C^{4+} - He collision system | 120 |
| A.4 | F^{7+} - He collision system | 121 |
| A.5 | O^{6+} - He collision system | 122 |
| A.6 | C^{3+} - He collision system | 123 |
| | Bibliography | 125 |

List of Figures

| | | |
|------|--|----|
| 1.1 | The Bragg Peak | 3 |
| 1.2 | Magnetic plasma confinement, edge region | 5 |
| 1.3 | Inertial confinement fusion scheme | 5 |
| 1.4 | Approaches of ion-atom collision study depending on the collision energy | 6 |
| 2.1 | Geometry of the ion-atom and ion-molecule collision | 15 |
| 2.2 | Asymptotic state energies optimisation | 27 |
| 3.1 | Convergence test for the five different basis sets: total electron capture of the Li^+ ion | 31 |
| 3.2 | Total electron capture in Li^{2+} - $\text{H}(1s)$ collision. | 33 |
| 3.3 | Partial cross sections for electron capture to $1s2l$ in the Li^{2+} - $\text{H}(1s)$ collision. | 34 |
| 3.4 | Sub-shell selective cross sections for electron capture to $1sn = 2$, (a) $l = 0$ and (b) $l = 1$ in Li^{2+} - $\text{H}(1s)$ collision. | 36 |
| 3.5 | Adiabatic potential curves of LiH^{2+} for (a) singlet states and (b) triplet states. Figure taken by Yan et al. [78] | 37 |
| 3.6 | The reduced probabilities $bP(b)$ for the production of (a) $\text{Li}^+(1s2s\ ^3S)$ and (b) $\text{Li}^+(1s2p\ ^3P)$ at 0.2 keV/u. | 38 |
| 3.7 | Sub-shell selective cross sections for electron capture to $1sn = 3$, (a) $l = 0$, (b) $l = 1$ and (c) $l = 2$ in Li^{2+} - $\text{H}(1s)$ collision. | 40 |
| 3.8 | Geometry of the ion-atom and ion-molecule collision | 45 |
| 3.9 | The $^3L/1L$ cross sections for production of $1s2l$ configuration in He^+ , Li^{2+} , B^{4+} , C^{5+} colliding with H. | 50 |
| 3.10 | The $^3L/1L$ cross sections for production of $1s3l$ configuration in He^+ , Li^{2+} , B^{4+} , C^{5+} colliding with H. | 51 |
| 3.11 | Shell selective cross sections for excitation of the H atom in the Li^{2+} - $\text{H}(1s)$ collision system systems. | 52 |
| 4.1 | Schematic representation of NTE process. | 58 |
| 4.2 | Schematic representation of NTE process. | 59 |

| | | |
|------|---|----|
| 4.3 | Cross sections of the production of the $1s2s\ ^2S$ for three initial C^{4+} states. | 63 |
| 4.4 | Cross sections for the production of the $C^{3+}(1s2s2p\ ^2P_+)$ (left panels) and $^2P_-$ (right panels) for the three projectile initial states. | 64 |
| 4.5 | $C^{3+}\ 1s2s2p\ ^4P$ formation | 65 |
| 4.6 | $C^{3+}\ bP(b)$ dependence | 66 |
| 4.7 | Cross sections for the production of the $1s2p^2\ ^2D$ state as function of energy for the three initial C^{4+} states. | 68 |
| 4.8 | Waterfall 3D plot of $C^{3+}\ 1s2p^2\ ^2D$ alongside with the impact parameter-weightened probabilities $bP(b)$ | 69 |
| 4.9 | The energy dependence of $C^{3+}(1s2p^2\ ^2D)$ M_L -resolved cross sections for the $1s^2\ ^1S$ projectile initial state. | 70 |
| 4.10 | SDSC for $C^{3+}\ 1s2p^2\ ^2D$ | 71 |
| 4.11 | 2-level CC calculations: cross sections of production of the $1s2p^2\ ^2D$ states in $C^{4+}(1s^2\ ^1S)$ - He collisions. | 72 |
| 4.12 | Cross sections for the production of the $1s2p^2\ ^2D$ states as function of impact energy | 73 |
| 4.13 | Impact parameter-weightened probabilities $bP(b)$ of $1s2p^2\ ^2D$ production by $1s^2\ ^1S$ for full CC, 2-level CC and 2-level CC without TCee | 75 |
| 4.14 | The $C^{3+}\ 1s2p^2\ ^2P$ formation | 76 |
| 4.15 | Cross sections of production of the $1s2p^2\ ^2P$ states, using the full close-coupling and the 2-level calculations. | 76 |
| 4.16 | Impact parameter-weightened probabilities $bP(b)$ of $1s2p^2\ ^2P$ production by $1s^2\ ^1S$ for full CC, 2-level CC and 2-level CC without TCee | 77 |
| 4.17 | Convergence of the cross sections of 5 typical channels ($1s2s^2\ ^2S$, $1s2s2p\ ^2P_{\pm}$ and 4P and $1s2p^2\ ^2D$) for two F^{7+} initial states $1s^2\ ^1S$ and $1s2s\ ^3S$ | 80 |
| 4.18 | The Auger SDCS for the four states (a) $1s2p^2\ ^2D$, (b), (c) $1s2s2p\ ^2P_{\pm}$ and (d) $1s2s^2\ ^2S$ | 81 |
| 4.19 | Total cross sections of production of the $F^{6+}\ 1s2s^2\ ^2S$ | 82 |
| 4.20 | Cross sections for the production of the $F^{6+}\ 1s2s2p\ ^2P_{\pm}$ | 83 |
| 4.21 | Cross sections for the production of the quartet state $1s2s2p\ ^4P$ by capture from the $F^{7+}(1s2s\ ^3S)$ initial states. | 84 |
| 4.22 | Cross sections for the production of the $1s2p^2\ ^2D$ state as function of energy for the three initial F^{7+} states. | 84 |

| | | |
|------|--|-----|
| 4.23 | The energy dependence of $F^{6+}(1s2p^2\ ^2D)$ M_L -resolved cross sections for the $1s^2\ ^1S$ projectile ground state. | 85 |
| 4.24 | Cross sections of production of $1s2p^2\ ^2D$ and its $M_L = 0$ component as function of impact energy. | 86 |
| 4.25 | $O^{5+}\ 1s2s^2\ ^2S$ formation | 90 |
| 4.26 | $O^{5+}\ 1s2s2p\ ^2P_{\pm}$ formation | 91 |
| 4.27 | Cross sections of production of the quartet state $1s2s2p\ ^4P$ by capture from the $O^{6+}(1s2s\ ^3S)$ initial state. | 92 |
| 4.28 | Cross sections for the production of the $1s2p^2\ ^2D$ state as function of energy for the three initial O^{6+} states. | 93 |
| 4.29 | The energy dependence of $O^{5+}(1s2p^2\ ^2D)$ M_L -resolved cross sections for the $1s^2\ ^1S$ projectile ground state. | 93 |
| 4.30 | Cross sections of the production of the (a) $2s2p\ ^1P$ and (b) $2s2p\ ^3P$ doubly excited states. | 95 |
| 5.1 | Normalised cross sections for the production of $C^{2+}(1s^22l2l'\ ^1,3L)$ states as function of impact energy. | 100 |
| 5.2 | Triplet over singlet ratio R of SEC to $1s^22s2p\ ^1,3P$ in $CC^{3+} + He$ collision system. | 103 |
| 5.3 | CHe^{3+} adiabatic Σ energy curves (from Figure 1(a) in Wu et al [142]). | 104 |
| 5.4 | The reduced probabilities $bP(b)$ for the production of $C^{2+}(1s^22s2p\ ^1P)$ and $C^{2+}(1s^22s2p\ ^3P)$ in light blue and green lines, respectively, at impact energies (a) 0.5 keV/u, (b) 1.25 keV/u, (c) 2 keV/u and (d) 25 keV/u. | 105 |
| 5.5 | Comparison of the normalised cross sections as in Figure 5.1 with the ones calculated with the 2-electron approach. | 106 |
| 5.6 | Ratio $R = ^3P/^1P$ of the cross sections of production of $C^{2+}(1s^22s2p\ ^1,3P)$ as function of energy. | 108 |

List of Tables

| | | |
|-----|---|-----|
| 3.1 | Comparison of energies, in a.u., of the Li^+ ion, singlet (left) and triplet (right) states, calculated based on the GTO basis set and the NIST data using $B_1^{H,Li}$ | 30 |
| 3.2 | Comparison of energies, in a.u., of the He atom, B^{3+} and C^{4+} ions, triplet and singlet states, based on the GTO basis set. We include the NIST data for comparison. | 49 |
| 4.1 | Coefficients and exponents used to represent the system $\text{He}^+ - e^-$ by the model potential eq. 4.6 | 61 |
| 4.2 | Comparison of energies, in a.u., of the C^{3+} and C^{4+} , based on the GTO basis set and the available data [111, 112]. | 61 |
| 4.3 | Comparison of energies, in a.u., of F^{6+} and F^{7+} states, based on the GTO basis set and the NIST data [73] and Refs [115, 127] | 79 |
| 4.4 | Comparison of energies, in a.u., of O^{5+} and O^{6+} states, based on the GTO basis set and the NIST data [73] and reference [136] | 89 |
| 5.1 | Coefficients and exponents used to represent the system $\text{C}^{4+} + e^-$ by the model potential eq. 5.2 | 98 |
| 5.2 | Comparison of energies, in a.u., of C^{3+} and C^{2+} , triplet and singlet, based on the GTO basis set and the NIST data | 99 |
| A.1 | The GTO coefficients used to describe the electronic states of H | 117 |
| A.2 | The GTO coefficients used to describe the electronic states of Li^+ and Li^{2+} | 118 |
| A.3 | The GTO coefficients used to describe the electronic states of He, He^+ , Li^+ , Li^{2+} , B^{3+} , B^{4+} and C^{4+} , C^{5+} | 119 |
| A.4 | The GTO coefficients used to describe the electronic states of C^{3+} and C^{4+} | 120 |
| A.5 | The GTO coefficients used to describe the electronic states of He and He^+ | 120 |
| A.6 | The GTO coefficients used to describe the electronic states of F^{6+} and F^{7+} | 121 |

| | | |
|------|--|-----|
| A.7 | The GTO coefficients used to describe the electronic states of He and He ⁺ | 121 |
| A.8 | The GTO coefficients used to describe the electronic states of O ⁵⁺ and O ⁶⁺ | 122 |
| A.9 | The GTO coefficients used to describe the electronic states of He and He ⁺ | 122 |
| A.10 | The GTO coefficients used to describe the electronic states of C ²⁺ and C ³⁺ | 123 |
| A.11 | The GTO coefficients used to describe the electronic states of He and He ⁺ | 123 |

Chapter 1

Introduction

Over the last century, physics and the way of our understanding of Nature have changed continuously through the development of quantum physics. Initially this took place mostly by investigating, theorising and experimenting atoms and molecules isolated or interacting with each other or with particles such as electrons or photons, at energies offered by the available technology, at a given period of the 20th century. A leading role of the development and interpretation of quantum physics was played by the field of atomic and molecular collisions and the study of the electronic processes during the scattering.

The electronic transitions induced by the collisions between atoms and molecules, neutral or ionised, are indeed of fundamental interest at atomic scale but also play important roles in the dynamics of many complex media, as for example cold and warm plasmas, e.g. for oxidation balance and magnetic thermonuclear fusion. Although these processes are now well understood and modelled when they involve a single active electron, this is not true for transitions involving several active electrons or where the static and dynamic electronic correlations play an important role. Before referring to some of these applications it is important to define the basic electronic processes occurring in collisions.

They can be categorised through the initial and final electronic states involved in the collision. Considering two partners of the collision, the target (T) and the projectile (P), let us first define the electronic processes which we consider in this thesis.

- elastic process: the initial and final electronic states of T and P are identical. In addition the incident projectile¹ is deflected at a certain angle, depending on the relative velocity of the two collisional partners,

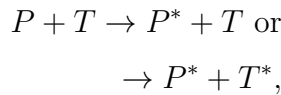
$$P + T \rightarrow P + T.$$

¹In the following, for simplicity, we shall describe a collision as a moving particle (the "projectile") and a particle at rest (the "target"). However the equations to solve and the results presented are derived in the centre of mass frame and are Galilean invariant.

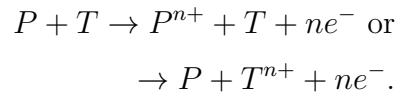
- electron capture²: During the collision, electrons are transferred between the collision partners, in ground or excited state. Defining n as the number of involved electrons, one can write the process



- excitation: One (or more) electrons of at least one of the two partners is promoted to a state of higher energy, e.g.

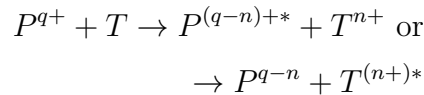


- ionisation: The scattering process induces the ejection of n electrons from one or both partners,

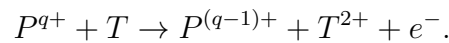


Furthermore, one can observe many combination of the aforementioned basic processes. For example we can refer to two multielectronic processes that are described in the frame of the present thesis,

- transfer-excitation,



- and transfer-ionisation,



Besides a fundamental point of view, these processes are important in a large number of domains. Indeed the collisions can be considered as a laboratory-on-earth to study a variety of quantum many-body systems [1, 2], as well as a range of macroscopic astrophysical objects, e.g. supernova remnants, solar wind interacting with interstellar media, chemical processes [3–6].

On the other hand, our domain enters in a number of applications in science and technology. As a first example, let us mention a medical application

² Alternatively, "electron transfer" or "charge exchange" can be found in literature.

that is hadron therapy, which consists in irradiating tumours with protons (proton therapy) or light nuclei (helium, carbon ions) and concerns the treatment of certain deeply localised cancerous tumours, allowing to precise targeting on the tumour while preserving the surrounding healthy tissues. Hadron therapy is relatively recent and is considered to become one of the major methods to be used to suppress certain tumours i.e. tumours in the brain and the eye. Traditionally, cancer is treated by methods like surgery, chemotherapy and radiation, X-ray therapy or the combination of them, when needed. As shown in Figure 1.1 conventional radiotherapy has the main drawback of interacting with healthy cells through the trajectory between the skin and the depth of the cancerous cells. By depositing a considerable amount of the dose on healthy tissue it may cause death of the healthy cells, leading to unpleasant and harmful results. On the contrary, irradiating cancer cells with protons (or C^{6+}) beams, the major deposition precisely targets the area to be treated by considerably limiting the possible damage of the healthy parts, up to an accuracy of μm . Hadrons can penetrate the tissue and interact mostly with the tissue at the preferable depth, where the Bragg peak is centred, directly depending on the energy of the injected beam.

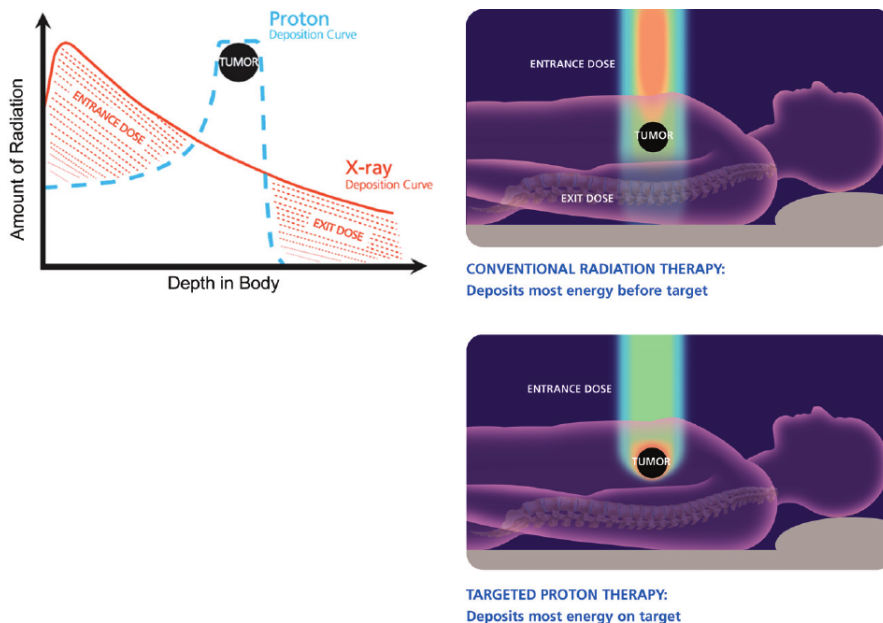


FIGURE 1.1: The Spread Out Bragg Peak (SOBP) is associated with a lower entrance dose and no exit dose when compared with conventional X-ray radiation. In the case of hadrons, the area where the dose is deposited is controlled and depended on the energy of the incoming beam (typically 100 MeV). Figure is from [7] and is courtesy of University of Florida Proton Therapy Institute

The physics underlying this medical application concerns mainly the inelastic collisions of nuclei with atoms and molecules present in the tissue. Indeed, during the penetration, the ions lose gradually their energy by ionising them, creating secondary electrons which also damage the tissue. When they slow down, at the Bragg peak, they deposit much efficiently their energy by ionisation and then electron transfer processes, in the limited zone of space where the tumour is located. [8]

Atomic collisions play also a leading role in plasma science and specifically in the research field of magnetic and inertial confinement fusion. One can come across atomic collisions in areas such as heating, confining and fueling plasma, keeping the gas stable, controlling its impurity at the plasma edge. In the frame of the magnetic fusion, in the hot plasma area where the fusion reactions occur, atomic processes such as ionisation, excitation, and electron capture contribute to the energy balance and fluid stability. Many tokamaks are heated by the injection of beams of high energy neutral atoms (20-40 keV). The presence of these neutral atoms can lead to an additional recombination mechanism through the reaction $H + A^{q+} \rightarrow H^+ + A^{(q-1)+}$ [9]. In the region where plasma interacts with the solid wall of the fusion chamber (Figure 1.2), the so called plasma edge, the energy and density decrease rapidly in the radial direction and plasma interacts with the walls releasing cold impurities which, through inelastic collisions with the plasma electrons and protons, cause a further decrease of plasma temperature. [10]

Concerning the physical properties of the plasma, the most direct application of atomic physics in fusion research is the area of diagnostics. The current range of diagnostic techniques requires knowledge of a broad spectrum of collisions involving electron and heavy particles, in neutral or ionic states. Spectroscopic techniques, based on bremsstrahlung or on spectral line intensity ratios, usually require knowledge not only of direct excitation processes, but also of all the rest of processes which lead to population of corresponding levels, as well as, knowledge on the ionisation charge state equilibrium for the radiating species [10].

Atomic physics is even more important in inertial confinement research [11]. It is crucial to access and extract information on the equations of state and opacities for the designing of the fusion target pellet as well as understanding their behaviour. In inertial fusion a frozen pellet-to be irradiated by laser/ion beams is considered to include the fuel of the energy production. The absorption of laser light and deceleration of energetic ions in the outer layers of the imploding pellet (Figure 1.3), the design and construction of high energy lasers and ion beams, as well as the spectroscopy and laser scattering for diagnosing

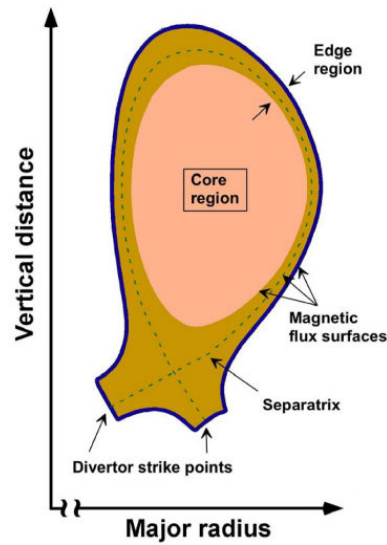


FIGURE 1.2: Plasma regions in a tokamak. The core region is where the plasma is fully confined. The separatrix, also last closed flux surface (LCFS), separates the confined plasma from the outer region. For tokamaks, the magnetic configuration shows a so called x-point, which is where the LCFS magnetic surface reconnects or closes on itself, which is used for a controlled energy deposition to the outside. The Figure is taken from [12]

pellet's implosion, depend on the aforementioned atomic collisions.

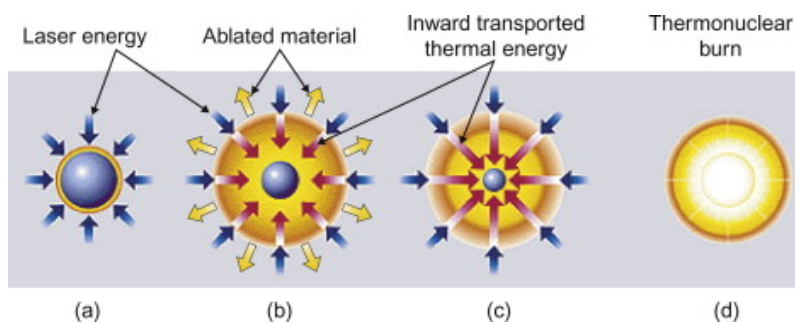


FIGURE 1.3: A frozen pellet is irradiated and thermalised relatively instantly by a number of laser beams. (a) Laser heating of the outer layer. (b) Due to the momentum conservation during the ablation of the outer layer a radial shock-wave compresses the capsule. (c) The core of the fuel reaches the required density and temperature for ignition. (d) The fuel burns under thermonuclear conditions and fusion reaction spreads rapidly through the compressed fuel. The Figure is taken by [13]

To interpret the outcomes of laboratory scattering experiments and to deliver atomic relevant data for the modelling and diagnostic of the complex media mentioned just above, it is important to develop methods and codes to compute cross sections for the electronic processes likely to occur in given conditions. These cross sections depend strongly on the impact relative velocity (energy) between the collision partners. It can be categorised in three "regions" according to the ratio between the velocity of the projectile v_P and the classical velocity v_e of the active electrons located on the target. Therefore, we can distinguish the three regions as low-, intermediate- and high-energy according to the ratios $v_P/v_e \ll 1$, $v_P/v_e \approx 1$ and $v_P/v_e \gg 1$, respectively. As it is schematically depicted in Figure 1.4 the three regimes and the theoretical approaches are distinguished as:

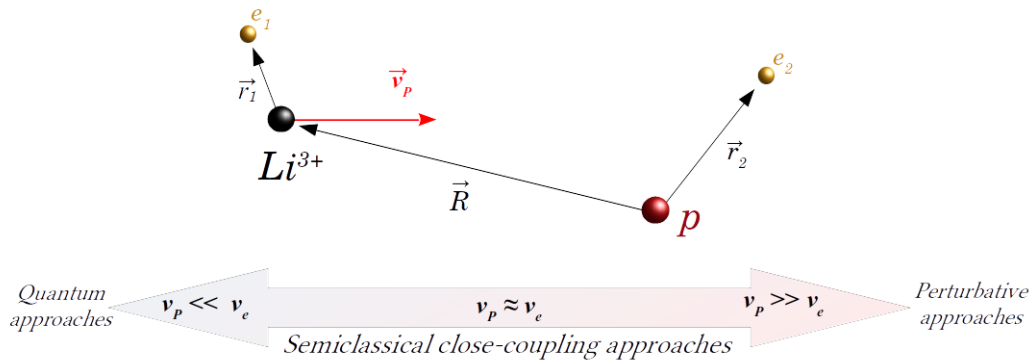


FIGURE 1.4: Geometrical scheme of an ion-atom collision, i.e. $\text{Li}^{2+} - \text{H}$, and the different approaches depending on the relative impact velocity. It is distinguished in three regions as low-, intermediate- and high-energy according to the ratios $v_P/v_e \ll 1$, $v_P/v_e \gg 1$ and $v_P/v_e \approx 1$, respectively.

- $v_P/v_e \ll 1$. At low velocities, the inelastic processes are rare and the dominant process is the electron capture. In this regime, the collision can be described by the electronic states of a transient quasi-molecule formed by the partners of the collision. Electronic transitions then occur mainly when there is degeneracy or quasi-degeneracy, at avoided crossings, between the molecular states that the system follows during the collision. In this region, non perturbative calculations within a limited number of molecular states are required, within fully quantum or semiclassical approaches [14–16], the latter involving a classical description of the relative motion between target and projectile.

- $v_P/v_e \approx 1$. This is the so-called intermediate energy regime. In this region all the inelastic processes such as charge exchange, excitation and ionisation can be of the same order of magnitude and likely i.e. characterised by large cross sections. This kind of collisions shall be treated non perturbatively, semiclassical or classically. The semiclassical approach is necessary in the intermediate domain but often difficult to implement especially when several electrons are active. It is presented in detail in the second chapter of the thesis. Classical Trajectory Monte Carlo (CTMC) methods, which describe the dynamics of all the particles by Newton equations of motion, was developed initially by R. Abrines and I. C. Percival [19] and have the advantage to be simply implemented but require further approximations for ion-atom collisions to deal with multi-electronic systems [20].
- $v_P/v_e \gg 1$. In high velocities the dominant processes are ionisation and excitation. The interaction time between the collision partners is short, of the order of several attoseconds, and the projectile can be considered a small perturbation on the target, so that perturbation theory becomes valid. As an example, a common perturbative approach is the first order Born approximation [17], while often, more elaborate, treatments follow the Continuum Distorted Wave approach [18].

Nowadays, the single active electron processes, such as single electron capture, excitation and ionisation, can be considered well understood and modelled for one and quasi-one electron systems (e.g. $H^+ - H(1s)$, $H^+ - Na(3s)$) while electron correlation is absent or plays a minor role. On the contrary, this is not true for transitions involving several active electrons. In such systems it is likely that i) a large number of channels are coupled and ii) the static and dynamic electronic correlations play an important role so that the use of independent electron approximation is excluded.

For physicists the understanding and modelling of multiple active electron collision systems is still challenging. In particular, in the intermediate impact energy region, where perturbative approaches cannot be used to describe the underlying physics due to the strong couplings between various open channels and electronic correlation effects. As a consequence, non perturbative multi-active electron semiclassical or quantum approaches are rare and still required.

In the frame of the present thesis, we apply a non perturbative semiclassical approach to describe multi-electronic processes occurring during non-relativistic

ion-atom collisions. The treatment is semiclassical in that the relative target-projectile motion is described by classical straight-line constant velocity trajectories. On the contrary the electronic dynamics is treated quantum mechanically, by solving non perturbatively the time-dependent Schrödinger equation (TDSE). In our team several codes [21–28] have been developed to solve the TDSE. Their use has been strongly focused on taking into account a very large number of channels as well as all couplings. These codes correspond to several thousand lines written in Fortran and are able to be applied for numerous collisions systems. They are also the only ones worldwide which can handle collision systems up to quasi-four-electrons.

During the present thesis work, we have studied several collision systems in regard of needs in plasma diagnostics (Li^{2+} - H) and also of very recent experimental investigations (C^{3+} , C^{4+} , O^{6+} , F^{7+} - He). In addition, we have developed a code to build the electronic states to be included in the collision code, since this prior stage is extremely important for describing as well as possible the systems considered but also to optimise the calculations which are extremely CPU and memory consuming.

In Chapter 2, the theoretical background of the semiclassical approach used in the present study is briefly presented. It is applied to TDSE, also called the eikonal equation in this content. Then follows the description of the semi-analytical method adopted to solve the TDSE which results in a set of coupled differential equations to be solved. We then describe the Gaussian type orbital (GTO) that we adopt to express the wavefunctions, as well as the algorithm used to optimise the basis sets.

In Chapter 3, electron capture and excitation in the context of $\text{Li}^{2+}(1s)$ - $\text{H}(1s)$ collisions is presented. We study total, shell and sub-shell cross sections, calculated in the energy domain 0.1 - 250 keV/u. Additionally, we discuss anisotropy spin effects encountered in electron transfer. A Oppenheimer-Brinkman-Kramers (OBK) approach is derived for the needs of understanding the effect at high energies ($\approx \text{MeV/u}$). We illustrate the interpretation with results obtained for four collision systems, He^+ , Li^{2+} , B^{4+} , C^{5+} - H.

In Chapter 4 we study the formation of doubly excited states occurring in MeV collisions between helium-like ions with He. In particular we focus on C^{4+} , O^{6+} , F^{7+} projectiles and the production of KLL states. The processes we mainly study in this chapter are single electron capture and transfer-excitation. These investigations have been performed for comparisons and interpretations of published experimental results but also in collaboration with experimentalists from University of Crete, University of Ioannina and NCSR "Demokritos" in

Athens, Greece [29].

Finally, in Chapter 5 our method is applied to examine the single electron capture and transfer-excitation processes in $C^{3+} - He(1s^2)$ collisions for low impact energies ranging from 0.5 to 400 keV/u. We focus on the production of $1s^22s^2\ ^1S$, $1s^22s2p\ ^1P$ and $1s^22p^2\ ^1D$ singlet and $1s^22s2p\ ^3P$, $1s^22p^2\ ^3P$ triplet states as well as on spin effects observed experimentally by collaborators in Institute of Modern Physics, Lanzhou, China [30] for the production of $1s^22s2p\ ^{1,3}P$ states.

Finally we end this manuscript by a summary of the presented results as well as several directions of developments and research for the future. These conclusions are followed by annexes presenting technical details concerning our calculations.

Chapter 2

The non perturbative semiclassical atomic orbital close-coupling approach

2.1 Introduction

In the field of atomic and molecular physics, during the 20th and 21st centuries there have been extensive theoretical studies on collisions. In parallel of the use of simple models to describe approximatively scattering events, quantum theory has been developed for potential scattering, by solving the time-independent Schrödinger equation, for example by the use of partial wave expansion approaches. At high energies for which partial wave expansions are not applicable, approximations are considered to introduce the dynamics over time. But even in this case, the simplest ion-atom collision system ($H^+ - H$) cannot be treated analytically exactly. Hence, the description of any electronic processes during any scattering event cannot be made without approximations [31].

The validity of any given approximation depends strongly on the relative velocity of the collision partners and on the charge of the projectile (in ion-atom collisions). In the frame of the present thesis, we study processes occurring during collisions, at impact energies ranging between 0.1 to 1.5 MeV/u. In this wide energy domain, we use a semiclassical approach so that the relative motion between projectile and target is described by classical trajectories and the dynamics of the electrons of the system is treated quantum mechanically. This approach is valid only by ensuring the fact that, the *de Broglie* wavelength associated with the relative motion between the target and the projectile is very small compared to the distance over which the interaction takes place during the collision. For example, the *de Broglie* wavelength for a proton of velocity

v_P with respect to the target at rest can be expressed in atomic units as

$$\lambda_d (a.u.) = \frac{2\pi}{1836 v_P}.$$

For an impact energy $E = 25$ keV/u, the impact velocity of the projectile is $v_P = 1$ a.u. so that the *de Broglie* wavelength is $\lambda_d = 3.4 \times 10^{-3}$ a.u. The interaction typically takes place when the target and the projectile are separated by less than a few atomic units of distance (say 10 a.u.) much larger than the *de Broglie* wavelength. In our studies we consider collision energies higher than the 100 eV/u, that is, $v_P > 0.05$ a.u., making the semiclassical approximation valid.

This Chapter describes the semiclassical non perturbative approach used in the study of the present collisions. The method has been well established in past works [32–34] and describes the inelastic processes in ion-atom/molecule collisions at intermediate energies by use of atomic orbital (AO) expansions of the total electronic wavefunction [35]. Since the interplays between many open channels are taken into account through a non perturbative treatment, our approach is also named semiclassical atomic orbital close-coupling (SCAOCC) method. The so called impact parameter approximation allows to transform the time-independent Schrödinger equation of the total system to the time-dependent Schrödinger equation (TDSE) of the electrons in the field of the moving nuclei. This equation is also called eikonal equation, by analogy with optics. First we present the outline of this development. Next, the method used to solve the eikonal equation non perturbatively is presented and illustrated in the case of two-active-electron systems. The last part of the chapter describes the Gaussian type orbital (GTO) expansion used to describe the atomic structure and the principle of the automatisation of optimisation of the GTO to evaluate the basis sets. Finally, we present briefly the computer implementation of the method, to finally evaluate the total cross sections.

2.2 Impact parameter method - The eikonal equation

In quantum mechanics the general treatment of a collision between ions, atoms or molecules concerns solving the time-independent Schrödinger equation,

$$\hat{H}^{tot} \Psi_{sys} = E^{tot} \Psi_{sys}, \quad (2.1)$$

where H^{tot} is the Hamiltonian operator and E^{tot} the corresponding energy of the complete system in the laboratory reference frame. For a system consisting of n_N nuclei n_e electrons, the Hamiltonian can be written as the summation of the kinetic and potential energies operators (in atomic units)

$$\hat{H}^{tot} = \hat{T} + \hat{V}, \quad (2.2)$$

with

$$\hat{T} = \sum_{I=1}^{n_N} -\frac{1}{2M_I} \nabla_{R_I}^2 + \sum_{i=1}^{n_e} -\frac{1}{2} \nabla_{r_i}^2 \quad (2.3)$$

$$\hat{V} = \sum_{I=1}^{n_N} \sum_{i=1}^{n_e} V_{Ii} + \sum_{I=1}^{n_N} \sum_{J=1}^{n_N} V_{IJ} + \sum_{i=1}^{n_e} \sum_{j=1}^{n_e} V_{ij} \quad (2.4)$$

where \vec{R}_I , M_I denote the positions and mass of the nuclei and \vec{r}_i the positions of the electrons of mass $m_e = 1$ a.u. The potential energy operators \hat{V}_{Ii} , \hat{V}_{IJ} and \hat{V}_{ij} correspond to the Coulomb potentials of the nucleus-electron, the internuclear and interelectronic interactions, respectively. It is convenient to write the Hamiltonian in the internal coordinate system. We restrict the treatment to two-electron systems, for collisions between ion and atoms or diatomic molecules. In addition, we make use of the approximation of the infinite nuclear mass, that is the mass of electrons is neglected with respect to the nuclei ones. Hence the total Hamiltonian \hat{H}^{tot} can be expressed as

$$\hat{H}^{tot} = -\frac{1}{2} \nabla_{r_1}^2 - \frac{1}{2} \nabla_{r_2}^2 - \frac{1}{2\mu_{TP}} \nabla_{R_{TP}}^2 - \frac{1}{2M_{tot}} \nabla_{R_G}^2 + \hat{V} \quad (2.5)$$

The R_{TP} is the internuclear distance of the collision partners, R_G is the position of the centre of mass for the total system in the reference system of the laboratory and the reduced masses are defined as

$$\mu_{TP} = \frac{M_T M_P}{M_T + M_P} \quad (2.6)$$

$$M_{tot} = M_T + M_P \quad (2.7)$$

The indices T and P correspond to the target and projectile, respectively.

It is useful to separate the Hamiltonian depending on the internal coordinates, so that the kinetic energy operator T^{tot} that depends on the internal coordinates of the collision system can be written as

$$\hat{T}^{tot} = \hat{T}^{int} - \frac{1}{2M_{tot}} \nabla_{R_G}^2 \quad (2.8)$$

and consequently, since the potential energy depends only on the relative coordinates between the particles, the Hamiltonian can be expressed as

$$\hat{H}^{tot} = \hat{H}^{int} - \frac{1}{2M_{tot}} \nabla_{R_G}^2 \quad (2.9)$$

Then one can simply separate the coordinates of centre mass from the relative ones between the particles so that

$$\Psi_{sys} = \Psi_{int} \Psi_G = \Psi_{int} e^{i\vec{k}_G \cdot \vec{R}_G}, \quad (2.10)$$

and

$$E^{sys} = E^{int} + E^G, \quad (2.11)$$

where $e^{i\vec{k}_G \cdot \vec{R}_G}$ describes the motion of a free particle in the laboratory frame and $E^G = \frac{k_G^2}{2M_{tot}}$ the corresponding (kinetic) energy. Then the Schrödinger equation can be separated and be written as

$$\hat{H}^{int} \Psi_{int} = E^{int} \Psi_{int}, \quad (2.12)$$

and

$$-\frac{1}{2M_{tot}} \nabla_{R_G}^2 \Psi_G = E^G \Psi_G. \quad (2.13)$$

After the internal and laboratory separation of variables we can express the Hamiltonian as

$$\hat{H}^{int} = -\frac{1}{2} \nabla_{r_1}^2 - \frac{1}{2} \nabla_{r_2}^2 - \frac{1}{2\mu_{TP}} \nabla_{R_{TP}}^2 + \hat{V} \quad (2.14)$$

for ion-atom collisions, which can be expressed in a general form as

$$\hat{H}^{int} = \hat{H}^{el} - \frac{1}{2\mu_{TP}} \nabla_{R_{TP}}^2, \quad (2.15)$$

with

$$\hat{H}^{el} = -\frac{1}{2} \nabla_{r_1}^2 - \frac{1}{2} \nabla_{r_2}^2 + \hat{V}. \quad (2.16)$$

Moreover, the nuclear masses are much larger than that of the electrons so that the kinetic energy term corresponding to the relative motion of the target and the projectile can be considered significantly larger than the electronic energy in the impact energy domain considered. Hence one can treat the relative motion of the nuclei independently of the electrons independent, so that the Ψ_{int} can be approximately written as a product of the electronic wavefunction

$\Psi(\vec{r}_1, \vec{r}_2, \vec{R})$ and the nuclei wavefunction $\Xi(\vec{R})$,

$$\Psi_{int} = \Xi(\vec{R})\Psi(\vec{r}_1, \vec{r}_2, \vec{R}) \quad (2.17)$$

In the frame of this approximation, the dependence on \vec{R} is mainly included in $\Xi(\vec{R})$ [33]. Furthermore, in the impact energy domain considered, the scattering is predominantly in the forward direction with respect to the initial direction of the projectile and the wavefunction $\Xi(\vec{R})$ can be expressed approximately as a plane wave [36],

$$\Xi(\vec{R}) = e^{i\vec{k}\cdot\vec{R}} \quad (2.18)$$

where \vec{k} is the wave vector, of magnitude

$$k = \sqrt{2\mu_{TP}E^{int}} \quad (2.19)$$

Using equations 2.15-2.19, the Schrödinger equation (2.12) becomes

$$\left[\hat{H}^{el} - \frac{i}{\mu_{TP}} \vec{k} \cdot \vec{\nabla}_R \right] \Psi = 0. \quad (2.20)$$

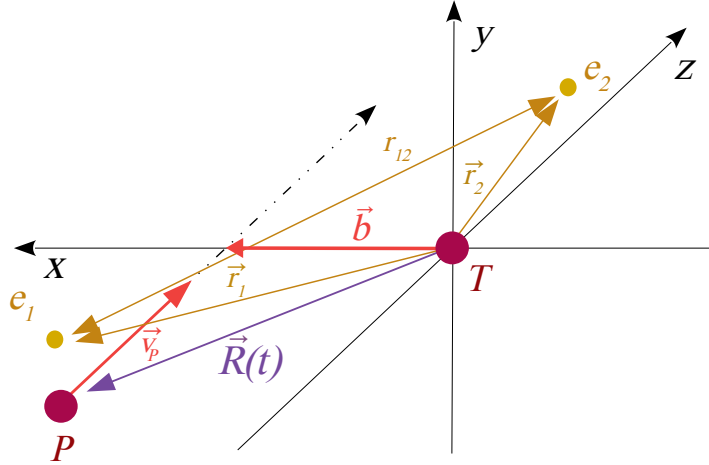


FIGURE 2.1: (a) The ion-atom collision geometry. The impact parameter \vec{b} and velocity \vec{v}_P define the xz plane, that is the collision plane, and $\vec{R}(t)$ symbolises the trajectory that the projectile follows with respect to the target. Vectors \vec{r}_1 , \vec{r}_2 and $\vec{r}_{12} = \vec{r}_2 - \vec{r}_1$ represent the positions of the two electrons, e_1 , e_2 with respect to the target and the relative vector between them, respectively.

As mentioned, the spread of the projectile is mainly forward, in a few degrees cone. Accordingly the relative heavy particle motion is approximated classically

as a straight line constant velocity trajectory (Figure 2.1) as

$$\vec{R}(t) = \vec{b} + \vec{v}_P t, \quad (2.21)$$

where \vec{b} is the impact parameter and \vec{v}_P the relative velocity between target and projectile,

$$\vec{v}_P = \frac{1}{\mu_{TP}} \vec{k}. \quad (2.22)$$

The impact parameter \vec{b} and velocity \vec{v}_P define the xz plane, that is the plane of the collision, and $\vec{R}(t)$ represents the trajectory that the projectile follows with respect to the target. It should be noted that, in Figure 2.1, the origin of the reference system is located for simplicity on the centre of mass of the target without losing the general validity of our approach, which is Galilean invariant. Combining equations 2.20 and 2.22, it results in the time-dependent Schrödinger equation (TDSE) of the electrons, which is finally written as,

$$i\hbar \frac{\partial}{\partial t} \Psi = \hat{H}^{el} \Psi, \quad (2.23)$$

the so-called eikonal equation. In the next sections, the method to solve the eikonal equation is presented, as well as the definition of the total and angular differential cross sections of the electronic processes occurring during atomic or molecular collisions.

2.3 Solution of the eikonal equation in Hilbert space

In general, the time-dependent Schrödinger equation cannot be solved in closed analytical form. To treat this, there have been developed a variety of theoretical and computational methods. At the beginning nuclear physicists [37–40], followed by atomic physicists [41, 42], provided a number of grid calculation methods based on the discretisation of time and space using the finite-difference method. These methods were not effectively used much because they require large computer resources for convergence, not available at that time. Although the recent computer science and technology provide higher performance, the grid methods are not efficient enough, since to describe ion-atom collisions requires the use of very large spatial grids and thus extremely long calculations. They are rare and generally used for systems limited to single active electron or/and to lower spatial dimensions, see for example [43–46]. As a result two-

or more-active-electron numerical grid calculations in full dimensions cannot be considered currently feasible. Thus in our team the TDSE has been treated by expanding the wave functions on a set of analytically defined functions in Hilbert's space.

This semi-analytical treatment has been already used extensively on one-active-electron systems [32, 33, 36] and two-active-electron collision systems [24–28, 47]. In the next sections this formalism is presented for the two-active-electron¹ systems, which has been used and implemented in the original computational codes developed by our team. In eikonal equation (eq. 2.23) the wave function is expanded on a basis of states obtained diagonalizing the Hamiltonian of the isolated collision partners and expressed in terms of analytical orbitals. The eikonal equation becomes equivalent to a set of coupled differential equations for time-dependent coefficients from which one can compute cross sections. In the following, we present an outline of the method.

2.3.1 The electronic wave function

The asymptotic states of the isolated collision partners (target and projectile) are described by linear combinations of Gaussian-type orbitals (GTO) and spin-adapted products of the same GTO set. In the spherical coordinates, the GTOs are defined as

$$G_{a,l,m}(\vec{r}) = Y_{l,m}(\theta, \phi) r^l e^{-ar^2} \quad (2.24)$$

with $Y_{l,m}$ the spherical harmonics and l , m the azimuthal and the magnetic quantum numbers. The one-electron states of the collision partners are therefore written as the weighted sum of the GTOs,

$$\phi(\vec{r}) = \sum_{i=1}^N c_i G_{a_i, l_i, m_i}(\vec{r}), \quad (2.25)$$

$$H^{el} = \sum_{i=1,2} \left[-\frac{1}{2} \nabla_i^2 + V_T(\vec{r}_i) + V_P(|\vec{r}_i - \vec{R}(t)|) \right] + \frac{1}{|\vec{r}_1 - \vec{r}_2|} \quad (2.26)$$

and the two-electron states are defined as,

$$\phi^\pm(\vec{r}_1, \vec{r}_2) = \sum_{i=1}^N \sum_{j=i}^N C_{ij} \left[G_{a_i, l_i, m_i}(\vec{r}_1) G_{a_j, l_j, m_j}(\vec{r}_2) \pm G_{a_i, l_i, m_i}(\vec{r}_2) G_{a_j, l_j, m_j}(\vec{r}_1) \right]. \quad (2.27)$$

¹We present the formalism for two-active-electron for simplicity and since it shows the main features of the method for multielectronic systems.

The symmetry \pm of the states depends on the spin state (singlet corresponding to + and triplet to -) of the collision system, under the Pauli principle. This spin symmetry, imposed by the initial conditions, is retained during the collision, since our model does not include spin-orbit couplings. The coefficients c_i and C_{ij} are obtained by diagonalisation on these sets of one- and two-electron functions, for the one- and two-electron Hamiltonians of the isolated partners.

The total electronic wave function $\Psi(\vec{r}_1, \vec{r}_2, \vec{R}(t))$ of the collision system consists of the sum of N_T , N_P one-electron states and N_{TT} N_{PP} two-electron states regarding the target or the projectile respectively,

$$\begin{aligned} \Psi(\vec{r}_1, \vec{r}_2, \vec{R}(t)) &= \sum_{i=1}^{N_{TT}} c_i^{TT}(t) \Phi_i^{TT}(\vec{r}_1, \vec{r}_2) e^{-iE_i^{TT}t} f^T(\vec{r}_1) f^T(\vec{r}_2) \\ &+ \sum_{k=1}^{N_T} \sum_{l=1}^{N_P} c_{kl}^{TP}(t) \left[\phi_k^T(\vec{r}_1) \phi_l^P(\vec{r}_2, \vec{R}(t)) f^T(\vec{r}_1) f^P(\vec{r}_2) \right. \\ &\pm \left. \phi_k^T(\vec{r}_2) \phi_l^P(\vec{r}_1, \vec{R}(t)) f^T(\vec{r}_2) f^P(\vec{r}_1) \right] e^{-i(\epsilon_k^T + \epsilon_l^P)t} \\ &+ \sum_{j=1}^{N_{PP}} c_j^{PP}(t) \Phi_j^{PP}(\vec{r}_1, \vec{r}_2, \vec{R}(t)) e^{-iE_j^{PP}t} f^P(\vec{r}_1) f^P(\vec{r}_2) \end{aligned} \quad (2.28)$$

with T, P, TT and PP standing to characterise the one-electron states and related energies (E) and two-electron states and related energies (ϵ) of the target and the projectile, respectively. At long enough distances, where the partners are isolated, we can categorise the following three asymptotic cases that satisfy the Schrödinger equations,

$$\hat{H}_{el}^{TT} \Phi_i^{TT}(\vec{r}_1 \vec{r}_2) = E_i^{TT} \Phi_i^{TT}(\vec{r}_1 \vec{r}_2) \quad (2.29)$$

$$\hat{h}_{el}^{T,P} \phi_{k,l}^{T,P}(\vec{r}_1 \vec{r}_2) = \epsilon_{k,l}^{T,P} \phi_{k,l}^{T,P}(\vec{r}_1 \vec{r}_2) \quad (2.30)$$

$$\hat{H}_{el}^{PP} \Phi_j^{PP}(\vec{r}_1 \vec{r}_2) = E_j^{PP} \Phi_j^{PP}(\vec{r}_1 \vec{r}_2) \quad (2.31)$$

corresponding to the state Φ_i^{TT} of two electrons attached to the target T, before the collision, the state $\phi_{k,l}^{T,P}$, where the two partners have one electron each, and Φ_j^{PP} of two electrons attached to the projectile P. The time evolution of the wave function is carried by the coefficients \mathbf{c}_f ($\equiv \mathbf{c}^{TT}$, \mathbf{c}^{PP} , \mathbf{c}^{TP}) which, in the limit $t \rightarrow \infty$, correspond to probability amplitudes. The $f^{T,P}(\vec{r}_i, i = 1, 2)$ are called "Electronic Translation Factors" (ETF) and guarantee the Galilean invariance regarding the relative motion of the partners and can cancel spurious dipolar

couplings [48]. These phase factors can be written as

$$\begin{aligned} f^T(\vec{r}_i, t) &= e^{-ip\vec{v}_P \cdot \vec{r}_i} e^{-i\frac{1}{2}p^2 v_P^2 t} \\ f^P(\vec{r}_i, t) &= e^{-i(1-p)\vec{v}_P \cdot \vec{r}_i} e^{-i\frac{1}{2}(1-p^2)v_P^2 t} \end{aligned} \quad (2.32)$$

where p any real number defined in $[0,1]$, depending on the chosen origin of the reference frame. Here it should be noted that the $f^{T,P}(\vec{r}_{1,2})$ action lies only on the relative velocity between projectile and target. Fixing the origin of the reference system on the target, we can re-express equations 2.27 and 2.31, without any loss of generality as

$$\begin{aligned} \Psi(\vec{r}_1, \vec{r}_2, t) &= \sum_{i=1}^{N_{TT}} c_i^{TT}(t) \Phi_i^{TT}(\vec{r}_1, \vec{r}_2) e^{-iE_i^{TT}t} \\ &+ \sum_{k=1}^{N_T} \sum_{l=1}^{N_P} c_{kl}^{TP}(t) \left[\phi_k^T(\vec{r}_1) \phi_l^P(\vec{r}_2) f^P(\vec{r}_2) \right. \\ &\quad \left. \pm \phi_k^T(\vec{r}_2) \phi_l^P(\vec{r}_1) f^P(\vec{r}_1) \right] e^{-i(\epsilon_k^T + \epsilon_l^P)t} \\ &+ \sum_{j=1}^{N_{PP}} c_j^{PP}(t) \Phi_j^{PP}(\vec{r}_1, \vec{r}_2) e^{-iE_j^{PP}t} f^P(\vec{r}_1) f^P(\vec{r}_2) \end{aligned} \quad (2.33)$$

where

$$f^P(\vec{r}_i) = e^{-i\frac{1}{2}v_P^2 t} e^{i\vec{v}_P \cdot \vec{r}_i} \quad (2.34)$$

2.3.2 The coupled differential equation system

Inserting equation 2.32 in the eikonal equation (eq. 2.23) we obtain a system of first-order coupled differential equations (CDE), which in matrix form can be written as

$$i \frac{d}{dt} \mathbf{c}(t) = \mathbf{S}^{-1}(\vec{b}, \vec{v}, t) \mathbf{M}(\vec{b}, \vec{v}, t) \mathbf{c}(t) \quad (2.35)$$

where \mathbf{c} is the column vector of the expansion coefficients and \mathbf{M} , \mathbf{S} the coupling and overlap matrices. The coupling matrix is given by

$$\mathbf{M} = \begin{pmatrix} M_{(TT)_1,(TT)_1} & M_{(TT)_1,(TT)_2} & \dots & M_{(TT)_1,(TP)_1} & \dots & M_{(TT)_1,(PP)_{N_P}} \\ M_{(TT)_2,(TT)_1} & M_{(TT)_2,(TT)_2} & \dots & M_{(TT)_2,(TP)_1} & \dots & M_{(TT)_2,(PP)_{N_P}} \\ M_{(TT)_3,(TT)_1} & M_{(TT)_3,(TT)_2} & \dots & M_{(TT)_3,(TP)_1} & \dots & M_{(TT)_3,(PP)_{N_P}} \\ \dots & \dots & \dots & \dots & \dots & \dots \\ M_{(TT)_{N_T},(TT)_1} & M_{(TT)_{N_T},(TT)_2} & \dots & M_{(TT)_{N_T},(TP)_1} & \dots & M_{(TT)_{N_T},(PP)_{N_P}} \\ M_{(TP)_1,(TT)_1} & M_{(TP)_1,(TT)_2} & \dots & M_{(TP)_1,(TP)_1} & \dots & M_{(TP)_1,(PP)_{N_P}} \\ M_{(TP)_2,(TT)_1} & M_{(TP)_2,(TT)_2} & \dots & M_{(TP)_2,(TP)_1} & \dots & M_{(TP)_2,(PP)_{N_P}} \\ M_{(TP)_3,(TT)_1} & M_{(TP)_3,(TT)_2} & \dots & M_{(TP)_3,(TP)_1} & \dots & M_{(TP)_3,(PP)_{N_P}} \\ \dots & \dots & \dots & \dots & \dots & \dots \\ M_{(PP)_1,(TT)_1} & M_{(PP)_1,(TT)_2} & \dots & M_{(PP)_1,(TP)_1} & \dots & M_{(PP)_1,(PP)_{N_P}} \\ \dots & \dots & \dots & \dots & \dots & \dots \\ M_{(PP)_{N_P},(TT)_1} & M_{(PP)_{N_P},(TT)_2} & \dots & M_{(PP)_{N_P},(TP)_1} & \dots & M_{(PP)_{N_P},(PP)_{N_P}} \end{pmatrix}. \quad (2.36)$$

Expressing for simplicity any of TT-, TP- and PP-type asymptotic cases as A and B during the interaction, the elements of the coupling matrix \mathbf{M} can be defined as

$$M_{A_i,B_j} = \langle \Phi_i^A(\vec{r}_1, \vec{r}_2) F_i^A(\vec{r}_1, \vec{r}_2) | H_{el} | \Phi_i^B(\vec{r}_1, \vec{r}_2) F_i^B(\vec{r}_1, \vec{r}_2) \rangle \quad (2.37)$$

where the energy phases are included in the Φ functions and the F phases represent the product of the relevant ETF. Applying the eq. 2.16, one gets

$$\begin{aligned} M_{A_i,B_j} &= \langle \Phi_i^A(\vec{r}_1, \vec{r}_2) F_i^A(\vec{r}_1, \vec{r}_2) | T_1 + T_2 | \Phi_i^B(\vec{r}_1, \vec{r}_2) F_i^B(\vec{r}_1, \vec{r}_2) \rangle \\ &+ \langle \Phi_i^A(\vec{r}_1, \vec{r}_2) F_i^A(\vec{r}_1, \vec{r}_2) | V_{T_1} + V_{T_2} | \Phi_i^B(\vec{r}_1, \vec{r}_2) F_i^B(\vec{r}_1, \vec{r}_2) \rangle \\ &+ \langle \Phi_i^A(\vec{r}_1, \vec{r}_2) F_i^A(\vec{r}_1, \vec{r}_2) | V_{P_1} + V_{P_2} | \Phi_i^B(\vec{r}_1, \vec{r}_2) F_i^B(\vec{r}_1, \vec{r}_2) \rangle \\ &+ \langle \Phi_i^A(\vec{r}_1, \vec{r}_2) F_i^A(\vec{r}_1, \vec{r}_2) | \frac{1}{r_{12}} | \Phi_i^B(\vec{r}_1, \vec{r}_2) F_i^B(\vec{r}_1, \vec{r}_2) \rangle \end{aligned} \quad (2.38)$$

where T_i is the kinetic energy of the electron i , V_{T_i} (V_{P_i}) is the interaction potential between electron i and target (projectile) nucleus (and inner electrons if the frozen core approximation is used).

Equivalently, the overlap matrix \mathbf{S} can be expressed as

$$\mathbf{S} = \begin{pmatrix} S_{(TT)_1,(TT)_1} & S_{(TT)_1,(TT)_2} & \cdots & S_{(TT)_1,(TP)_1} & \cdots & S_{(TT)_1,(PP)_{N_P}} \\ S_{(TT)_2,(TT)_1} & S_{(TT)_2,(TT)_2} & \cdots & S_{(TT)_2,(TP)_1} & \cdots & S_{(TT)_2,(PP)_{N_P}} \\ S_{(TT)_3,(TT)_1} & S_{(TT)_3,(TT)_2} & \cdots & S_{(TT)_3,(TP)_1} & \cdots & S_{(TT)_3,(PP)_{N_P}} \\ \cdots & \cdots & \cdots & \cdots & \cdots & \cdots \\ S_{(TT)_{N_T},(TT)_1} & S_{(TT)_{N_T},(TT)_2} & \cdots & S_{(TT)_{N_T},(TP)_1} & \cdots & S_{(TT)_{N_T},(PP)_{N_P}} \\ S_{(TP)_1,(TT)_1} & S_{(TP)_1,(TT)_2} & \cdots & S_{(TP)_1,(TP)_1} & \cdots & S_{(TP)_1,(PP)_{N_P}} \\ S_{(TP)_2,(TT)_1} & S_{(TP)_2,(TT)_2} & \cdots & S_{(TP)_2,(TP)_1} & \cdots & S_{(TP)_2,(PP)_{N_P}} \\ S_{(TP)_3,(TT)_1} & S_{(TP)_3,(TT)_2} & \cdots & S_{(TP)_3,(TP)_1} & \cdots & S_{(TP)_3,(PP)_{N_P}} \\ \cdots & \cdots & \cdots & \cdots & \cdots & \cdots \\ S_{(PP)_1,(TT)_1} & S_{(PP)_1,(TT)_2} & \cdots & S_{(PP)_1,(TP)_1} & \cdots & S_{(PP)_1,(PP)_{N_P}} \\ \cdots & \cdots & \cdots & \cdots & \cdots & \cdots \\ S_{(PP)_{N_P},(TT)_1} & S_{(PP)_{N_P},(TT)_2} & \cdots & S_{(PP)_{N_P},(TP)_1} & \cdots & S_{(PP)_{N_P},(PP)_{N_P}} \end{pmatrix} \quad (2.39)$$

with the elements of the overlap matrix \mathbf{S} defined as

$$\mathbf{S}_{A_i,B_j} = \langle \Phi_i^A(\vec{r}_1, \vec{r}_2) F_i^A(\vec{r}_1, \vec{r}_2) | \Phi_i^B(\vec{r}_1, \vec{r}_2) F_i^B(\vec{r}_1, \vec{r}_2) \rangle. \quad (2.40)$$

Finally, the column vectors of the expansion coefficients are

$$\mathbf{c}(t) = \begin{pmatrix} c_{(TT)_1}(t) \\ c_{(TT)_2}(t) \\ c_{(TT)_3}(t) \\ \cdots \\ c_{(TT)_{N_T}}(t) \\ c_{(TP)_1}(t) \\ c_{(TP)_2}(t) \\ \cdots \\ c_{(PP)_1}(t) \\ c_{(PP)_2}(t) \\ c_{(PP)_3}(t) \\ \cdots \\ c_{(PP)_{N_P}}(t) \end{pmatrix} \quad (2.41)$$

These CDE of eq. 2.34 are solved for given initial conditions, i.e. an initial electronic state i , impact parameter b and impact velocity v_P by using a powerful predictor-corrector time-step method developed by Shampine and Gordon [49]. The probability of a transition $i \rightarrow f$ is given by the coefficients \mathbf{c}_f ($\equiv \mathbf{c}^{TT}$, \mathbf{c}^{PP} , \mathbf{c}^{TP}) when the two partners are far apart after the collision

$$P_{fi}(b, v_P) = \lim_{t \rightarrow \infty} |c_f(t)|^2. \quad (2.42)$$

Finally, as we will see extensively in the following chapters, the evaluation of the total cross sections for the considered transition is given by

$$\sigma_{fi}(v_P) = 2\pi \int_0^{+\infty} b P_f(b, v_P) db. \quad (2.43)$$

2.4 Implementation

For the evaluation of the probabilities and the cross sections characterising the electronic processes presented in the current thesis, we used computer programs, developed by the team during decades and are still under development. Initially, the programs were developed for one-active-electron ion-atom and ion-molecule collisions [50, 54], then for two-active-electrons [55, 56], and recently were generalised up to four-active-electron collisions [57]. The code to solve the coupled differential equations (eq. 2.34) to obtain the probability amplitudes, requires input parameters to define the Coulomb (or model potentials) carried by each of the collision partners, the impact velocity v_P , the impact parameter b , some accuracy parameters and the exponents and the angular momenta of the Gaussian type orbitals (GTOs) for the creation of the states by diagonalisation of the atomic Hamiltonians. The structure of the computer program follows the next five main stages:

- Initialisation where the GTO exponents are selected and optimised to describe the one- and multi-electron states for each of the isolated collision partners. They are used as input along with the information about the potentials of the target and projectile, the projectile velocity, the impact parameter values and the definition of the collision zone in which the eq. 2.34 is solved.
- Diagonalisation to obtain the states of the one- and two-electron Hamiltonians for the two isolated partners, using the set of GTOs input in the first stage. Then the set of states included to solve the ordinary differential equation (ODE) (eq. 2.34) is defined.
- Matrices evaluation: the evaluation of the overlap and coupling matrix elements along the projectile trajectory for a large number of grid points in the collision zone.²

²We use this strategy to avoid extremely long CPU time. The matrix elements are interpolated between these points required by the solver of the ODEs

- Dynamics stage during which, the system of first-order coupled differential equations is integrated over time, for the initial conditions on the fixed grid along the collision.
- Evaluation of the cross sections, total or angular differential.

To build the state basis set on which the wave function (eq. 2.32) is developed, is an indispensable step in the preparation of the computations. Indeed the memory (RAM) occupation and the CPU time increase considerably with the number of states and angular momenta included in the basis. It is therefore important to define an adequate and parsimonious basis set that includes a maximum of states, but keeping the computation time reasonable with the computer resources available. The basis set should include the states under consideration (the more likely populated and also the ones of interest i.e. for comparison with experiment) and, hopefully, all important states which couple to these former, to reach convergence. The convergence of the results presented in the following has been verified, using different bases to test this convergence but also with respect to the numerics and the quality of the modelling of the states. The latter point is performed by the optimisation of GTO. This stage is presented in the following section.

2.4.1 Gaussian Type Orbitals (GTO)

The first treatments in quantum chemistry used the so-called Slater-type orbitals (STOs) since these functions related to the hydrogenic ones, showing the correct asymptotic behaviour. They have the advantage that they have direct physical interpretation and thus are naturally good basis for our study. On the other hand they suffer by the drawback that they don't allow compact analytical form for the two-centre and two-electron integrals, so that they require very important CPU time for the evaluation of these latter. To avoid this drawback, Boys [58] proposed the use of Gaussian-type orbitals (GTOs) to extend the STO as linear combinations. This greatly simplifies therefore the evaluation of the integrals and speeds up the computations. They have been widely applied in quantum chemistry and in our domain. Integrals necessary for the calculations of the coupling matrix elements, are analytically evaluated, allowing thus, *ab initio* approaches.

To best describe the states of systems we have to optimise the GTO used in the calculations: one can play with the number of the functions eqs. 2.26 and 2.27 and on their exponents. The exponents of the latter are optimised to

obtain a good description of the important eigenstates in the collision using the minimum of basis functions. The choice of the set of GTOs is crucial for the dynamic part of the calculations and is based on three criteria:

- Firstly, the states and their energies to be included in the dynamics should be correctly described.
- Secondly, it is very important to consider the consumption of the computational resources and time. For a given precision to obtain the important states, the number of GTOs must be kept reasonably low to minimize computation times and the size of memory required.
- Thirdly, we shall deal with well tempered GTO set to avoid numerical problems and divergences.
- Ultimate convergence of the cross sections should be checked, that is their values should be independent of the choice of the GTO sets.

These factors are strongly linked to the collision system studied and may also depend on the collision impact velocity and on the electronic processes considered. For example, a base optimised for cross sections at intermediate energies may be insufficient for low energies, because of the different couplings and mechanisms in action in this section. However we tried to construct GTO sets to be satisfactory in a wide range of impact velocities in such way that a unique set of GTOs (and states) is considered in the calculations. The exponents of GTOs are optimised in order to keep a good description of the important states, trying to keep always minimum the size of the GTO sets.

In the present implementation, a linear combination of Gaussian-type orbitals (GTOs) centred on target and projectile is used, which are expressed in Cartesian coordinates (compared to eq. 2.24) for convenience

$$\chi_k = N_k x^{u_k} x^{v_k} x^{w_k} e^{-\alpha_k r^2}, \quad k = 1, 2, \dots, N, \quad (2.44)$$

where N_k is a normalisation parameter, u_k , v_k , w_k are non-negative integers (with $u_k + v_k + w_k = l$) describing any spherical harmonics for given l . For the description of the electronic states we try to keep even-tempered GTOs, optimising the exponents α_k in geometric progressions

$$\alpha_k = \alpha_1 \epsilon^{k-1}, \quad k = 2, \dots, N. \quad (2.45)$$

The procedure of optimisation in which all the exponents of GTOs are independently optimised is time consuming since requiring many diagonalisations

of the Hamiltonians. Reeves and Harrison [59] proposed even-tempered GTOs based on intuitive reasoning, while later Raffenetti [60] proposed it again depending on the empirical observation that when full optimisation is performed the optimised exponents obtained follow an almost straight line on the logarithmic scale. Defining the lowest and the highest exponents as α_{min} and α_{max} respectively, the algorithm, diagonalises the Hamiltonians and checks whether the atomic states are of lower energy. The optimisation of the exponents begins by scanning a series of α_{min} and α_{max} , (i.e. α_1, ϵ, N) on a S dimension space in a range defined manually by the user. Then a loop takes place to give a little “tilt” on the α exponents for which the optimal states have been obtained. As far as the multi-electron states are concerned, the algorithm minimises the difference between the energy obtained by diagonalisation on the GTO basis and the values found in the literature or the NIST database. In order to describe ionisation, pseudostates of positive energy (so called probability absorbers) are included in our bases too. It is therefore also important to minimise their energies. Indeed when these pseudostates possess very large energy (≥ 10 a.u.), they may cause numerical instabilities related to the energy factor $e^{-i\epsilon t}$ which oscillates very quickly even though they may be weakly populated during the collision. The algorithm is designed to optimise simultaneously up to two states of the same angular momentum, i.e., $1s$ and $2s$, for four different angular momenta, up to $l = 3$, i.e., s, p, d, f. It can be schematically outlined as

```

do tilt array
  do  $\alpha_{min}$  array
    do  $\alpha_{max}$  array
      GTO calculation by
      do  $j = 1, \#$  of  $\alpha$ 
         $newbasis(j) = \alpha_{min}exp^{j-1}, \quad exp = e^{\ln(\frac{\alpha_{max}/\alpha_{min}}{\# \text{ of } \alpha}-1)}$ 
      end do
      Hamiltonian diagonalisation
      keep minimum
    end  $\alpha_{max}$  array
    keep minimum
  end  $\alpha_{min}$  array
  keep minimum
end tilt array

```

The code provides the ability to investigate a range of α_{min} and α_{max} and have an overall mapping on where the eigenvalues of any state of interest get their minimal value. Hence, as depicted in Figure 2.2, we may create maps to investigate the behaviour of energy states depending the atom (or ion) studied. Thus, one can explore a wide range of α exponents, focusing in the optimum α values to succeed optimal energies for the states of interest.

Figure 2.2 shows an example of the results of this optimisation for six different states of atomic hydrogen. Each picture maps the energies obtained by diagonalisation for the lowest and largest exponents. The colour corresponds to the energy succeeded for each $(\alpha_{min}, \alpha_{max})$ combination. It can be observed that each atomic state may be optimised by different GTO exponent, therefore a simultaneous state optimisation is not an obvious task. However in hydrogen example we may observe a shift of the a_{max} to lower values for increasing excitation, that is the largest exponents may contribute more in the ground and/or the first excited state, while higher excited states are affected mainly by lower ones.

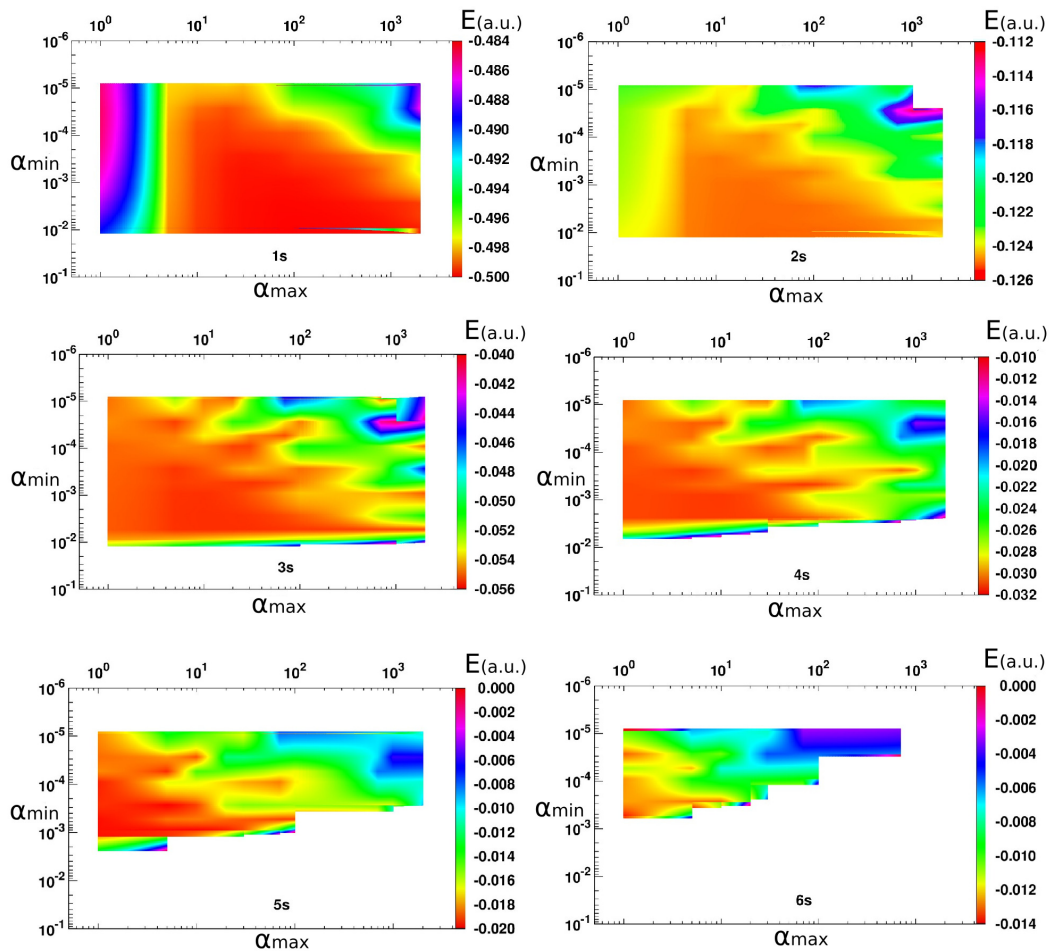


FIGURE 2.2: Example of the optimisation of the α exponents of the GTO for optimisation of the atomic states. The investigation as a function of α_{\min} and α_{\max} depicts the values of the exponents that can optimise the ground state and the first five excited states of hydrogen. Colour bar corresponds to the energy of the atomic state in a.u.

2.4.2 The evaluation of one- and two-electron integrals

The solution of the first-order coupled differential equations (eq. 2.34) is the heaviest and most demanding part of our computations, in terms of memory and CPU time. Several strategies have been developed by our team [25, 61] to compute the coupling M and overlap S matrix elements (equations 2.36, 2.39) considering the evaluation of the one- and two-electron multi-centre integrals. Recently a new strategy based on evaluating the integrals using recursive relationships (which reduces the memory requirement significantly) has also been developed in our group and implemented [26]. Since we were not involved in the development and optimisation of these methods, details on them will not

be included here but can be found in [56, 57]. We must also mention here that the evaluation of the matrix elements is done for a given number of mesh points on a grid spanning the collision zone in which the coupled differential equations (eq. 2.34) are solved in a second step. This grid shall be dense enough to ensure the quality of the interpolation and the convergence of the predictor-corrector strategy. In most of the systems studied in the present thesis, the coupling and overlap matrix elements are evaluated on a set of grid of 100 points ranging from -100 a.u. to +100 a.u. for all range of impact velocities considered in our investigations.

2.4.3 The solution of the ODEs

The numerical resolution of the time-dependent Schrödinger equation requires the use of propagation methods. They correspond to the propagation of an initial function for a sufficiently long time, ensuring convergence of the solutions step by step, and thus ensuring the physical meaning of the results. This propagation is performed by evaluating numerically the system of coupled differential equations (eq. 2.34), by a predictor-corrector algorithm. The basic idea of such algorithms consists of two steps, the prediction and the corrector steps:

- The first, prediction, step evaluates through the ODE, the functions and their first derivative for a given time step.
- The second, correction, step refines the initial evaluation by using a smaller time step and also extrapolation. Then these two series of values are tested for convergence to evaluate an optimised time step for further propagation.

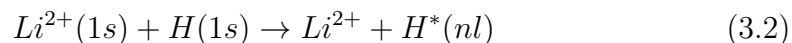
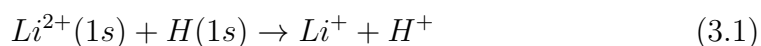
In the current implementation, the robust predictor-corrector time-step variable method developed by Shampine and Gordon [49] is used. The method adapts the time step automatically according to the evolution of the expansion coefficients during the integration procedure, to guarantee a given accuracy. The predictor-corrector algorithm requires therefore the evaluation of the M and S matrices at any times, not defined in our fixed time grid. Hence this evaluation is performed by Lagrange interpolation using the pre-computed values at mesh point.

Chapter 3

Li²⁺ - H collisions: State selective cross sections and spin effects

3.1 Introduction

Over the last few decades, electronic processes in collisions between lithium and hydrogen have attracted appreciable interest in thermonuclear fusion research and technology. Hydrogen and its isotopes, deuterium and tritium, have been considered as the prevailing fuel for energy production in the frame of the magnetic and inertial thermonuclear fusion [64, 65]. Moreover hydrogen and deuterium as well as lithium and lithium-like ion beam spectroscopies, are important tools to provide information on the ionisation balance in the plasma and impurity ion transport [66–68]. Lithium has also been proposed as a low atomic number plasma-facing material in tokamak reactors while new technologies are steadily developed, i.e. the capillary-pore system [69–71]. Such systems target to treat problems such as mechanical instabilities of liquid lithium films, thermal emission and accumulation of lithium in plasma columns [69, 72]. The lithium ions transit and thus the thermal emission is highly determined by their interaction with the hydrogen gas. The study of electronic processes induced in the course of the collisions of hydrogen and lithium, in any ionic state, is therefore important. Here, we study the processes of electron capture and excitation for lithium dication projectile



for impact energies ranging from 0.1 to 250 keV/u.

3.2 Calculation details

For this collision system, we have created and optimised several GTO sets for the hydrogen and lithium (Li^{2+} and Li^+) centres. Most of the cross sections used in this chapter have been obtained with B_1^H and B_1^{Li} sets (given in Appendix A) on H and Li centres: they are both composed by 56 GTOs (12 for $l = 0$, 8×3 for $l = 1$ and 4×5 for $l = 2$). After diagonalisation and the use of an energy cut-off¹ of ≈ 1 a.u., this set allows to include 2074 states describing elastic and excitation (Li^{2+}, H), capture (Li^+) and ionisation channels through the 542 positive pseudostates of energy above the ionisation threshold. In table 3.1, most of the important states of the Li^+ ion produced by electron capture are presented, alongside the energies of the corresponding values provided by the NIST database [73]. Our calculated eigenvalues are in a very good agreement (with differences smaller than 1%) with the NIST ones, except for the D states, which is expected since we use very few orbitals.

TABLE 3.1: Comparison of energies, in a.u., of the Li^+ ion, singlet (left) and triplet (right) states, calculated based on the GTO basis set and the NIST data using $B_1^{H,Li}$.

| State | E_{GTO} | E_{NIST} | $\Delta(\%)*$ | State | E_{GTO} | E_{NIST} | $\Delta(\%)*$ |
|--------------|-----------|------------|---------------|--------------|-----------|------------|---------------|
| $1s^2 \ ^1S$ | -7.2771 | -7.2798 | 0.038 | | | | |
| $1s2s \ ^1S$ | -5.0403 | -5.0410 | 0.013 | $1s2s \ ^3S$ | -5.1104 | -5.1109 | 0.009 |
| $1s2p \ ^1P$ | -4.9923 | -4.9934 | 0.022 | $1s2p \ ^3P$ | -5.0271 | -5.0278 | 0.014 |
| $1s3s \ ^1S$ | -4.7334 | -4.7339 | 0.010 | $1s3s \ ^3S$ | -4.7518 | -4.7522 | 0.009 |
| $1s3p \ ^1P$ | -4.7192 | -4.7203 | 0.024 | $1s3p \ ^3P$ | -4.7294 | -4.7306 | 0.024 |
| $1s3d \ ^1D$ | -4.6862 | -4.7225 | 0.768 | $1s3d \ ^3D$ | -4.6865 | -4.7226 | 0.764 |
| $1s4s \ ^1S$ | -4.6285 | -4.6299 | 0.029 | $1s4s \ ^3S$ | -4.6358 | -4.6372 | 0.031 |
| $1s4p \ ^1P$ | -4.6226 | -4.6243 | 0.037 | $1s4p \ ^3P$ | -4.6263 | -4.6286 | 0.049 |
| $1s4d \ ^1D$ | -4.1103 | -4.6252 | 11.13 | $1s4d \ ^3D$ | -4.1134 | -4.6253 | 11.07 |
| $1s5s \ ^1S$ | -4.5627 | -4.5825 | 0.433 | $1s5s \ ^3S$ | -4.5738 | -4.5862 | 0.271 |

* $\Delta = |(E_{GTO} - E_{NIST})/E_{NIST}| \times 100$

In addition, some convergence tests were performed with a few different basis sets, $B_2^{H,Li}$ of 45 GTOs (11 for $l = 0$, 8×3 for $l = 1$ and 2×5 for $l = 2$), $B_3^{H,Li}$ of 36 GTOs (12 for $l = 0$, 8×3 for $l = 1$), $B_4^{H,Li}$ of 62 GTOs (14 for $l = 0$, 6×3 for $l = 1$ and 6×5 for $l = 2$), $B_5^{H,Li}$, of 28 GTOs -10 for $l = 0$, 8×3 for $l = 1$, including 674, 784, 2206 and 560 energy states, respectively. Details of the GTO sets are given in Appendix A. Figure 3.1 shows the convergence of the different basis sets regarding the total electron capture cross sections. We

¹The cut-off value corresponds to the largest value of the total electronic energy of the states (here for (Li^{2+}, H) and Li^+) included in the scattering calculations.

can observe a good agreement for the results coming from these different sets. Accordingly the results, presented in the following, were obtained with the basis set $B_1^{H,Li}$ since it is large enough to describe the important channels with high accuracy, consuming reasonable computational resources.

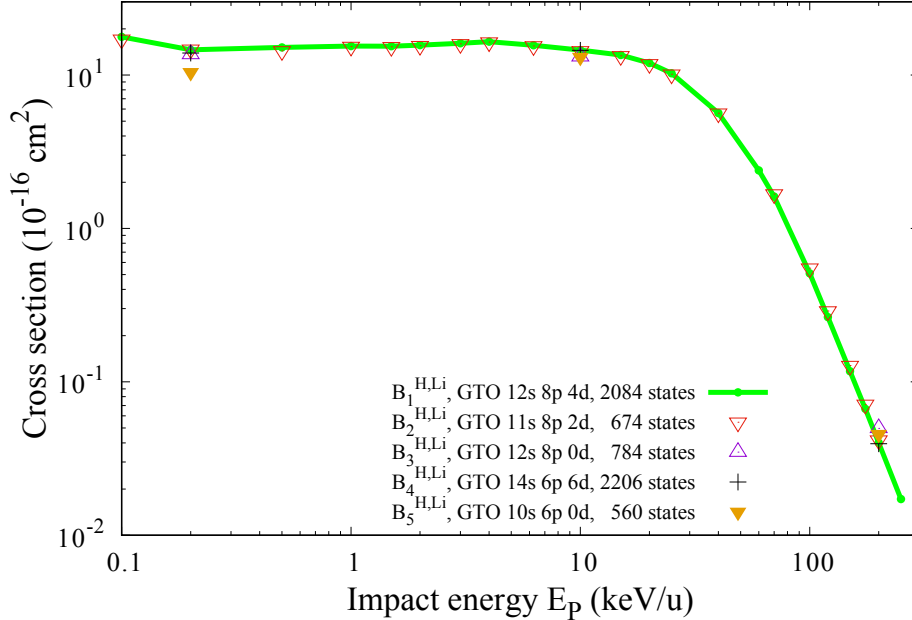
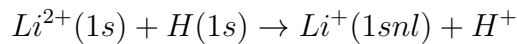
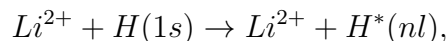


FIGURE 3.1: Convergence test for the five different basis sets given in Appendix A: total electron capture cross sections as function of impact energy of the Li^+ ion for $Li^{2+} - H$.

For this two-electron collision system the calculations are two-folded since, on one hand, the initial states for Li^{2+} and H are unique, i.e. their respective ground state, while, on the other hand, the initial total spin state may be undefined, except in polarised beam experiments, very rare and certainly not existing for $Li^{2+} - H$ collisions. We therefore performed calculations for singlet and triplet cross sections, averaging over spin statistic weight the respective spin states, i.e. for channel χ , as total capture



or for any specific excitation



the averaged cross sections is

$$\sigma(\chi) = \frac{\sigma_{\chi}^S + 3\sigma_{\chi}^T}{4}$$

where σ_{χ}^S and σ_{χ}^T are the cross sections for the channel χ calculated for initial singlet and triplet total spin states, respectively.

3.3 Results and discussion

3.3.1 Electron capture

We present in Figure 3.2 the spin-averaged cross sections of total capture as a function of the impact energy. Our results were obtained with the $B_1^{H,Li}$ basis set, over a wide energy range, from 0.1 to 300 keV/u. They are shown in thick green line together with eight series of theoretical data [76–82] and two of experimental results [74,75]. Note the lack of experimental data for this system, especially at low energies, below 2 keV/u, and also in the range 4 – 25 keV/u, limiting the comparisons to theoretical results in these domains.

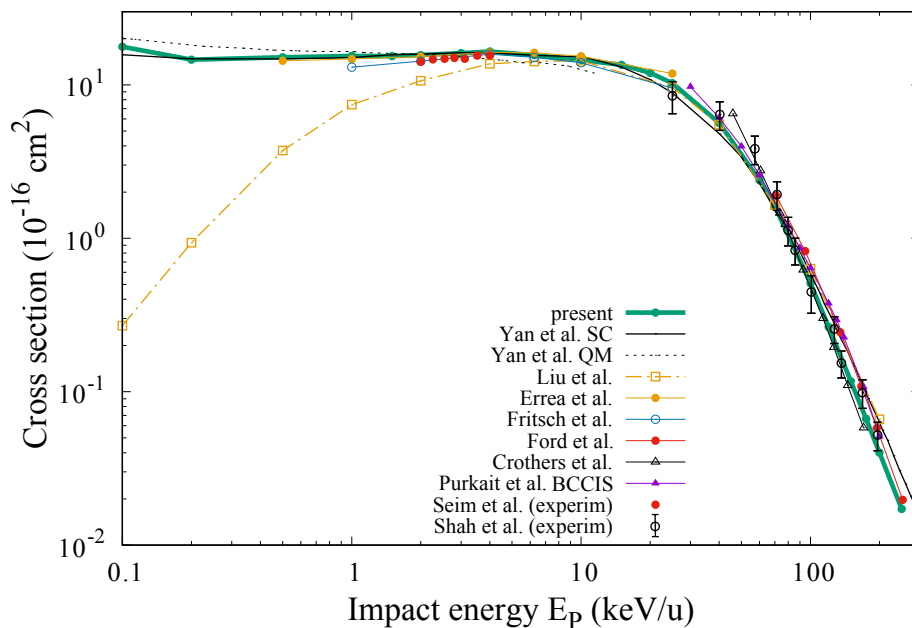


FIGURE 3.2: Total electron capture in Li^{2+} - $H(1s)$ collision as a function of the impact energy. The present results are shown as thick green solid line, with the full circles showing the different energies where the cross sections were evaluated. The experimental data are from Seim et al. [74] (solid red dot) and Shah et al. [75] (open black dot). Theoretical results are also shown: Yan et al. [78] (black solid line), Liu et al. [79] (yellow square dash-dot line), Errea et al. [77] (yellow full circle line), Fritsch et al. [76] (blue open solid circle line), Ford et al. [80] (red full circle line), Crothers and Todd [81] (black triangle line) and Purkait et al. [82] (purple open triangle line).

For energies ranging from 0.1 to 10 keV/u the cross sections show a plateau behaviour, typical for a (quasi-)resonant collision system. Capture is therefore favoured, with cross sections larger than 10^{15} cm². In this range our data are converged within 4% (and better) and agree very well with the recent semiclassical (AOCC) treatment reported in Yan et al [78] as well as with the MOCC results of Errea et al [77]. However the full quantum (QMOCC) cross sections reported also in [78] are larger up to 1 keV/u and show a slight decrease with increasing energy. It is difficult to conclude on the best series of data since, on one hand, the semiclassical approach, in [78] and present, may reach its limit of validity for the lowest velocity while, on the other hand, the convergence of QMOCC requires high partial waves for increasing energies. These problems have been discussed in [78] and the present results tend to validate their AOCC results. Note that Liu et al [79], as will be discussed in the following, reported lower cross sections in this energy range since they consider close-coupling only with singlet states.

At larger energies, the present results are about 10% larger than the experimental data reported in [74] and the AOCC results of Fritsch and Lin [76] but in nearly perfect agreement with [78]. Above 10 keV/u the cross sections start to decrease significantly and reach a v^{-7} regime beyond 100 keV/u, following the trend given by the Bohr-Lindhard model in [83]. Our agreement with AOCC of Yan et al [78] continues up to 60 keV/u, beyond which this latter calculations tend to predict somewhat larger cross sections, also seen in the distorted waves results of Purkait et al [82]. However our results agree quite well with the experimental results reported in [75], as well as the modified CDW theoretical results from Crothers and Todd [81], and the perturbative version of the one-and-a-half-centred expansion (POHCE) of Ford et al. [80]. Compared with previous results obtained in their respective validity ranges, one can conclude that our two-electron approach predicts reliable cross sections for the entire energy domain under consideration.

Figure 3.3 presents cross sections² for the most dominant capture channels $Li^{2+}(1s) + H(1s) \rightarrow Li^+(1snl \ ^1,^3L) + H^+$ for $n = 2$ and $n = 3$. Our results are shown with thick green lines together with the only available 3L theoretical results available, that is AOCC of Yan et al [78] as well as the TC-AOCC of Liu et al. [79] and the POHCE results of Ford et al. [80] only for 1L .

The results presented in this figure show clearly that the production of $Li^+(1sn = 2)$ by single electron capture dominates $Li^+(1sn = 3)$ production by

²The cross sections for capture to singlet and triplet states are not spin averaged and are obtained by pure singlet and triplet calculations, respectively.

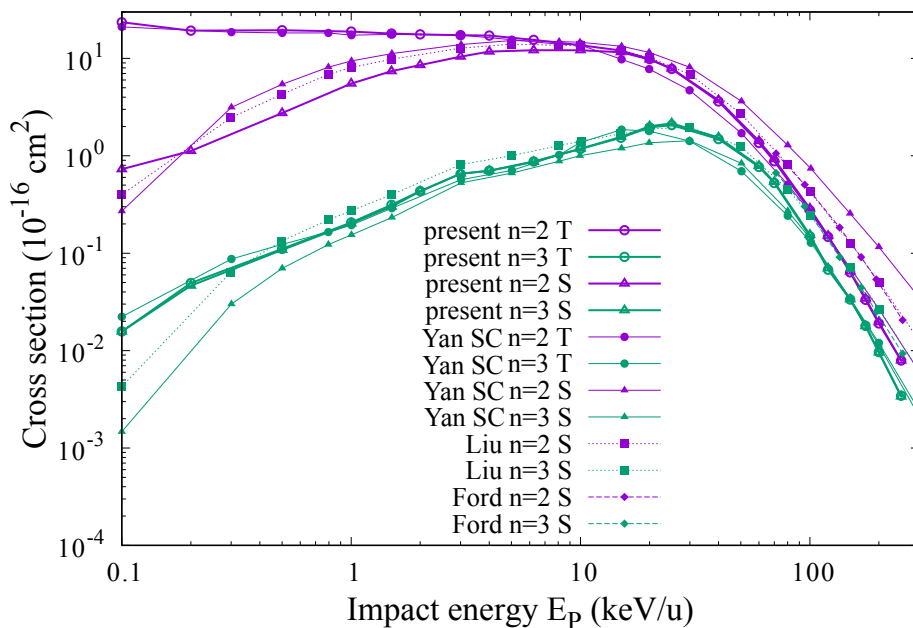


FIGURE 3.3: Cross sections of capture to the n -shell as a function of the impact energy. Our results are shown in thick lines, purple for $n = 2$ and green for $n = 3$, with open circles (triangles) for triplet (singlet). For comparison, three series of theoretical results are also shown in thin lines and same colour convention: Yan et al. [78] with full circles (triangles) for triplet (singlet), Liu et al. [79] and Ford et al. [80] for which only singlet states are shown, with full squares and diamond, respectively.

orders of magnitude at low energies, with difference decreasing for increasing energies. The total capture process, shown in Figure 3.2, is therefore mainly dominated by the transfer of the electron to the $n = 2$ shell. Concerning the spin state, the two channels present different behaviours: for capture to $n = 2$ the triplet cross sections are larger than the singlet ones by more than one order of magnitude at low energies with their difference decreasing for increasing energies. However, singlet and triplet cross sections show very similar values in the entire energy range considered. These results will be commented in section 3.2.2.

Figure 3.3 shows also three series of theoretical results for comparison. We note that they stem from one-electron calculations using model potentials to describe the interaction between the active electron and $Li^{2+}(1s)$ core. Moreover, in Liu et al. [79] and Ford et al. [80], only singlet calculations were performed, while singlet and triplet results were reported in Yan et al. [78], using two different model potentials to describe $Li^+(1s nl \ ^1L)$ and $Li^+(1s nl \ ^3L)$ ions. As a general comment, these results compare qualitatively well with our results, in their energy dependence. In more detail, the results reported in [78] compare

very well with ours for transfer to $n = 2$, in the triplet case, up to 10 keV/u, beyond which they are lower before to converge again after 100 keV/u. For transfer to $n = 2$ singlet the situation is somewhat different since the results in [78] are always larger than ours. Note that the results in [79] lay in between these two series of data. Since in [78] and [79], the authors use the same one-electron semiclassical atomic orbital close-coupling methods, with the same model potential to describe the singlet states of Li^+ , one may infer that the differences between these results are related to the different size of the basis sets used in the two calculations, showing therefore a convergence issue. This may also explain partly the fact that the cross sections for transfer to $n = 2$ singlet reported in [78] are significantly larger than all other calculations for energies above 20 keV/u. Finally, concerning the low energy region and as mentioned previously, the cross sections for triplet are larger than the ones for singlet: this explains the much lower values of cross sections for total capture reported in [79] since only singlet configurations were taken into account in this investigation. For the electron transfer to the $n = 3$ shell, one can see also a reasonable agreement in shape of the cross sections as function of impact energy, but significant quantitative differences, especially for the lowest energies considered. The quantitative disagreements between our results and the other theoretical data are certainly related to the fact that our calculations involve the two electrons, taking into account the interelectronic repulsion exactly, within the large basis sets used. This allows us also to take into account the differences between the Li^+ states, in singlet and triplet symmetries in a much elaborated way than the use of model potentials in one-electron approach. We shall comment the effects of the spin symmetries on the cross sections in the next subsection. However the validation of our results (or those reported in the three other investigations) should require further experimental investigations.

To go further in the analysis of our results we present in Figure 3.4 the sub-shell selective cross sections for electron capture. For low energies, the cross sections for both transfer to $2s$ and $2p$ in triplet symmetry are orders of magnitude larger than their singlet counterparts, the production of $\text{Li}^+(1s2s\ ^3S)$ dominating totally the capture process. More precisely, as far as the most dominant state $1s2s$ is concerned, Figure 3.4(a) shows that the cross section of $1s2s\ ^3S$ is larger than the $1s2s\ ^1S$ by a factor of even larger than 10^3 . Also, regarding the second most dominant state $1s2p$, Figure 3.4(b) shows that $1s2p\ ^3P$ exceeds the $1s2p\ ^1P$ by a factor of almost 10.

This behaviour can be simply explained since in this range, the process is dominated by molecular mechanisms, especially by interactions occurring in the

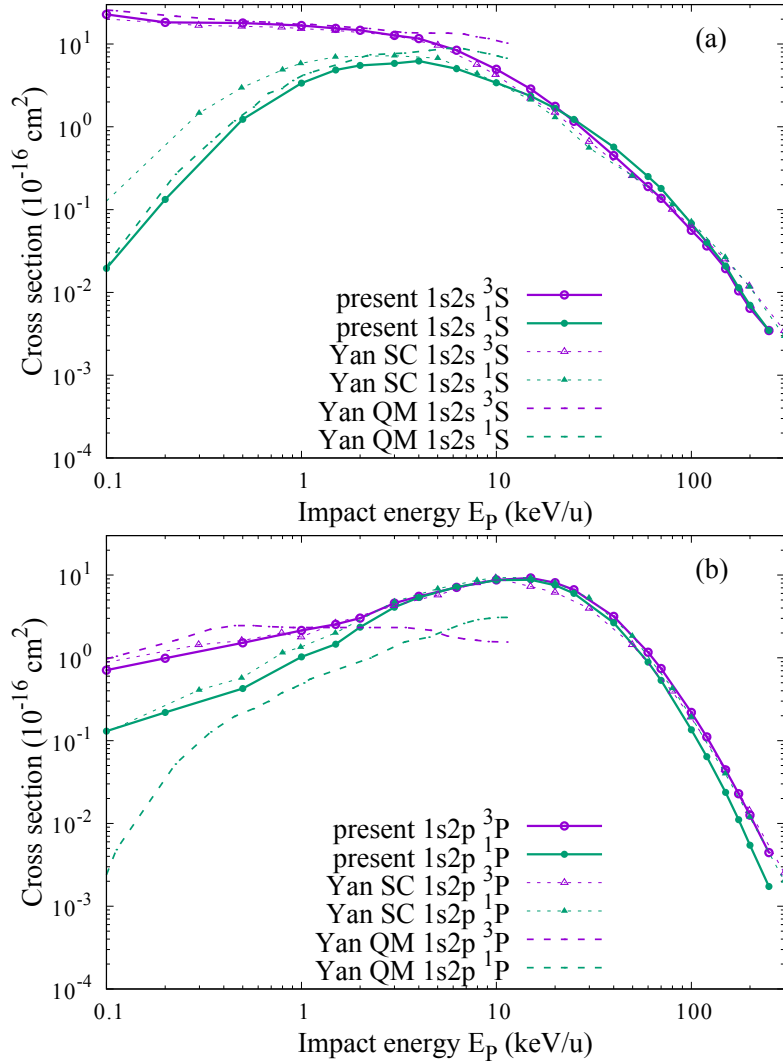


FIGURE 3.4: Sub-shell selective cross sections for electron capture to $1sn = 2$, (a) $l = 0$ and (b) $l = 1$. Present results are shown in thick line, purple for capture to triplet and green to singlet, with open (filled) circles for triplet (singlet). Keeping the same color convention, Yan et al. [78] SC is in open (solid) triangles for triplet (singlet) and their QM in only dashed lines.

vicinity of avoided crossings. When analysing the molecular curves of the triplet and singlet manifolds of Figure 3.5 (Figure 1 in [78]), important differences can be seen.

In Figure 3.5, one can see first that the molecular curves correlated asymptotically to the atomic $Li^+(1s3l)$ states have much larger energies than the ones corresponding to $Li^+(1s2l)$ and do not cross the curves correlated to the initial channel ($Li^{2+}(1s) - H(1s)$), except at very low internuclear distances R . Second, for these higher molecular curves, the triplet and singlet cases do not show significant differences. This explains the low and quite similar values of

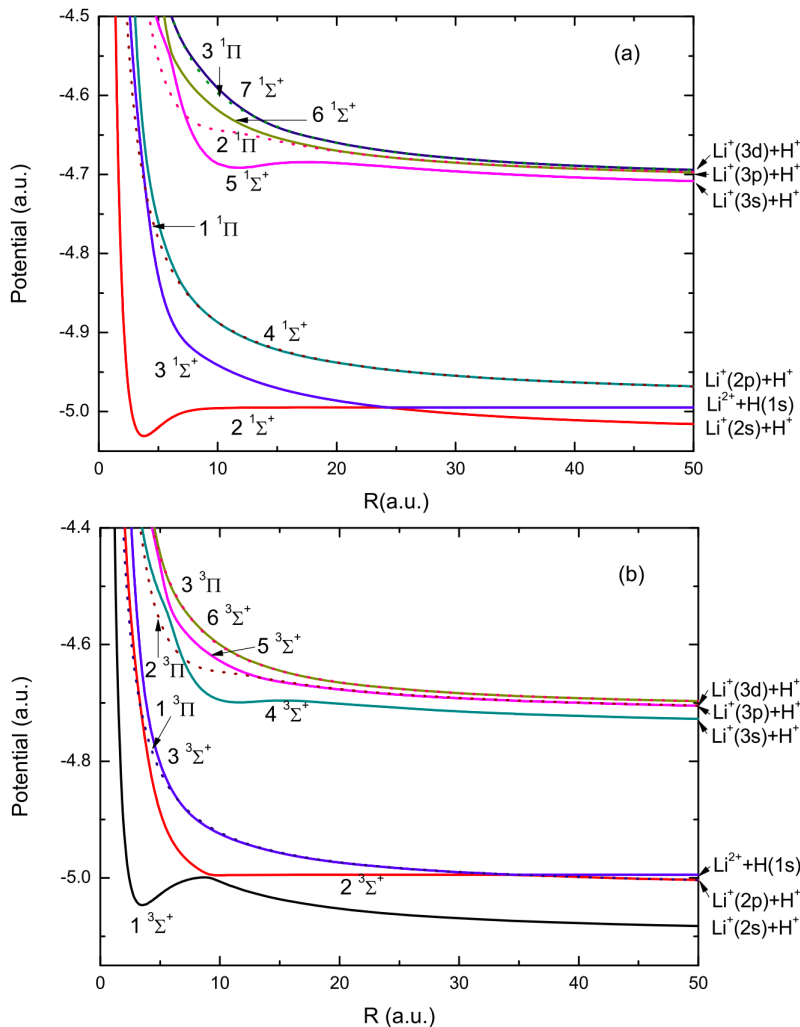


FIGURE 3.5: Adiabatic potential curves of LiH^{2+} for (a) singlet states and (b) triplet states. Solid lines denote the Σ^+ states; dotted lines the Π states. Figure taken by Yan et al. [78]

the cross sections for the production of $\text{Li}^+(1s3l)$ in singlet and triplet symmetries. This is clearly not the case for those of $\text{Li}^+(1s2l)$: Figures 3.5 (a) and (b) are quite different in [78]: the $2^1\Sigma^+$ curve (correlated to $\text{Li}^+(1s2s\ ^1S)$) presents a crossing with $3^1\Sigma^+$ (correlated to the initial channel in the singlet case) at large internuclear distance ($R \approx 24$ a.u.), though behaving adiabatically, and therefore not inducing a transition between the two curves. However, for the triplet symmetry, the $1^3\Sigma^+$ and $2^3\Sigma^+$ curves present a clear avoided crossing at $R \approx 9$ a.u. inducing a hop between them driven by a strong radial coupling (see Figure 2 in [78]). On the other hand, this behaviour does not exist for the curves correlated to $\text{Li}^+(1s2p\ ^{1,3}P)$. These two latter facts explain the dominance of the transfer to $2s$ for the triplet symmetry compared to both the singlet symmetry and the transfer to $2p$ (in both symmetries).

In our treatment we do not use the molecular representation of the collision system and therefore the coupling matrix, eq. 2.35 in Chapter 2, does not include explicitly radial and rotational couplings. However, since we present very converged results, our atomic basis representation gives a near exact picture of the mechanisms in action during the scattering, equivalent to their molecular counterparts. This can be seen in the Figure 3.6 where we show the reduced probabilities $bP(b)$ for the production of (a) $Li^+(1s2s\ ^3S)$ and (b) $Li^+(1s2p\ ^3P)$ at a typical, low, impact energy (0.2 keV/u): the probability for $Li^+(1s2s\ ^3S)$ shows a first and large peak at $b \approx 7$ a.u., i.e. for projectile trajectories which can pass the crossing, followed at decreasing impact parameters by the typical oscillations for this kind of mechanism. The probabilities for the other 3 channels are more than one order of magnitude smaller than the ones for transfer to $2p$ developing, as expected, only at small b ($b < 4$ a.u.). Our results for $1s2s$ production at these low impact parameter are also corroborated by the excellent agreement observed in Figure 3.4 between our results and Yan et al. [78] results stemming from the fully quantum treatments.

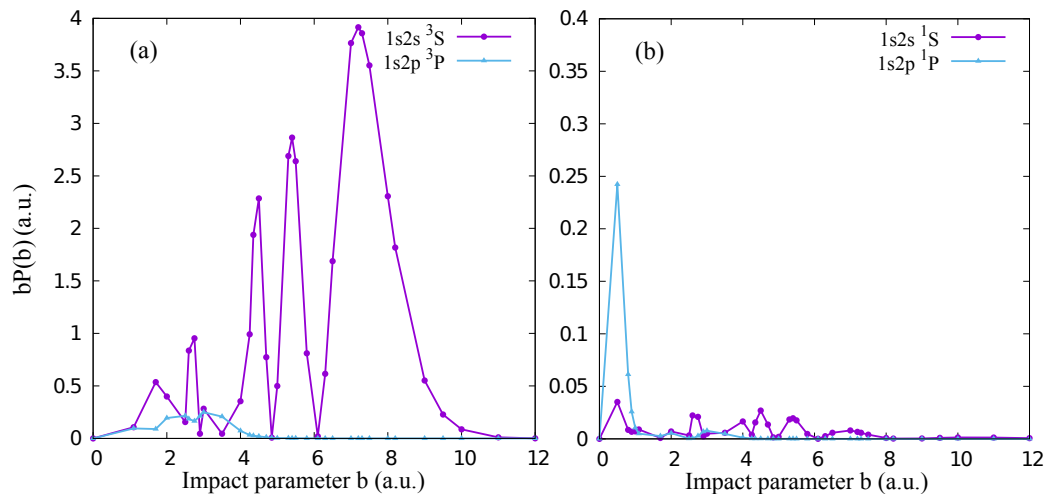


FIGURE 3.6: The reduced probabilities $bP(b)$ for the production of (a) $Li^+(1s2l\ ^3L)$ and (b) $Li^+(1s2l\ ^1L)$ at a typical, low, impact energy, 0.2 keV/u.

Finally the detailed analysis of the cross sections in Figure 3.4 for impact energies above 25 keV/u shows another, very particular, difference between electron transfer to $2s$ and $2p$: for $2s$, the singlet and triplet cross sections seem to tend to very close values, while the ones for $2p$ have clear distinct values. This feature will be discussed in detail in the next section, 3.3.2.

The cross sections for production of $\text{Li}^+(1s3l\ ^{1,3}L)$ by single electron capture is shown in Figure 3.7. At low energies, say below 1 keV/u, there are significant differences between our results and those of Yan et al. [78], the quantum and semiclassical data from this latter investigation showing also serious disagreement. It is then quite difficult to have a clear conclusion on the more exact results in this range, where the cross sections are quite low. Beyond 1 keV/u, the quantum calculations are clearly not converged and the comparison between the two semiclassical results show reasonable agreement, especially for the dominant capture process, producing $1s3s\ ^{1,3}S$. We note however that the cross sections for $1s3d$ production reported in [78] are clearly lower than ours: one may speculate that a problem of convergence in one or both series of results. From our side, as mentioned in the introduction of this chapter, the GTO set used in our calculations possess only few $l = 2$ orbitals, producing, after diagonalisation, D levels of less quality than the S and P levels, as can be seen in their energies listed in table 3.1. Independent calculations or experimental studies are required to validate some of these data. Finally, for these weaker channels, the cross sections for singlet and triplet electronic configurations get to close values at high energy, except for the 1P and 3P , as seen for $1s2p$. This spin asymmetry is the subject of the following subsection.

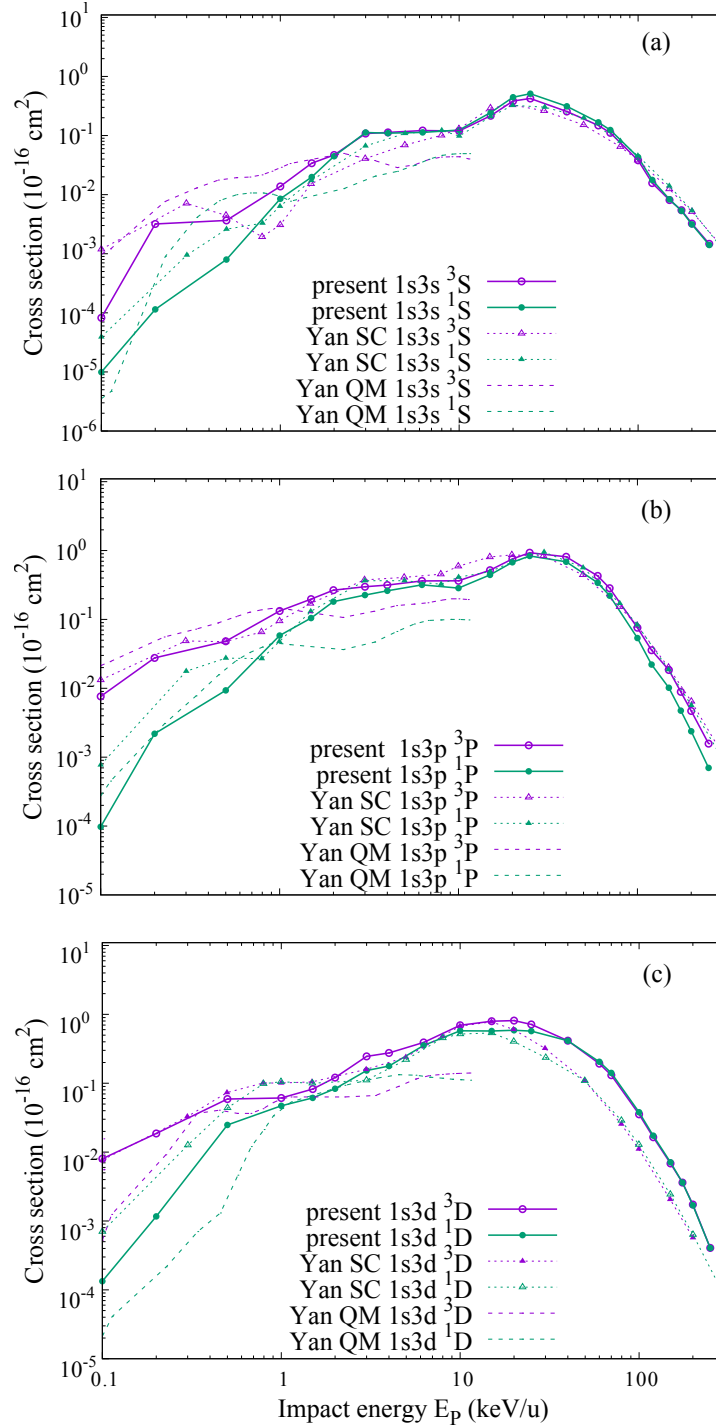


FIGURE 3.7: Sub-shell selective cross sections for electron capture to $1sn = 3$, (a) $l = 0$ (b) $l = 1$ and (c) $l = 2$. Present results are shown in thick line, purple for capture to triplet and green to singlet, with open (filled) circles for triplet (singlet). Keeping the same color convention, Yan et al. [78] SC is in open (solid) triangles for triplet (singlet) and their QM in only dashed lines.

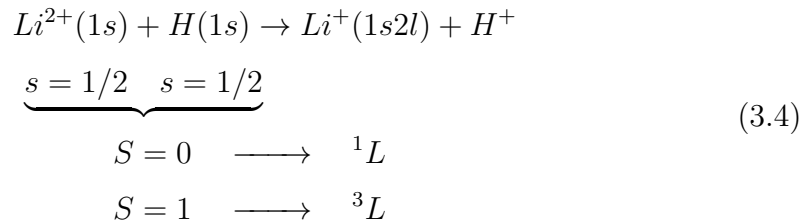
3.3.2 Spin anisotropy effect

As mentioned previously, Figures 3.4 and 3.7 show a significant difference between the triplet and singlet cross sections for P levels (for $1s2p$ and $1s3p$ configurations) at high collision energies but not for S and D ones. This difference seems counter-intuitive since one may expect that at high velocities, the cross sections should be very close in this high energy regime,

$$\lim_{v \rightarrow \infty} \sigma(^1L) \approx \lim_{v \rightarrow \infty} \sigma(^3L) \quad (3.3)$$

since the energies of the singlet and triplet states are close, i.e. $\sim 1\%$ for $1s2l$ and even lower for $1s3l$.

As mentioned at the beginning of this chapter, in Li^{2+} - H two-electron collision system, the initial state can be of singlet or triplet total spin symmetry, since our approach uses a Hamiltonian operator containing only Coulomb potential and no relativistic corrections, as spin-orbit, which may couple the spin symmetries, total spin is conserved during the collision and our calculations consist of two series of independent calculations with $S = 0$ and $S = 1$: a singlet or triplet $2e$ state:



For the two symmetries, the initial states, have, of course, the same energy and the two levels, corresponding to the same electronic configuration $1snl$ created after transfer, correspond to different but close values of energy. From simple first-order perturbative approach for one-electron systems, this energy argument³ may suggest similar cross sections for the two systems. It is what is seen for the production of all configurations considered, except for the P states. However the "convergence" of the singlet and triplet cross sections is shown for all states in the one-electron calculations reported in [78]. This effect, never reported in the literature to our knowledge, is therefore due to many-electron features, of special importance for P states.

³This argument does not take into account special feature of two-electron system, as two distinct wavefunctions for the singlet and triplet states due to antisymmetrisation, and more specifically Fermi hole effect (see eq.3.5) in the triplet case.

In the following paragraphs, we are going to develop a model to explain this feature which will be supported by further calculations for other two-electron collision systems. For the production of $1snl$ by single capture let us express the initial Ψ_i and final Ψ_f in a simple orbital representation as follows,

$$\begin{aligned}\Psi_i^\pm(\vec{r}_1, \vec{r}_2) &= \frac{1}{\sqrt{2}}(1s^P(1)1s^T(2) \pm 1s^T(1)1s^P(2)) \\ \Psi_f^\pm(\vec{r}_1, \vec{r}_2) &= \frac{1}{\sqrt{2}}(1s^P(1)2l^P(2) \pm 2l^P(1)1s^P(2)),\end{aligned}\quad (3.5)$$

where \pm stands for the singlet (+) and triplet (-) spin states, $1s^P$ and $2l^P$ represent orbitals on the projectile and therefore include ETF factors of eq. 2.33. The energy of Ψ_i and Ψ_f will be written, respectively, as $\epsilon_{1s^P} + \epsilon_{1s^T}$ and $E_{1s2l^P}^\pm$ in the following.

Considering a simplified version of the first-Born approximation referred as the Oppenheimer, Brinkman and Kramers (OBK) approximation [84], the process time dependent probability amplitude is expressed in the prior form as

$$C_{fi}^{OBK}(b, t \rightarrow \infty) = -i \int_{-\infty}^{\infty} dt' \langle \Psi_f^\pm | W | \Psi_i^\pm \rangle e^{-i(\epsilon_{1s^P} + \epsilon_{1s^T} - E_{1s2l^P}^\pm - \frac{1}{2}v^2)t'} \quad (3.6)$$

where W is the potential

$$W = -\frac{Z^P}{r_i} + \frac{1}{r_{ij}} \quad (3.7)$$

with the electrons i and j centred on the target and the projectile, respectively.

Since the energy of $Li^+(1s2l)$ in singlet $E_{1s2l^P}^+$ and triplet $E_{1s2l^P}^-$ are very close, the magnitude of the probability amplitude in eq. 3.5 is related mainly to the matrix element which can be expressed by

$$M_{fi}^\pm = \frac{1}{2} \langle 1s^P(1)2l^P(2) \pm 2l^P(1)1s^P(2) | W | 1s^P(1)1s^T(2) \pm 1s^T(1)1s^P(2) \rangle. \quad (3.8)$$

This coupling matrix element can be split into the four terms

$$\begin{aligned}M_{fi}^\pm &= \frac{1}{2} [\underbrace{\langle 1s^P(1)2l^P(2) | W | 1s^P(1)1s^T(2) \rangle}_{\textcircled{1}} \pm \underbrace{\langle 1s^P(1)2l^P(2) | W | 1s^T(1)1s^P(2) \rangle}_{\textcircled{2}}] \\ &\quad \pm [\underbrace{\langle 2l^P(1)1s^P(2) | W | 1s^P(1)1s^T(2) \rangle}_{\textcircled{3}} + \underbrace{\langle 2l^P(1)1s^P(2) | W | 1s^T(1)1s^P(2) \rangle}_{\textcircled{4}}]\end{aligned}\quad (3.9)$$

$$\begin{aligned}
& \textcircled{1} \rightarrow \langle 1s^P(1)2l^P(2) | -\frac{Z^P}{r_2} + \frac{1}{r_{21}} | 1s^P(1)1s^T(2) \rangle = \\
& \langle 1s^P(1)2l^P(2) | -\frac{Z^P}{r_2} | 1s^P(1)1s^T(2) \rangle + \langle 1s^P(1)2l^P(2) | \frac{1}{r_{21}} | 1s^P(1)1s^T(2) \rangle = \\
& \langle 1s^P | 1s^P \rangle \langle 2l^P | -\frac{Z^P}{r_2} | 1s^T \rangle + \langle 1s^P(1)2l^P(2) | \frac{1}{r_{21}} | 1s^P(1)1s^T(2) \rangle = \\
& I_{2l^P 1s^T} + \langle 1s^P(1)2l^P(2) | \frac{1}{r_{21}} | 1s^P(1)1s^T(2) \rangle
\end{aligned}$$

so that

$$\textcircled{1} \rightarrow I_{2\bar{2}} + \langle 1\bar{2} | \frac{1}{r_{21}} | 1\bar{2} \rangle \quad (3.10)$$

where we use a shorthand notation with $1 \equiv 1s^P$, $2 \equiv 2l^P$ and $\bar{2} \equiv 1s^T$. Equivalently, we have for the three other terms,

$$\begin{aligned}
& \textcircled{2} \rightarrow \langle 1s^P(1)2l^P(2) | -\frac{Z^P}{r_1} + \frac{1}{r_{12}} | 1s^T(1)1s^P(2) \rangle = \\
& \langle 1s^P(1)2l^P(2) | -\frac{Z^P}{r_1} | 1s^T(1)1s^P(2) \rangle + \langle 1s^P(1)2l^P(2) | \frac{1}{r_{12}} | 1s^T(1)1s^P(2) \rangle = \\
& \langle 1s^P | -\frac{Z^P}{r_1} | 1s^T \rangle \underbrace{\langle 2l^P | 1s^P \rangle}_0 + \langle 1s^P(1)2l^P(2) | \frac{1}{r_{12}} | 1s^T(1)1s^P(2) \rangle = \\
& \langle 1s^P(1)2l^P(2) | \frac{1}{r_{12}} | 1s^T(1)1s^P(2) \rangle
\end{aligned}$$

and therefore

$$\textcircled{2} \rightarrow \langle 1\bar{2} | \frac{1}{r_{12}} | \bar{2}1 \rangle, \quad (3.11)$$

$$\begin{aligned}
& \textcircled{3} \rightarrow \langle 2l^P(1)1s^P(2) | -\frac{Z^P}{r_2} + \frac{1}{r_{12}} | 1s^P(1)1s^T(2) \rangle = \\
& \langle 2l^P(1)1s^P(2) | -\frac{Z^P}{r_2} | 1s^P(1)1s^T(2) \rangle + \langle 2l^P(1)1s^P(2) | \frac{1}{r_{21}} | 1s^P(1)1s^T(2) \rangle = \\
& \underbrace{\langle 2l^P | 1s^P \rangle}_0 \langle 1s^P | -\frac{Z^P}{r_2} | 1s^T \rangle + \langle 2l^P(1)1s^P(2) | \frac{1}{r_{21}} | 1s^P(1)1s^T(2) \rangle = \\
& \langle 2l^P(1)1s^P(2) | \frac{1}{r_{21}} | 1s^P(1)1s^T(2) \rangle
\end{aligned}$$

and therefore

$$\textcircled{3} \rightarrow \langle \bar{2}1 | \frac{1}{r_{21}} | 1\bar{2} \rangle, \quad (3.12)$$

$$\begin{aligned}
\textcircled{4} &\rightarrow \langle 2l^P(1)1s^P(2) | -\frac{Z^P}{r_1} + \frac{1}{r_{12}} | 1s^T(1)1s^P(2) \rangle = \\
&\langle 2l^P(1)1s^P(2) | -\frac{Z^P}{r_1} | 1s^T(1)1s^P(2) \rangle + \langle 2l^P(1)1s^P(2) | \frac{1}{r_{12}} | 1s^T(1)1s^P(2) \rangle = \\
&\langle 2l^P | -\frac{Z^P}{r_1} | 1s^T \rangle \langle 1s^P | 1s^P \rangle + \langle 2l^P(1)1s^P(2) | \frac{1}{r_{12}} | 1s^T(1)1s^P(2) \rangle = \\
&I_{2l^P 1s^T} + \langle 2l^P(1)1s^P(2) | \frac{1}{r_{12}} | 1s^T(1)1s^P(2) \rangle
\end{aligned}$$

and consequently

$$\textcircled{4} \rightarrow I_{2\bar{2}} + \langle 21 | \frac{1}{r_{12}} | \underline{21} \rangle. \quad (3.13)$$

Hence the M_{fi}^\pm is given by

$$M_{fi}^\pm = \frac{1}{2} \left[I_{2\bar{2}} + \langle 12 | \frac{1}{r_{21}} | \underline{12} \rangle \pm \langle 12 | \frac{1}{r_{12}} | \underline{21} \rangle \pm \langle 21 | \frac{1}{r_{21}} | \underline{12} \rangle + I_{2\bar{2}} + \langle 21 | \frac{1}{r_{12}} | \underline{21} \rangle \right] \quad (3.14)$$

and making use of the indistinguishability of the two electrons,

$$\begin{aligned}
\langle 12 | \frac{1}{r_{21}} | \underline{12} \rangle &= \langle 1s^P(1)2l^P(2) | \frac{1}{r_{21}} | 1s^P(1)1s^T(2) \rangle = \\
&\langle 2l^P(1)1s^P(2) | \frac{1}{r_{12}} | 1s^T(1)1s^P(2) \rangle = \langle 21 | \frac{1}{r_{12}} | \underline{21} \rangle
\end{aligned} \quad (3.15)$$

$$\begin{aligned}
\langle 12 | \frac{1}{r_{12}} | \underline{21} \rangle &= \langle 1s^P(1)2l^P(2) | \frac{1}{r_{12}} | 1s^T(1)1s^P(2) \rangle = \\
&\langle 2l^P(1)1s^P(2) | \frac{1}{r_{21}} | 1s^P(1)1s^T(2) \rangle = \langle 21 | \frac{1}{r_{21}} | \underline{12} \rangle,
\end{aligned} \quad (3.16)$$

one gets

$$M_{fi}^\pm = I_{2\bar{2}} + \langle 12 | \frac{1}{r_{21}} | \underline{12} \rangle \pm \langle 12 | \frac{1}{r_{12}} | \underline{21} \rangle \quad (3.17)$$

where the mono-electronic integral $I_{2\bar{2}} = \langle 2l^P | -\frac{Z^P}{r_1} | 1s^T \rangle$, carries also an ETF, while the bielectronic integrals are expressed by

$$\langle 12 | \frac{1}{r_{21}} | \underline{12} \rangle = \int \int d\vec{r}_1 d\vec{r}_2 1s^{P*}(1)2l^{P*}(2) \frac{e^{-i\vec{v}_P \cdot \vec{r}_2}}{r_{12}} 1s^P(1)1s^T(2) \quad (3.18)$$

$$\langle 12 | \frac{1}{r_{21}} | \underline{21} \rangle = \int \int d\vec{r}_1 d\vec{r}_2 1s^{P*}(1)2l^{P*}(2) \frac{e^{-i\vec{v}_P \cdot \vec{r}_1}}{r_{12}} 1s^T(1)1s^P(2). \quad (3.19)$$

where we include explicitly the ETF phase. The two latter integrals can be described as analogues to the *Coulomb* and *exchange* integrals for many electron systems (Szabo [85], p. 85).

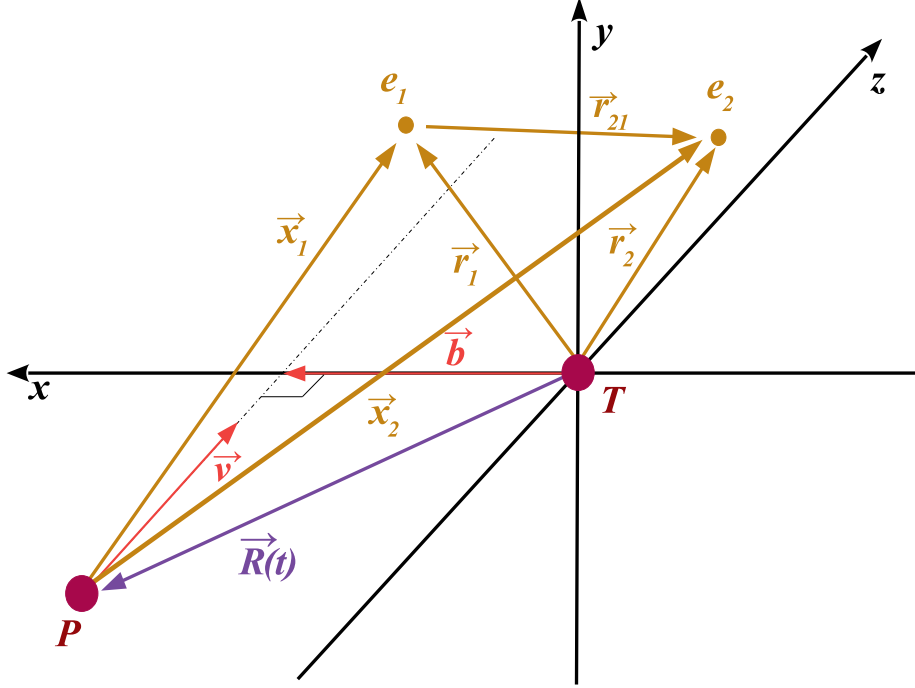


FIGURE 3.8: The ion-atom collision geometry. The impact parameter \vec{b} and velocity \vec{v}_P define the xz plane, that is the collision plane and $\vec{R}(t)$ symbolises the trajectory that the projectile follows in respect to the target. Vectors $\vec{r}_1(\vec{x}_1)$, $\vec{r}_2(\vec{x}_2)$ and \vec{r}_{12} represent the positions of the two electrons, e_1 , e_2 with respect to the target (projectile) and the relative vector between them.

When analysing eq. 3.17, one can observe that the couplings between the initial state and the final, singlet and triplet, states differ only by the third term. Since the second and third terms have quite similar expressions and their values depend on various parameters as \vec{R} , \vec{v} and the expression of the orbitals $1s^P$, $2s^P$ and $1s^T$, we are going to express them approximatively in the following. We introduce two series of position vectors for the two electrons, as shown in Figure 3.8. Then one can see easily that $\vec{r}_1 = \vec{x}_1 + \vec{R}$ so that

$$\vec{r}_{21} = \vec{r}_2 - \vec{r}_1 \Rightarrow \vec{r}_{21} = \vec{r}_2 - \vec{x}_1 - \vec{R}. \quad (3.20)$$

We can then express the distance between the two electrons as

$$\begin{aligned} r_{12}^2 &= (\vec{r}_2 - \vec{x}_1)^2 + R^2 - 2(\vec{r}_2 - \vec{x}_1) \cdot \vec{R} = \\ &R^2 \left(1 + \frac{(\vec{r}_2 - \vec{x}_1)^2}{R^2} - \frac{2}{R} (\vec{r}_2 - \vec{x}_1) \cdot \hat{u}_R \right), \end{aligned} \quad (3.21)$$

with \hat{u}_R a unit vector in the direction of \vec{R} . Then the two-centre interelectronic repulsion term in the "Coulomb" and "exchange" integrals can be written as

$$\frac{1}{r_{21}} = \frac{1}{R} \left(1 + \frac{(\vec{r}_2 - \vec{x}_1)^2}{R^2} - \frac{2}{R} (\vec{r}_2 - \vec{x}_1) \cdot \hat{u}_R \right)^{-1/2}. \quad (3.22)$$

Making use of the Taylor expansion

$$\frac{1}{\sqrt{1+x}} = 1 - \frac{1}{2}x + \frac{3}{8}x^2 + \mathcal{O}(x^3) \quad (3.23)$$

the operator can be expressed as

$$\begin{aligned} \frac{1}{r_{21}} = \frac{1}{R} & \left(\underbrace{1}_{1^{st} \text{ order}} - \underbrace{\frac{1}{2} \left(\frac{(\vec{r}_2 - \vec{x}_1)^2}{R^2} - \frac{2}{R} (\vec{r}_2 - \vec{x}_1) \cdot \hat{u}_R \right)}_{2^{nd} \text{ order}} + \right. \\ & \left. \underbrace{\frac{3}{8} \left(\frac{(\vec{r}_2 - \vec{x}_1)^2}{R^2} - \frac{2}{R} (\vec{r}_2 - \vec{x}_1) \cdot \hat{u}_R \right)^2}_{3^{rd} \text{ order}} + \dots \right) \end{aligned} \quad (3.24)$$

that is

$$\frac{1}{r_{21}} = \frac{1}{R} + \frac{1}{R^2} (\vec{r}_2 - \vec{x}_1) \cdot \hat{u}_R + \frac{1}{2R^3} \left[3 [(\vec{r}_2 - \vec{x}_1) \cdot \hat{u}_R]^2 - (\vec{r}_2 - \vec{x}_1)^2 \right] + \mathcal{O}\left(\frac{1}{R^4}\right). \quad (3.25)$$

Equivalently for the $\vec{r}_2 = \vec{x}_2 + \vec{R}$,

$$\vec{r}_{12} = \vec{r}_1 - \vec{r}_2 = \vec{r}_1 - \vec{x}_2 - \vec{R} \quad (3.26)$$

and the repulsion term $\frac{1}{r_{12}}$ is given by

$$\frac{1}{r_{12}} = \frac{1}{R} + \frac{1}{R^2} (\vec{r}_1 - \vec{x}_2) \cdot \hat{u}_R + \frac{1}{2R^3} \left[3 [(\vec{r}_1 - \vec{x}_2) \cdot \hat{u}_R]^2 - (\vec{r}_1 - \vec{x}_2)^2 \right] + \mathcal{O}\left(\frac{1}{R^4}\right). \quad (3.27)$$

The "coulomb equivalent" integral (eq. 3.18), keeping the first and the second terms of eq. 3.25 becomes

$$\begin{aligned} \langle 12 | \frac{1}{r_{21}} | 21 \rangle = & \underbrace{\frac{1}{R} \int \int d\vec{r}_1 d\vec{r}_2 1s^{P^*}(\vec{x}_1) 2l^{P^*}(\vec{x}_2) e^{-i\vec{v} \cdot \vec{r}_2} 1s^P(\vec{x}_1) 1s^T(\vec{r}_2)}_{\textcircled{1}} \\ & + \underbrace{\frac{\hat{u}_R}{R^2} \cdot \int \int d\vec{r}_1 d\vec{r}_2 1s^{P^*}(\vec{x}_1) 2l^{P^*}(\vec{x}_2) e^{-i\vec{v} \cdot \vec{r}_2} (\vec{r}_2 - \vec{x}_1) 1s^P(\vec{x}_1) 1s^T(\vec{r}_2)}_{\textcircled{2}} \end{aligned} \quad (3.28)$$

with (making use of $d\vec{r}_{r_i} \equiv d\vec{r}_{x_i}$)

$$\textcircled{1} = \frac{1}{R} \int \underbrace{d\vec{r}_1 1s^{P*}(\vec{x}_1) 1s^P(\vec{x}_1)}_1 \times \int d\vec{r}_2 2l^{P*}(\vec{x}_2) e^{-i\vec{v}\cdot\vec{r}_2} 1s^T(\vec{r}_2) = \frac{1}{R} S_{22} \quad (3.29)$$

$$\begin{aligned} \textcircled{2} &= \frac{\hat{u}_R}{R^2} \cdot \left(\int d\vec{r}_2 2l^{P*}(\vec{x}_2) \vec{r}_2 1s^T(\vec{r}_2) \times \int d\vec{r}_1 1s^{P*}(\vec{x}_1) 1s^P(\vec{x}_1) \right. \\ &\quad \left. - \int d\vec{r}_2 2l^{P*}(\vec{x}_2) e^{-i\vec{v}\cdot\vec{r}_2} 1s^T(\vec{r}_2) \times \underbrace{\int d\vec{r}_1 1s^{P*}(\vec{x}_1) \vec{x}_1 1s^P(\vec{x}_1)}_0 \right) = \\ &\quad \frac{\hat{u}_R}{R^2} \cdot \int d\vec{r}_2 2l^{P*}(\vec{x}_2) e^{-i\vec{v}\cdot\vec{r}_2} \vec{r}_2 1s^T(\vec{r}_2) \end{aligned} \quad (3.30)$$

and finally

$$\langle 12 | \frac{1}{r_{21}} | 12 \rangle = \frac{1}{R} \int d\vec{r}_2 2l^{P*}(\vec{x}_2) e^{-i\vec{v}\cdot\vec{r}_2} \underline{1s}^T(\vec{r}_2) + \frac{\hat{u}_R}{R^2} \cdot \int d\vec{r}_2 2l^{P*}(\vec{x}_2) \vec{r}_2 1s^T(\vec{r}_2) \quad (3.31)$$

Following the same treatment, the "exchange" integral in eq. 3.19, keeping the first two terms of eq. 3.27, can be expressed as

$$\begin{aligned} \langle 12 | \frac{1}{r_{21}} | 21 \rangle &= \frac{1}{R} \int \int \underbrace{d\vec{r}_1 d\vec{r}_2 1s^{P*}(\vec{x}_1) e^{-i\vec{v}\cdot\vec{r}_1} 2l^{P*}(\vec{x}_2) 1s^T(\vec{r}_1) 1s^P(\vec{x}_2)}_{\textcircled{1}} \\ &\quad + \frac{\hat{u}_R}{R^2} \cdot \int \int \underbrace{d\vec{r}_1 d\vec{r}_2 1s^{P*}(\vec{x}_1) 2l^{P*}(\vec{x}_2) (\vec{r}_1 - \vec{x}_2) e^{-i\vec{v}\cdot\vec{r}_1} 1s^T(\vec{r}_1) 1s^P(\vec{x}_2)}_{\textcircled{2}} \end{aligned} \quad (3.32)$$

with

$$\textcircled{1} = \frac{1}{R} \int d\vec{r}_1 1s^{P*}(\vec{x}_1) e^{-i\vec{v}\cdot\vec{r}_1} 1s^T(\vec{r}_1) \times \underbrace{\int d\vec{r}_2 2l^{P*}(\vec{x}_2) 1s^P(\vec{x}_2)}_0 = 0 \quad (3.33)$$

$$\begin{aligned} \textcircled{2} &= \frac{\hat{u}_R}{R^2} \cdot \left(\int d\vec{r}_1 1s^{P*}(\vec{x}_1) \vec{r}_1 1s^T(\vec{r}_1) \times \int d\vec{r}_2 2l^{P*}(\vec{x}_2) 1s^P(\vec{x}_2) \right. \\ &\quad \left. - \int d\vec{r}_1 1s^{P*}(\vec{x}_1) e^{-i\vec{v}\cdot\vec{r}_1} 1s^T(\vec{r}_1) \times \int d\vec{r}_2 2l^{P*}(\vec{x}_2) \vec{x}_2 1s^P(\vec{x}_2) \right) = \\ &\quad - \frac{\hat{u}_R}{R^2} \cdot S_{12} \int d\vec{r}_2 2l^{P*}(\vec{x}_2) \vec{x}_2 1s^P(\vec{x}_2) \end{aligned} \quad (3.34)$$

and finally

$$\langle 12 | \frac{1}{r_{21}} | 21 \rangle = - \frac{\hat{u}_R}{R^2} \cdot \int d\vec{r}_1 1s^{P*}(\vec{x}_1) e^{-i\vec{v}\cdot\vec{r}_1} 1s^T(\vec{r}_1) \times \int d\vec{r}_2 2l^{P*}(\vec{x}_2) \vec{x}_2 1s^P(\vec{x}_2). \quad (3.35)$$

Eventually, using equations 3.31 and 3.35, the coupling matrix elements of the process take the form

$$M_{fi}^{\pm} \approx \int d\vec{r}_1 2l^P(1) \left(-\frac{Z^P}{r_1}\right) 1s^T(1) + \frac{1}{R} S_{22} + \frac{\hat{u}_R}{R^2} \cdot \int d\vec{r}_2 2l^{P*}(\vec{x}_2) \vec{r}_2 1s^T(\vec{r}_2) \pm \frac{\hat{u}_R}{R^2} S_{12} \cdot \int d\vec{r}_2 2l^{P*}(\vec{x}_2) \vec{x}_2 1s^P(\vec{x}_2). \quad (3.36)$$

Note that we retain only the first and second terms in the expansion in $\frac{1}{R}$ since, at the high impact energies we consider ($E > 100$ keV/u), the process is only likely for rather low values of internuclear distance for which these terms are dominant. As mentioned before, the differences between the singlet and triplet cases, are related in our approximation to the last term. Then, analysing the latter, one can see in eq. 3.36 that it is proportional to a dipolar type integral which exactly cancels when $\Delta l \neq \pm 1$. Therefore this term is exactly zero for $2l \equiv 2s$ (and equivalently for the M-shell $3l \equiv 3s$ or $3l \equiv 3d$) but not for $2p$ (or $3p$). This simple model explains therefore qualitatively the surprising difference between the cross sections for production of $1s2p \ ^1P$ and $1s2p \ ^3P$ (as well as $1s3s \ ^1,^3P$) at high impact energies. However, another issue remains to be clarified, that is whether the last term which explains the difference between singlet and triplet is negligible compared to the two first and especially the first whose contribution may be easily tunable, since depending on the charge of the projectile Z_P .

To get further insight to the spin anisotropy effect, we have therefore performed further calculations with hydrogen-like projectiles, He^+ , B^{4+} and C^{5+} to investigate, i) the generality of the effect and ii) the contribution of the first term with respect to the third in eq. 3.17. Additionally, we performed further calculations at higher impact energies regarding the Li^{2+} - H collision system⁴. For the high impact velocity collisions we have created new GTO basis sets which are given in Appendix A. All the projectiles are based on a set of 56 GTOs (12 for $l = 0$, $8 \times 3 = 24$ for $l = 1$ and $4 \times 5 = 20$ for $l = 2$) while the target on a set of 45 GTOs (12 for $l = 0$, $6 \times 3 = 18$ for $l = 1$ and $3 \times 5 = 15$ for $l = 2$). This group of calculations includes: for He^+ 1869 (931 TP and 938 PP states)⁵, for Li^{2+} 1654 (935 TP and 719 PP states), for B^{4+} 1574 (891 TP and 683 PP states) and for C^{5+} 1550 (889 TP and 661 PP) states and represent thousands of hours of computation. In Table 3.2 the energies of the important

⁴The new basis set, used in the high impact energies velocities, converge with the main basis set ($B_1^{H,Li}$) of this chapter at $\approx 1\%$

⁵Note that TP stands for the two electrons shared by the target and the projectile while PP stands for both electrons attached on the projectile.

states we focus regarding the projectiles, He^+ , B^{4+} , C^{5+} ions are presented. The quality of the energies for the three new systems is very similar to the ones obtained for Li^+ , presented in 3.1.

TABLE 3.2: Comparison of energies, in a.u., of the He atom, B^{3+} and C^{4+} ions, triplet and singlet states, based on the GTO basis set. We include the NIST data for comparison.

| | State | E_{GTO} | E_{NIST} | $\Delta(\%)*$ | State | E_{GTO} | E_{NIST} | $\Delta(\%)*$ |
|-----------------|-------------|-----------|------------|---------------|-------------|-----------|------------|---------------|
| He | $1s2s\ ^1S$ | -2.1456 | -2.1458 | 0.015 | $1s2s\ ^3S$ | -2.1751 | -2.1750 | 0.004 |
| | $1s2p\ ^1P$ | -2.1236 | -2.1236 | 0.001 | $1s2p\ ^3P$ | -2.1331 | -2.1330 | 0.008 |
| | $1s2s\ ^1S$ | -2.0476 | -2.0611 | 0.056 | $1s3s\ ^3S$ | -2.0609 | -2.0685 | 0.366 |
| | $1s3p\ ^1P$ | -2.0398 | -2.0550 | 0.737 | $1s3p\ ^3P$ | -2.0465 | -2.0579 | 0.092 |
| | $1s3d\ ^1D$ | -2.0207 | -2.0554 | 1.686 | $1s3d\ ^3D$ | -2.0208 | -2.0554 | 1.690 |
| B^{3+} | $1s2s\ ^1S$ | -14.5776 | -14.5820 | 0.030 | $1s2s\ ^3S$ | -14.7331 | -14.7377 | 0.004 |
| | $1s2p\ ^1P$ | -14.4759 | -14.4805 | 0.032 | $1s2p\ ^3P$ | -14.5726 | -14.5765 | 0.027 |
| | $1s2s\ ^1S$ | -13.4078 | -14.4153 | 0.056 | $1s3s\ ^3S$ | -13.4500 | -13.4564 | 0.047 |
| | $1s3p\ ^1P$ | -13.3805 | -13.3859 | 0.040 | $1s3p\ ^3P$ | -13.4087 | -13.4132 | 0.034 |
| | $1s3d\ ^1D$ | -13.3454 | -13.3922 | 0.350 | $1s3d\ ^3D$ | -13.3464 | -13.3929 | 0.347 |
| C^{4+} | $1s2s\ ^1S$ | -21.2207 | -21.2301 | 0.044 | $1s2s\ ^3S$ | -21.4194 | -21.4294 | 0.047 |
| | $1s2p\ ^1P$ | -21.0916 | -21.1009 | 0.044 | $1s2p\ ^3P$ | -21.2210 | -21.2295 | 0.040 |
| | $1s2s\ ^1S$ | -19.4779 | -19.4137 | 0.058 | $1s3s\ ^3S$ | -19.4671 | -19.4749 | 0.056 |
| | $1s3p\ ^1P$ | -19.3786 | -19.3877 | 0.047 | $1s3p\ ^3P$ | -19.4154 | -19.4240 | 0.044 |
| | $1s3d\ ^1D$ | -19.3399 | -19.3961 | 0.290 | $1s3d\ ^3D$ | -19.3413 | -19.3971 | 0.288 |

$$* \Delta = |(E_{GTO} - E_{NIST})/E_{NIST}| \times 100$$

For the three new collision systems and Li^{2+} - H collisions we present in Figures 3.9 and 3.10 the ratio of the cross sections for triplet and singlet states for production of $1snl$ configuration with $n = 2$ and 3, respectively.

Regarding transfer to $2l$, Figure 3.9 shows the ratio of the cross sections in triplet and singlet for S state production is close to 1 for the four collision systems. On the other hand, for P states this trend differs significantly from unity, with capture for the triplet states largely dominating. The features observed for Li^{2+} - H collision at high energy is therefore of general nature and not a peculiarity of this system, supporting our approximate treatment (eq 3.36). However the ratio covers gradually different ranges: it extends up to the value of ≈ 9 for He^+ projectile while it does not exceed ≈ 1.5 for C^{5+} projectile. This illuminates the relative magnitude of the 4^{th} (inducing triplet and singlet difference) and 1^{st} term in eq. 3.36. For increasing of Z_P this latter gets larger, reducing the effect of the 4^{th} , which corresponds to the interelectronic repulsion.

The results presented in Figure 3.10 for transfer to $3l$ show the same tendency, i.e. large differences between triplet and singlet, from ≈ 10 down gradually to ≈ 1.5 , for P state production. On the other hand, for S and D states

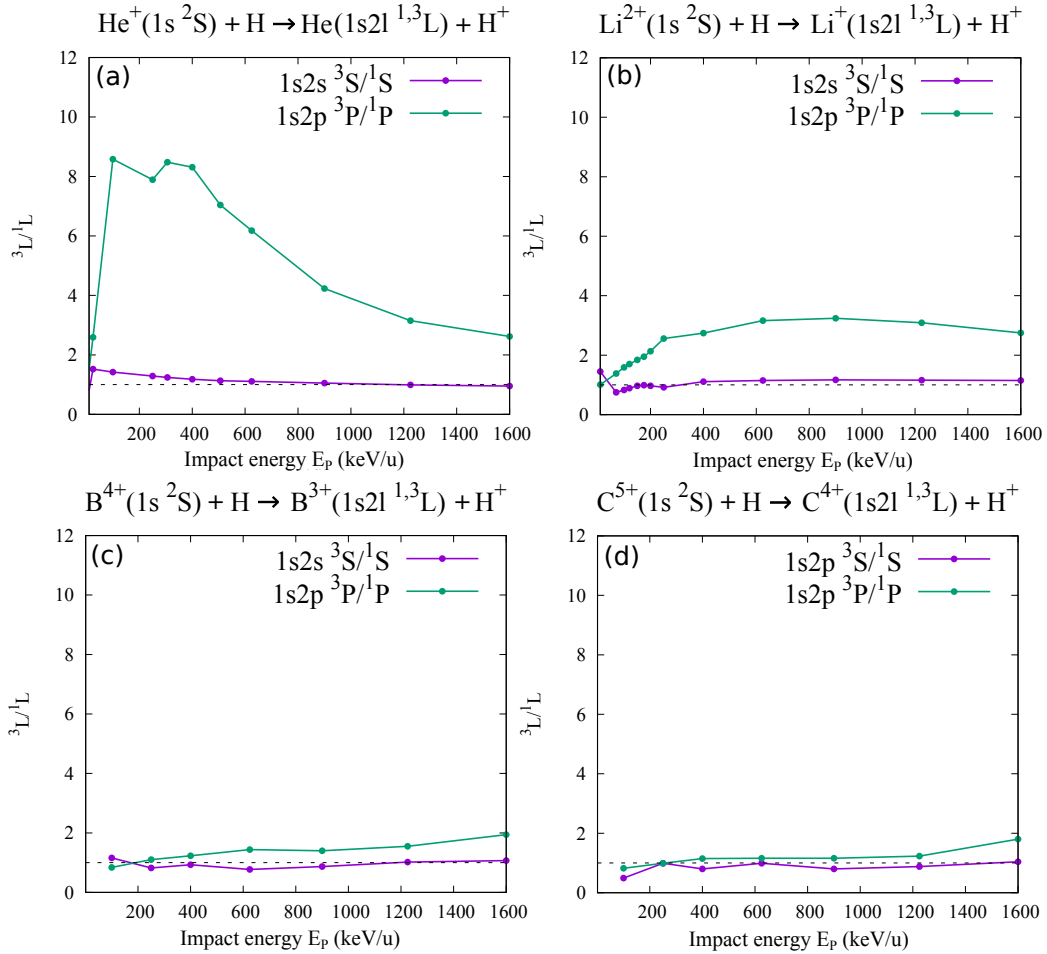


FIGURE 3.9: The ${}^3L/{}^1L$ cross sections for production of $1s2l$ configuration in He^+ , Li^{2+} , B^{4+} , C^{5+} colliding with H.

the ratio is close to unity, as expected by our model.

Finally one can observe that the variation with the energy is different for the four collision systems. Focusing to the high impact energies in Figures 3.9 and 3.10 it is observed that, after the peak, the $\frac{{}^3P}{{}^1P}$ ratio for He and Li^+ begin to decrease again. This can be attributed to the ETF (eq. 2.33) which are included in the anisotropy term $\pm \frac{\hat{u}_R}{R^2} S_{12} \cdot \int d\vec{r}_2 2l^{P*}(\vec{x}_2) \vec{x}_2 1s^P(\vec{x}_2)$. As the collision velocity increases, the ETF must drive the anisotropy term to zero exponentially, reducing, therefore, the $\frac{{}^3P}{{}^1P}$ ratio to ≈ 1 . Additionally the shift of the peak location to higher energies from helium to lithium, projectile He shows the dependencies of the overlap S_{12} on the size of the atom. For example, He, of atomic radius 31 pm, gets the ratio peak at ≈ 200 keV/u (and the $1s3p$ ratio peak at ≈ 400 keV/u) while Li^+ , of ionic radius 90 pm, gets the peak at ≈ 1000 keV/u for both capture to $n = 2$ and 3. At the same specific energy, the overlap between lithium and hydrogen shall be larger, sustaining the anisotropy term

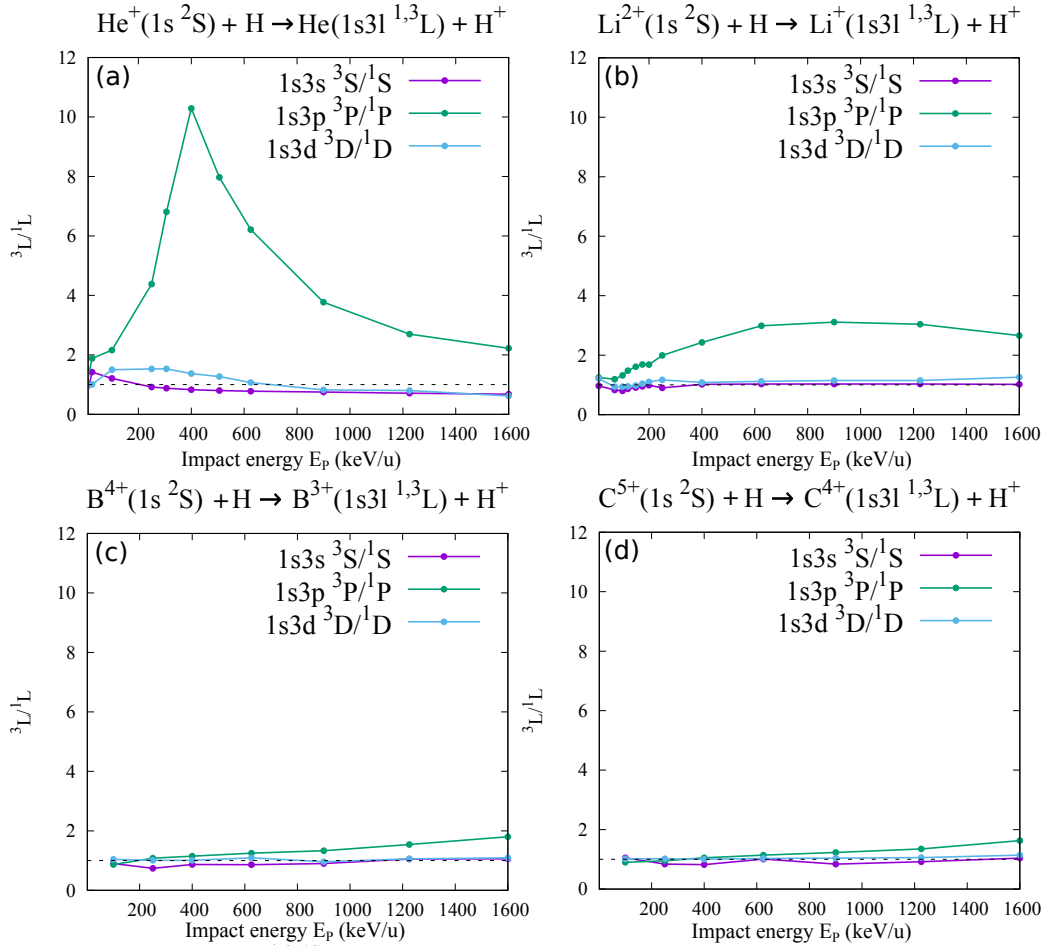


FIGURE 3.10: The ${}^3L/{}^1L$ cross sections for production of $1s3l$ configuration in He^+ , Li^{2+} , B^{4+} , C^{5+} colliding with H.

and, therefore, the $\frac{{}^3P}{{}^1P}$ ratio higher.

Finally, note also that we expand our calculations to the highest projectile energy (1600 keV/u. i.e. $v_P = 8$ a.u.) before severe numerical instabilities appear and forbid further calculations. There is a known drawback of close-coupling calculations when reaching perturbative regime where, the cross sections are very small, the process occurring significantly only at low impact parameters, e.g. $b < 1$ a.u. for S channels.

3.3.3 Electron excitation

As mentioned in the introduction of this chapter, the basis sets we used in the calculations are very large and contain many states describing capture but also target excitation. Since cross sections for this latter process exist in the literature, it is interesting to include them to our results. We, therefore, present in Figure 3.11 the cross sections of excitation of the H target into the $n = 2$,

$n = 3$ and $n = 4$ shells. We also show the results of Liu et al. [79] and Ramirez et al. [86], both investigations being based on one-electron models, the first in a close-coupling approach while the second within a perturbative symmetric eikonal one. The result of the latter agrees fairly well with ours for $H(n = 2)$ production in the range where the two series of data overlap. i.e. from 40 to 250 keV/u.

For these excitation channels our cross sections show oscillations, with three local maxima, also present in the results of Liu [79]. These structures can be due to different mechanisms, from molecular to direct ones, and also to the selectivity of the excitation to $2s$ and $2p$ as function of energy. One could advocate the swap interpretation described in Hansen et al. ([87] and references therein). However the agreement with Liu's cross sections is not excellent and worsens for decreasing energies. For excitation to higher shells, the agreement is also qualitative but the cross sections show also oscillations in both studies. Further studies should be performed to understand these oscillations.

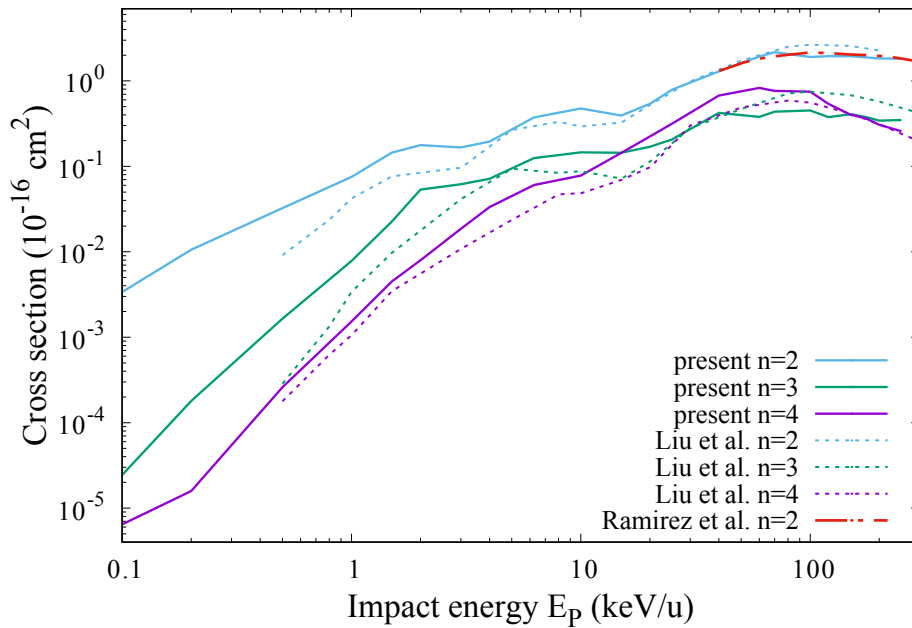


FIGURE 3.11: Shell selective cross sections for excitation of the H atom in the Li^{2+} - $H(1s)$ collisions. Our present calculations are in light blue, green and purple solid lines for $n = 2$, $n = 3$ and $n = 4$, respectively along with Liu et al. [79] (keeping the same colour pattern) and Ramirez et al. [86] in red dash-dot line for $n = 2$.

3.4 Conclusion

In this chapter capture and excitation in $\text{Li}^{2+} - \text{H}(1s)$ collisions have been studied by using the two-active-electron SCAOCC approach presented in Chapter 2. Using large basis sets, allowing the evaluation of well converged cross sections, total and state-selective are presented in a wide energy domain, 0.1 - 250 keV/u. The present results agree well with previous available experimental data [74, 75] and theoretical calculations [76–82] in their respective energy range. Our study extends the calculations to impact energies as low as 0.1 keV/u where it is observed that the capture to $n = 2$ dominates and determine the total capture cross section. The sub-shell results show that the triplet states become dominant with cross section up to more than 10^3 larger than the singlet ones for capture, both in $n = 2$ and $n = 3$ shells. Independent calculations and experimental work would be useful to validate the cross sections in this energy range.

Additionally, we have studied the asymmetry spin effect we encounter in electron transfer to P states for high collision energies, not present in S or D ones. An OBK model has been developed for the needs of understanding of this high velocity feature. Additional calculations for different hydrogenic projectiles present the same spin asymmetry, which seems of general nature and not accidental. This series of results validate the illustrative model developed during this thesis, validating the interplay between two-centre two-electron coupling, which explains the asymmetry, and direct coupling, which involves mainly the charge of the projectile.

Chapter 4

Multielectronic processes in helium-like ion – He collisions

4.1 Introduction

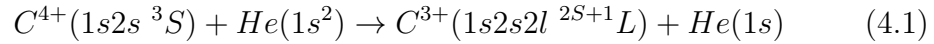
Ion-impact research provides a detailed insight into the structure and dynamics of atoms and molecules, neutral or ionised [88,89]. It also provides fundamental information on the processes occurring when these objects interact, i.e. charge transfer, excitation, ionisation, as well as the combinations of the aforementioned, while, simultaneously, supplying data of importance for other domains and applied research, such as laboratory and astrophysical plasmas, controlled thermonuclear fusion, radiation damage concerning the biological tissue [90,91]. An important issue in this context is the description of multi-electronic collision systems and processes, when the electronic correlation plays an important role. An interesting but complex object of study is the production of doubly excited states which decay, after the scattering event, radiatively or by Auger electron emission which can be detected experimentally.

In this context, we have conducted a project concerning collisions between helium-like ions, i.e. C^{4+} , O^{6+} , F^{7+} and He targets in the MeV energy range. This investigation was carried out in collaboration with a group of experimentalists of University of Crete and University of Ioannina and the difficulties encountered by our co-workers have impacted considerably our investigation. Indeed when producing helium-like ions in accelerators, a significant proportion of the ions in the beam are in low lying, long lived, excited states. We have, therefore, considered collisions with helium targets for both ground and excited state projectiles. These latter present several further difficulties compared to ground state systems. Firstly, they involve several open shell electronic states and therefore, several total spin symmetries. Secondly, since located much above the ground state, the scattering event may induce transitions with a

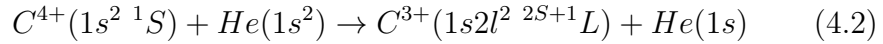
much larger number of states, implying, for modelling, the use of basis sets of much larger size. The ions in the beams are considered to be in mixed states as explained in [29, 92, 93]: in particular the three states considered taking place in the initial projectile beams are the ground state $1s^2\ ^1S$ and the two excited metastable states $1s2s\ ^1,^3S$. The percentage of the three initial states, present when the scattering takes place, varies, depending on the life-time of the metastable states, as well as with the impact velocity of the collision.

In the following we are going to present results for three different electronic processes induced in three different collision systems: as for example, using C^{4+} and O^{6+} projectiles, these processes which produce doubly excited states are the following:

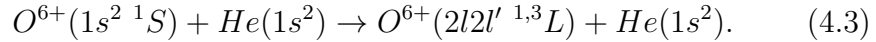
- electron transfer or single electron capture (SEC),



- transfer-excitation (TE),



- excitation¹,



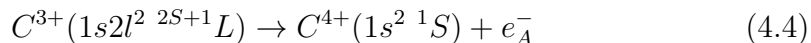
These processes have been thoroughly investigated experimentally in the same context but interpreted only by simple models, with the use of one-electron treatment, and very rare multi-electron treatments. Before presenting our results we are going to briefly resume some of the interpretations used in the past.

4.2 Transfer-Excitation

As mentioned in the introduction of the thesis, although the main processes in an ion-atom collision are transfer (electron capture), excitation and ionisation, any combination of these may take place within the collision time. For example, in collisions between an ion and an atom, charge transfer alongside projectile inner-shell excitation can occur in a single event resulting in the formation of a doubly excited state [94, 95].

¹This processes is presented only for oxygen projectile in this thesis.

The combined transfer and excitation can result predominantly from electron-electron (e-e) and/or from electron-nucleus (e-n) interactions. In this context, a first mechanism, the so-called Resonant Transfer-Excitation (RTE), was advocated in the past and is related to electron correlation effect, with a direct analogy to an inverse Auger effect: taking the example of eq. 4.1 the corresponding inverse Auger emission is



neglecting the binding of the electron on He. Then a condition of resonance is obtained if the relative velocity between target and projectile is approximately equal to the Auger electron velocity, $v_P \approx v_{e_A}$, resulting in an impact energy for which the transfer-excitation process is maximum, giving the name RTE to this peak. A second mechanism of interest in this thesis, the so-called Non-resonant Transfer-Excitation (NTE), involves independent, successive, capture and excitation processes in a single encounter.

The up-to-date but rather old theoretical description of TE within coherent approaches, has proven to be problematic, primarily due to the difficulty of including several electrons and both e-e and e-n interactions within the same dynamical multi-electron treatment [96,97]. Only two such treatments have appeared so far in which the signatures of RTE and NTE have been sought, both for collisions of one-electron projectiles with one-electron targets: (i) the two-electron atomic orbital close-coupling (CC) treatment [98] and (ii) the perturbative continuous distorted wave four-body (CDW-4B) approach [99–101]. The CC calculations, were carried out for the benchmark near symmetric $\text{He}^+(1s) - \text{H}(1s)$ system. Stemming from a minimal basis sets CC, the cross sections for the dominant $\text{He}(2p^2\ ^1D)$ RTE resonance were found to be much larger than measurements for an H_2 target (see [102] and Figure 6 in [92]). Nevertheless, this approach showed the way for such exact non perturbative TE treatments while introducing a model to assess the NTE contributions using an independent event approximation. However, the results shown were rather partial and not convincing. The CDW-4B approach, was applied primarily to highly asymmetric systems, e.g. $\text{S}^{15+} - \text{H}$ [99] while the cross sections were compared for the RTE peak from low resolution x-ray measurements making an accurate quantitative interpretation difficult. On the other hand, the NTE peak was too low in collision energy to be described by CDW-4B. This approach was also applied to the $\text{He}^+ - \text{He}$ [100, 103] and $\text{He}^+(1s) - \text{H}(1s)$ systems [101], but found to disagree strongly with both experiment and the previous CC results. To date,

no further attempts have been made to provide a comprehensive coherent treatment of TE. The next sub-sections will present in more detail the processes of electron transfer as well as electron transfer-excitation.

4.2.1 Resonant Transfer-Excitation

RTE is a correlated two-electron process, produced by an electron-electron (e-e) interaction [104], [see Figure 4.1], following the image of an inverse Auger effect. As mentioned before, it involves the transfer of an electron of the target to the projectile and the simultaneous excitation of a projectile electron to a doubly-excited state of the latter. The doubly-excited states relax either by photon emission and they are studied by x-ray spectroscopy (RTEX) or by non-radiative electron ejection, studied by Auger spectroscopy (RTEA).

RTE is identified by its resonant behaviour, when the cross section undergoes a maximum. The signature of RTEA is therefore expected to be a peak in the Transfer-Excitation cross section, appearing at energy corresponding to the resonance condition described before when the projectile velocity equals the Auger electron velocity. However, following quantitatively the inverse Auger effect, one should consider the momentum distribution of the electron in target, which broadens the RTE peak. The narrower the momentum distribution, or Compton profile of the target electron, the sharper is the RTE maximum in the TE cross section. Thus, light two-electron targets, such as H₂ and He, are desirable for RTE study due to their narrow momentum distribution. [92].

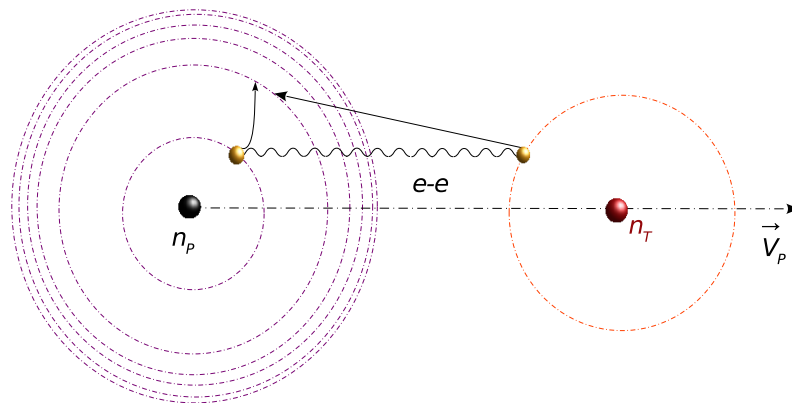


FIGURE 4.1: Schematic representation of RTE process.

Furthermore, RTE only occurs from the ground state, $1s^2\ ^1S$. Indeed the metastable $1s2s\ ^3S$ lies energetically above the respective doubly excited states, so that the latter cannot be populated by RTE.

4.2.2 Non-Resonant Transfer-Excitation

A competitive mechanism to RTE is the Non-resonant Transfer-Excitation (NTE). Here the electron transfer and the excitation are two successive processes and commonly are treated as two single electron independent events. An electron of the target is transferred to an excited state of the projectile due the Coulomb attraction of the projectile nucleus, while projectile electron excitation takes place due to its interaction with the target nucleus (Figure 4.2) [105, 106]. In this process there is no resonance condition, but NTE is usually stronger at lower projectile energies than the RTE maximum [107, 108].

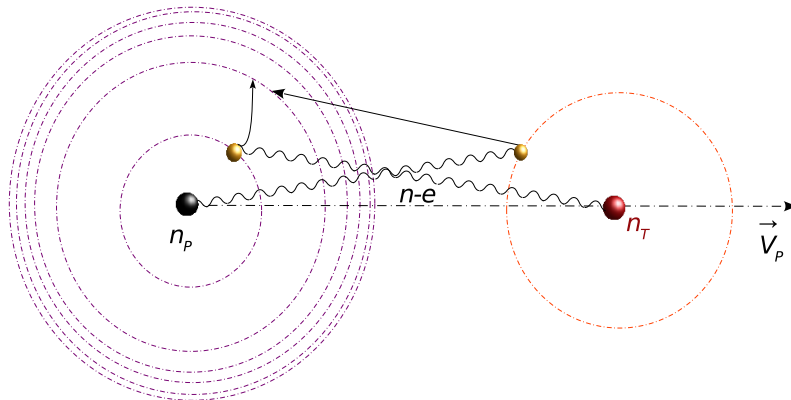


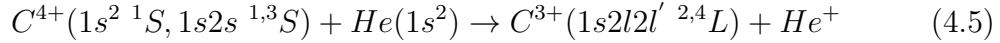
FIGURE 4.2: Schematic representation of NTE process.

Unlikely to RTE, NTE is energetically allowed from both the ground state $1s^2\ ^1S$ and the metastable $1s2s\ ^3S$ metastable state, denoted respectively NTEg and NTEm, respectively [109].

4.3 The C^{4+} - He collision system

In the frame of the present study partially performed with experimentalist collaborators, we have focused on Auger spectroscopy observable states, i.e.

$1s2p^2\ ^2P$, $1s2p^2\ ^2D$, $1s2s2p\ ^2P_{\pm}$, $1s2s2p\ ^4P$ and $1s2s^2\ ^2S$ in



collisions. As can be seen, due to the experimental conditions, different initial states for the projectile have to be taken into account since they are present in the beams, when interacting with the target in the collision chamber. The experimentalists can determine the proportion of the initial states in the beam: $C^{4+}(1s^2\ ^1S)$ contribute to about 75% of the beam and the two other, the metastable ones, to about 25%, following spin statistic proportion between them.

However, among these two pre-excited states, the singlet one represents a very low contribution. Indeed, for C^{3+} , the singlet state $1s2s\ ^1S$ has a life time of $\tau_{1s2s\ ^1S} = 3 \times 10^{-6} s$ whereas the triplet $1s2s\ ^3S$ lives for $\tau_{1s2s\ ^3S} = 2.1 \times 10^{-2} s$ [110]. Therefore, due to the experimental conditions, the singlet state can be considered to have decayed nearly totally when reaching the interaction region, while the triplet not. Consequently, we shall not consider any contribution of the $1s2s\ ^1S$ without any loss of accuracy.

Our experimentalist collaborators have developed a method to extract from the outcomes of their experiment, the cross sections related to either initial states. Therefore, when possible, we shall compare directly our results for a given initial state to their results. When not possible or when comparing to other experimental investigations, we shall weight our results with the contributions of the different initial states, defined approximatively just above.

4.3.1 Calculation details

To obtain probabilities and cross sections of the processes of interest occurring in C^{4+} - He collisions in the considered impact velocity range, i.e., from 0.5 to 18 MeV, we used the SCAOCC method, presented in Chapter 2, but in a three-active-electron development. This allows to have an adequate description of C^{3+} states, but requires to describe the target, approximatively, with a single electron, using a model potential. In the frame of this approximation the active electron of He is bound to He^+ potential, expressed by

$$V_T(r) = -\frac{1}{r} \sum_{i=1}^{13} c_i e^{-\beta_i r^2}, \quad (4.6)$$

with the values of c_i and β_i being given in Table 4.1. This three-active-electron implementation allows for a coupled and coherent treatment of all processes such as SEC, TE, target and projectile excitation, and ionisation.

TABLE 4.1: Coefficients and exponents used to represent the system $He^+ - e^-$ by the model potential eq. 4.6

| | | | | | | | |
|-----------|--------|--------|--------|---------|---------|----------|----------|
| i | 1 | 2 | 3 | 4 | 5 | 6 | |
| c_i | 1.0 | 0.0212 | 0.2386 | 0.2418 | 0.1841 | 0.1220 | |
| β_i | 0.0 | 0.7351 | 4.5960 | 13.3789 | 47.8218 | 260.8236 | |
| i | 7 | 8 | 9 | 10 | 11 | 12 | 13 |
| c_i | 0.1319 | 0.0193 | 0.1065 | 0.1067 | -0.0412 | -0.0779 | -0.0743 |
| β_i | 1.7848 | 0.5064 | 1.0731 | 2.3884 | 12.0949 | 30.8796 | 153.6072 |

Because of this frozen core electron approximation, all presented results have been multiplied by a factor 2 to account for the two target electrons, in an independent particle approximation. The spin-orbit couplings being small were not taken into account.

The extended calculations include 1794 (799 *PPP* and 995 *PTP*) states² and represent thousands of hours of computation. They are based on a set of 7 and 22 GTOs (10 for $l = 0$, $4 \times 3 = 12$ for $l = 1$) for target and projectile respectively, including the magnetic substates M . The full basis set is given in the Appendix A. In Table 4.2, we give the energies of the important C^{3+} , C^{4+} states, compared with the corresponding experimental data from the NIST tables and Chen et al. [111, 112].

TABLE 4.2: Comparison of energies, in a.u., of the C^{3+} and C^{4+} , based on the GTO basis set and the available data [111, 112].

| State | C^{4+} | | | State | C^{3+} | | |
|--------------|-----------|-----------|---------------|------------------|-----------|-----------|---------------|
| | E_{GTO} | E_{Ref} | $\Delta(\%)*$ | | E_{GTO} | E_{Ref} | $\Delta(\%)*$ |
| $1s^2 \ ^1S$ | -32.2187 | -32.4160 | 0.609 | $1s2s^2 \ ^2S$ | -23.9445 | -24.0524* | 0.449 |
| $1s2s \ ^3S$ | -21.3144 | -21.4294 | 0.537 | $1s2s2p \ ^4P$ | -23.8471 | -24.0161 | 0.704 |
| $1s2s \ ^1S$ | -21.1144 | -21.2301 | 0.545 | $1s2s2p \ ^2P_-$ | -23.6284 | -23.7961 | 0.704 |
| | | | | $1s2s2p \ ^2P_+$ | -23.4661 | -23.6361 | 0.719 |
| | | | | $1s2p^2 \ ^2D$ | -23.3580 | -23.5192 | 0.685 |

* $\Delta = |(E_{GTO} - E_{NIST})/E_{NIST}| \times 100$

* Reference [112]

The overall agreement between our basis set asymptotic energies and the available reference data is in general very good and at worst equal to about 0.7% for the considered states.

²Note that *PTP* stands for one electron attached on target and two electron on projectile while *PPP* stands for three electron attached on the projectile.

4.3.2 Results and discussion

In this section, we present the cross sections for the production of the $C^{4+}(1s2l2l')$ electronic configurations in C^{3+} - He collisions. Specifically we shall concentrate on the $1s2s^2\ ^2S$, the two $1s2s2p\ ^2P$ (labelled as $^2P_-$ and $^2P_+$ for the lowest and highest energy levels, respectively, see Table 4.2), the $1s2s2p\ ^4P$, the $1s2p^2\ ^2P$ and $^2D\ C^{3+}$ states. For future comparisons, we additionally present averaged cross sections corresponding to the incoherent addition of the results for the two initial C^{4+} states ($1s^2\ ^1S$, $1s2s\ ^3S$) contributing predominantly (at 75% and 25% respectively, see text above) to the beams in the experimental conditions of our collaborators.

Figure 4.3 shows the cross sections for the production of the $1s2s^2\ ^2S$ state as function of the impact energy. It is shown that the $1s2s^2\ ^1S$ major production mechanism is a direct transfer of a target electron to the $2s$ orbital on the projectile $1s2s$ electronic configuration. For the two corresponding initial levels, cross sections present a parallel dependency with respect to impact energy. However the cross sections for 1S initial state are about two times lower than the one for 3S , this difference being expected by the fact that the first process has a larger exoergicity compared to the latter. On the other hand, the cross sections for the initial C^{4+} ground state are one to two orders of magnitude lower than the previous ones, this ratio increasing for energies below 0.2 MeV/u. Indeed, in this case, the production of $1s2s^2$ corresponds to the bi-electronic process of transfer-excitation, much less likely to its single transfer counterpart from the $1s2s$ configuration. Moreover, this endoergic process corresponds to a Q -value³ of -8.27 a.u. (-225 eV), much larger in absolute value than the one for the metastable initial states (2.63 a.u, i.e. ≈ 71 eV), see Table 4.2. In our results there is no signature of the RTE mechanism (peak expected around 0.5 MeV/u) since the inverse Auger decay is weak. Due to this very large difference between the transfer from $1s2s$ configuration and the transfer-excitation from $1s^2$, the averaged cross sections (solid black line) follow the tendency of the ones from $1s2s\ ^3S$, weighted by about a factor four, due to the contribution of this state in the beam. One can also extract from our data the proportion of $1s2s\ ^1S$, neglected in the present time, beyond which, this approximation is not valid, since for example, a contribution of this latter above 1% will affect the values of the averaged cross sections by about 10%.

The cross sections for the production of $1s2s2p\ ^2P_+$ and $^2P_-$ states, respectively, are shown in Figures 4.4 *a* and *b*. The single transfer process to $2p$ from

³The process energy difference is defined as $Q = E_i - E_f$ between initial and final channels.

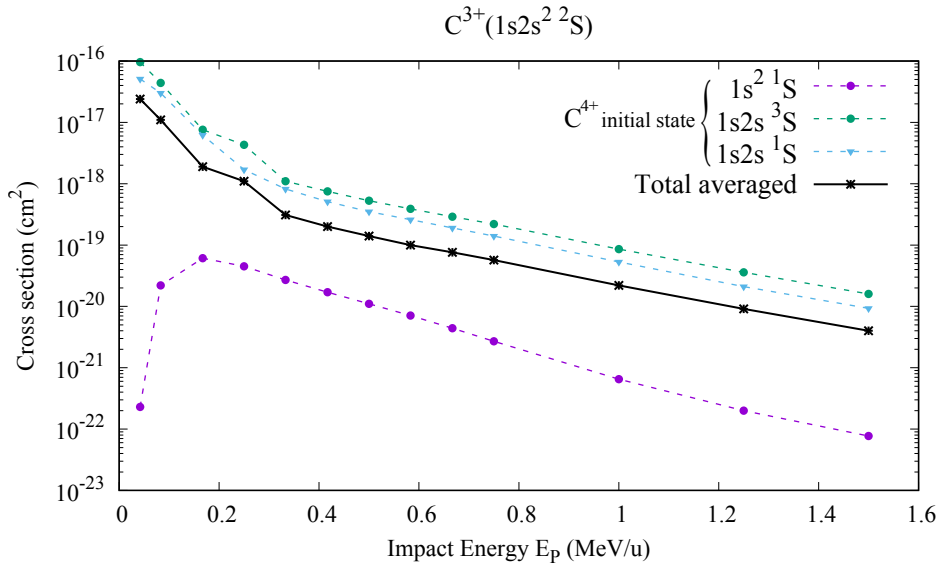


FIGURE 4.3: Cross sections of the production of the $1s2s^2 \ ^2S$ for three initial C^{4+} states. Total averaged cross sections correspond to the combination of the cross sections for 75% and 25% of the $1s^2 \ ^1S$ and $1s2s \ ^3S$ initial states, respectively.

$1s2s$ is dominant and, again, the two-electron transfer-excitation process (from the initial $1s^2 \ ^1S$) is again a minor channel. The same trends are observed as in Figure 4.3, since the Q -values for these channels are close (Table 4.2). For completeness, in Figures 4.4 *c* and *d* we present the cross sections for the magnetic components⁴ of the two final states $^2P_+$ and $^2P_-$. One can observe that the transfer and transfer-excitation processes favour the $M_L = 0$ component of the P states, whatever the initial states. One could expect this tendency since at these high impact energies the processes occur mainly in frontal collisions, that is at low impact parameters b , which weaken the population of the dumbbell-shaped P -component along the x -axis (see Figures 2.1 and 4.6) by symmetry (totally cancelled for $b = 0$). However one can observe a different behaviour for the transfer-excitation to the $^2P_-$ with a dominant population of the $M_L = 0$ component only for the lowest energies considered ($E < 0.4$ MeV/u).

In Figure 4.5 we present the cross sections for the production of the $1s2s2p \ ^4P$ state as function of the impact energy. Our calculations, in which we have included all Coulomb interactions but not spin-orbit couplings, conserve total spin. The quartet states can then be produced only from the metastable $1s2s \ ^3S$ C^{4+} states. The production of the quartet states from the ground

⁴The cross sections labelled $|M_L|$ ($M_L \neq 0$) means the sum of the cross section for M_L and $-M_L$ equivalently, since equal, the cross sections of M_L multiplied by 2, i.e. $\sigma(|M_L|) = \sigma(M_L) + \sigma(-M_L) = 2\sigma(M_L)$.

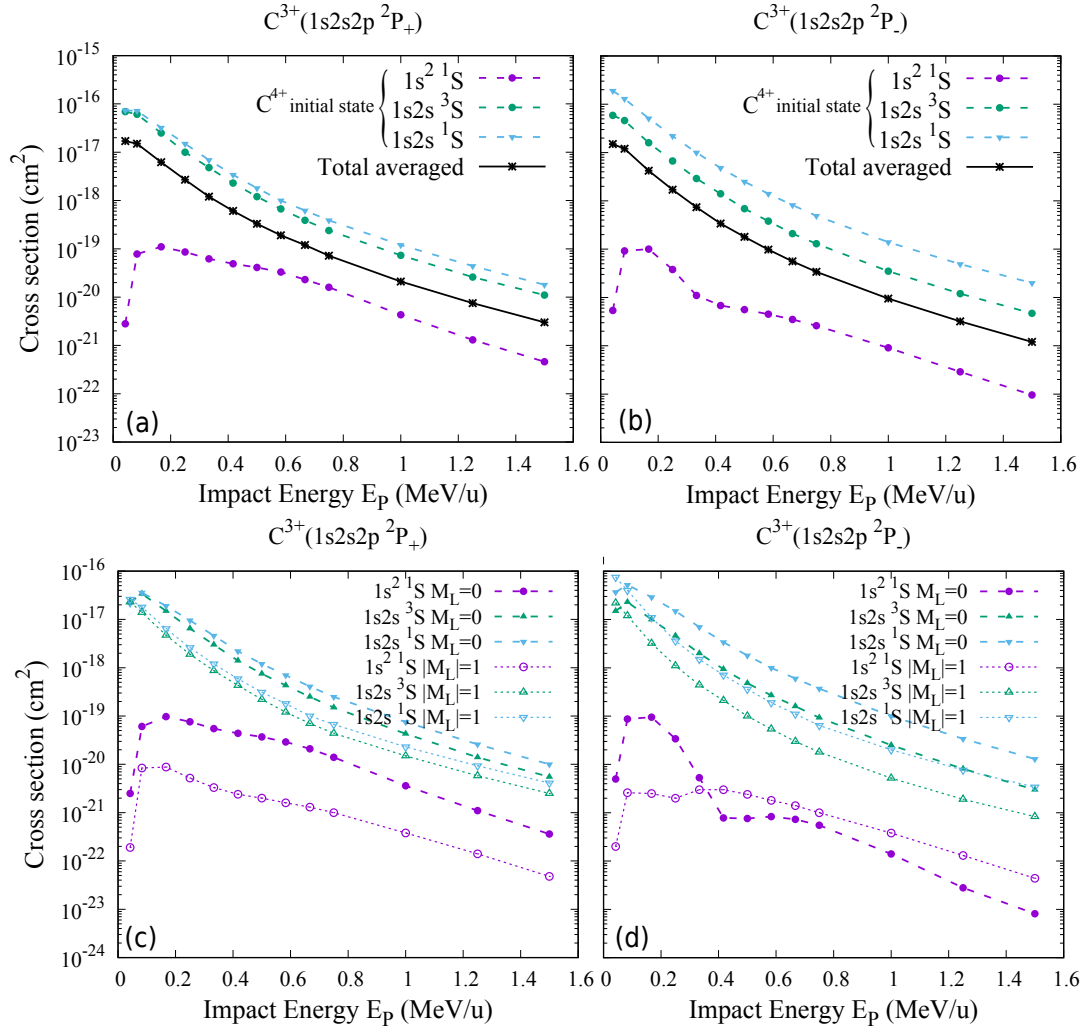


FIGURE 4.4: Cross sections for the production of the $1s2s2p^2P_+$ (left panels) and $^2P_-$ (right panels) for the three projectile initial states. The two upper panels show the total cross sections while the two lower panels the cross sections of the M-components of the $1s2s2p^2P_{\pm}$ states. In the upper panels, the solid lines show an averaged cs , using 75% and the 25% for $1s^2\ ^1S$ and $1s2s\ ^3S$, respectively.

and metastable singlet states requires a spin flip, a mechanism not present in our treatment. However, when considering the ground state initial state, the inverse Auger process model [113] suggests that this production would be five orders magnitude smaller than what it is observed from the $1s2s\ ^3S$, supporting our treatment. The cross sections shown in Figure 4.5 present similar values and behaviour as a function of energy as their doublet counterpart. Again it is observed that the population of the $M_L = 0$ component is the dominant channel.

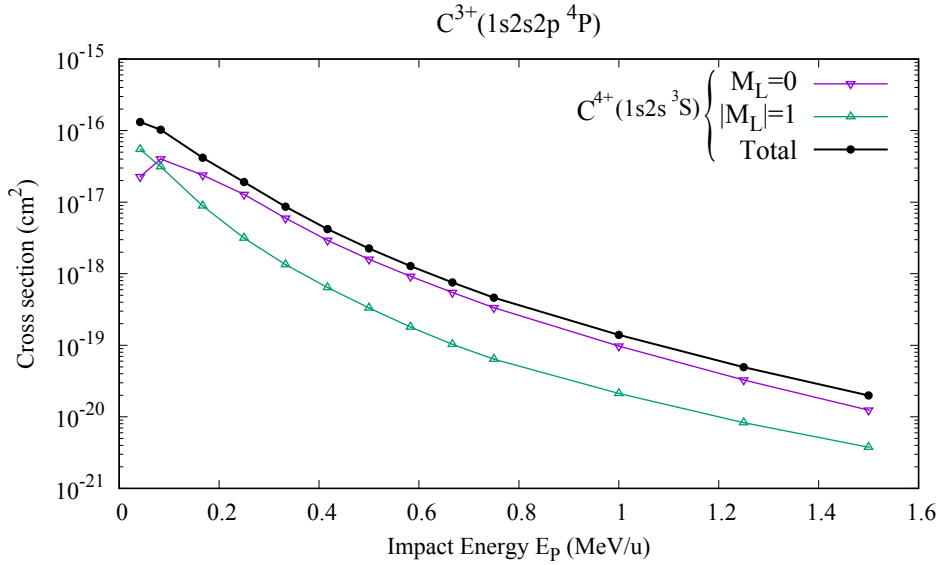


FIGURE 4.5: The quartet state $1s2s2p\ ^4P$ production by capture from the $C^{4+}(1s2s\ ^3S)$ initial states.

Additionally it is interesting to analyse the differential (semi-classical) quantities that are the probabilities to get further insight in the study of the capture process. The impact parameter b dependence of reduced probability $bP(b)$ for the production of the $1s2s^2\ ^2S$, $1s2s2p\ 2P_{\pm}$, and $1s2s2p\ ^4P$ states is presented in Figure 4.6 for the $C^{4+}(1s2s\ ^3S)$ initial state⁵. Note the logarithmic scale used on the ordinate axis. The three different P states show similar behaviour for the 12 impact energies considered. The impact parameter-weighted probability follows a bell-shape behaviour with an increase up to b ranging between about 0.5 and 1.0 a.u., depending on the impact energy, followed by an exponential decay. For the three P states the maximum of $bP(b)$ shifts to smaller impact parameters with increasing projectile energy, as expected. The maximum for $E = 2$ MeV is located at around $b = 1$ a.u., while for the highest energy, $E = 18$ MeV, it is found around $b = 0.5$ a.u. This indicates that the values of the cross sections shown previously, stem mainly from trajectories characterised by internuclear distances, smaller than about 2 a.u., i.e. quasi frontal collisions.

However, the $1s2s^2\ ^2S$ state probabilities present a different behaviour, with a special feature, not observed for the P states. The reduced probabilities curves show two maxima, separated by a minimum which shifts to higher b with increasing impact energies. For the lowest energies, the second maximum which represents the main contribution to the total cross sections can be explained

⁵The probabilities are not multiplied by the factor of 2 to account for the second electron: the cross sections shown previously correspond to the integration of these curves, further multiplied by $2\pi \times 2$ (see eq. 2.42).

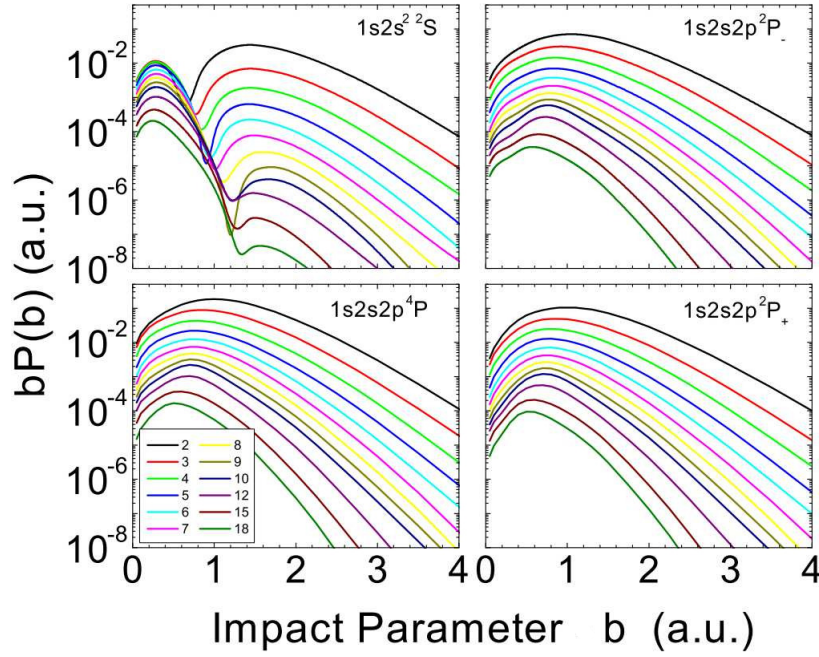


FIGURE 4.6: The impact parameter-weighted probability $bP(b)$ impact parameter dependence for the production of the $1s2s^2\ ^2S$, $1s2s2p\ ^2P_{\pm}$ and the $1s2s2p\ ^4P$ states in $C^{4+}(1s2s\ ^3S)$ - He collisions. Colour code: Projectile energy E_P in MeV. On the contrary to the cross sections in this chapter, the present probabilities are not multiplied by the factor 2 to account for the second target electron.

by the transfer of a spin-down electron from the target to the $2s$ orbital onto the initial spin-up $1s2s\ ^3S$ state. This orbital has a larger extent than the $1s$ orbital and thus can be populated during more distant collisions. On the other hand, regarding the production of the $1s2s2p\ ^2P$ states, this restriction is removed and the spin-down electron can be transferred to any of the three orbitals, explaining the rather smooth behaviour of the probabilities in this case. However, the first maximum at $b \approx 0.5$ a.u. denotes that for increasing velocities for which its contribution becomes more dominant in the cross sections, 2S production stems from more and more head-on collisions and its population can take place through exchange couplings, present in our treatment. This mechanism is for sure present for the two $1s2s2p\ ^2P$ states but does not give rise to the characteristic structures observed for 2S . Nevertheless, the second maximum can still be observed, but is more than one order of magnitude less important than the first, so that it can be only considered as very weakly contributing to the cross sections.

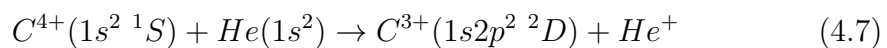
In C^{4+} - He system, the state of most interest for transfer-excitation study is

the $1s2p^2\ ^2D$, with a presence of a clear signature of resonant transfer-excitation (RTE) mechanism observed in previous studies [114] and also for other projectiles, such as F^{7+} [115], described in the next section. This feature is related to the strong Auger rate of this state, as a direct image of the inverse Auger effect advocated for this mechanism. We should note, compared to these previous investigations, that the present work corresponds to the first non perturbative treatment of such processes within a full configuration interaction approach [116] for three active electrons. Moreover, our calculations are performed in a wide range of impact energies, from 0.1 to 1.5 MeV/u, covering the region where, in addition to RTE, the so called non-resonant transfer mechanism can be observed. It is the first time that such a study is carried out, using a unique, quasi ab initio, theoretical treatment.

Figure 4.7 shows the cross sections for production of $1s2p^2\ ^2D$ for the three initial projectile states considered so far. One can observe the dominance of transfer-excitation to the ground state for impact energies higher than approximately 0.4 MeV/u, while for lower energies it gets gradually less likely and transfer-excitation processes to the metastable states dominate. These latter follow a very similar behaviour all over the energy range considered, with a light preference for the $1s2s\ ^3S$ initial state. These two regimes can be explained by the energy difference between initial and final channels. Indeed, as previously mentioned (see also Table 4.2) the ground state lays about 250 eV below the 2D so that transfer-excitation becomes unlikely for decreasing energies. On the other hand the $1s2s\ ^3S$ is about 55 eV above the 2D whose energy is raised by the Coulomb repulsion term between the two collision partners (C^{3+} - He^+), as their internuclear distance decreases during the scattering event. This molecular effect lowers the energy gap between the initial and final channels and makes the process increasingly more likely for decreasing energies.

Again we also present in solid line in Figure 4.7 the cross sections averaged on the two main C^{4+} initial states, $1s^2\ ^1S$ (75%) and $1s2s\ ^3S$ (25%), co-existing in the standard experimental conditions encountered with accelerators. One can observe that these averaged cross sections show the outcomes of two different processes, depending on the impact energy. Note that a not precise knowledge of the respective weights of $1s^2$ and $1s2s\ ^3S$ in experimental investigations may disturb significantly a comparison with theoretical results.

Focusing now on the production of the 2D from the ground state,



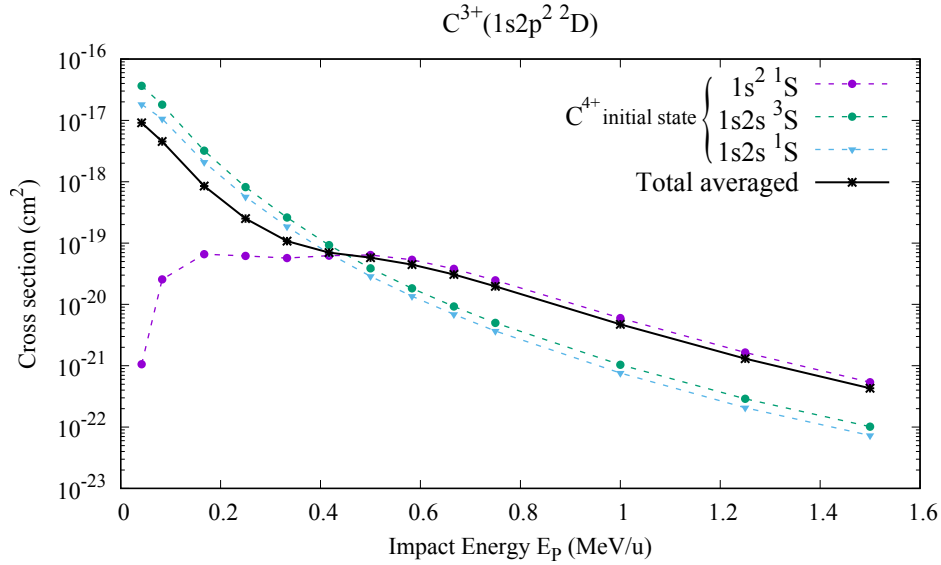
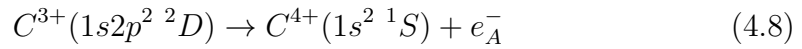


FIGURE 4.7: Cross sections for the production of the $1s2p^2 \ ^2D$ state as function of energy for the three initial C^{4+} states. Total averaged cross sections correspond to the combination of the cross sections for 75% and 25% of the $1s^2 \ ^1S$ and $1s2s \ ^3S$ initial states, respectively.



one can see that the energy dependence of the cross sections is rather different from the ones observed so far in this chapter. It seems that there is a plateau between 0.2 and 0.6 MeV/u which corresponds in fact to two maxima. They are hardly observable with the chosen logarithmic scale but, presented in linear (purple line in the left panel of Figure 4.8), they are clearly observed at about 2 MeV (≈ 0.17 MeV/u) and 6 MeV (0.5 MeV/u). In this figure, we present also the reduced probability (in linear and logarithm scales in left and right panels) of production of 2D as function of impact parameter and for several impact energies.

Let us remind that, in general, small b are known to correlate to large projectile deflections, characteristic of more violent collisions, mainly driven by electron-nucleus ($e-n$) interactions, giving rise to electron transfer, for example. Alternatively, large b typically correlate with small deflections characteristic of more gentle electron-electron ($e-e$) interactions, as excitation [117] or loss [118, 119]. In Figure 4.8 it is observed that for energies between 1-3 MeV the reduced probabilities $bP(b)$ are limited to low impact parameters ($b \approx 1$) whilst regarding the high energy peak around 6 MeV/u (0.5 MeV/u) they extend up to $b \approx 2 - 3$ a.u. This finding is coherent with the inverse Auger effect, signature of electron-electron interactions and the so called RTE peak. We shall return to

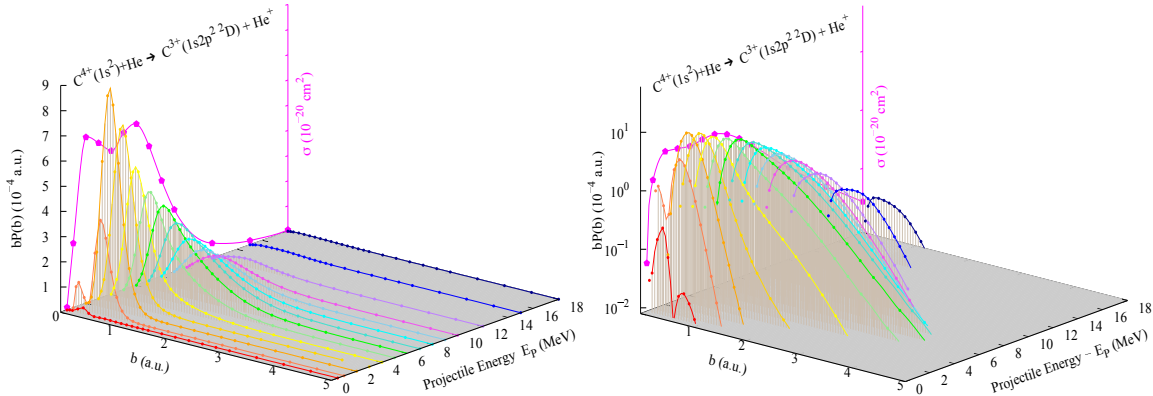


FIGURE 4.8: Left (linear scales): $1s2p^2 \ ^2D$ production from $1s^2 \ ^1S$ in purple line. The corresponding impact parameter-weighted probabilities $bP(b)$ (rainbow lines) for each energy. Right: same as left in logarithmic scales.

the impact parameter dependence later on this chapter trying to study further these two peaks.

Furthermore it is interesting to explore the partial cross sections of the $1s2p^2 \ ^2D$ production. Figure 4.9 depicts the cross sections of each magnetic component of 2D for the ground initial state $1s^2 \ ^1S$. For simplicity, we do not present any $1s2s \ ^1,3S$ contribution since it does not contribute in the cross sections measured experimentally. In Figure 4.9 one can observe that the $M_L = 0$ component is largely dominant at high energy when considering the initial ground state, with the relative weight of the $|M_L| = 1$ components increasing for decreasing energy, the $|M_L| = 2$ being totally negligible in the range considered. In particular the high energy peak of 2D , related to RTE, stems mainly from the $M_L = 0$ magnetic substate. This is consistent to our up-to-date knowledge since in the RTE mechanism, the exchange of angular momentum occurs exclusively between two interacting electrons and the transferred electron carries no net angular momentum into the collision [120]. On the other hand, for the low energy peak (violent collisions), this is not the case since interaction with the target nucleus is involved, affecting more significantly the three magnetic substates of 2D [121].

A comparison of the present theoretical approach with the experimental results of our collaborators is presented in Figure 4.10. These single differential cross sections (SDCS), labelled $d\sigma_A(E_p)/d\Omega'$ in the figure, were measured during a recent experimental campaign performed at the NCSR "Demokritos" 5.5 MV Tandem accelerator facility [122], using their zero-degree Auger projectile spectroscopy setup. Details on the experimental investigation can be found in [123]

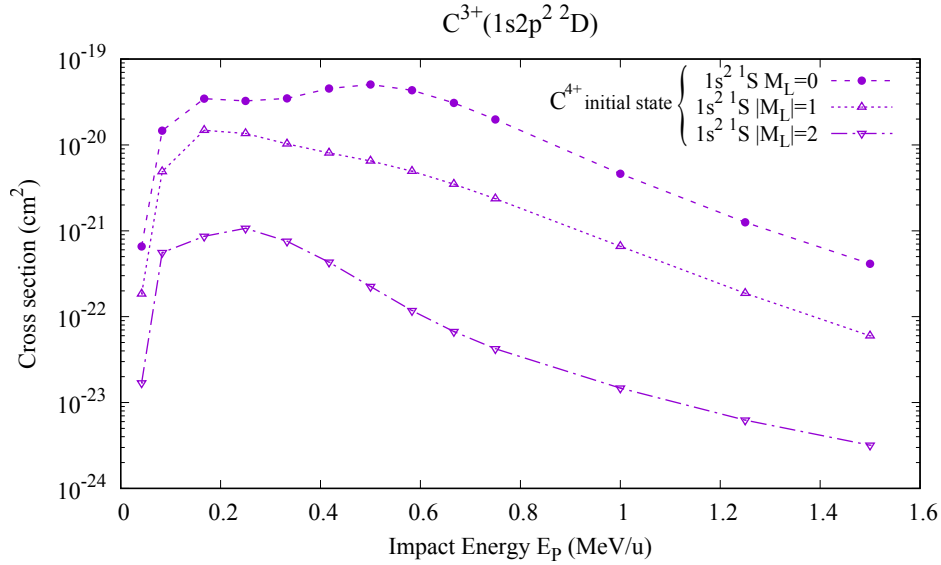


FIGURE 4.9: The energy dependence of $C^{3+}(1s2p^2 2D)$ M_L -resolved cross sections for the $1s^2 1S$ projectile initial state.

and in [124] for the two-spectra measurement technique that they developed to extract from the measured signal the contributions of the $1s^2 1S$ ground and $1s2s 3S$ metastable states. To compare with these data, our results presented in Figure 4.10 are

$$\frac{d\sigma_A(0^\circ)}{d\Omega'} = \xi \frac{5}{4\pi} \sigma(M_L = 0) \quad (4.9)$$

where $\xi \simeq 1$ is the Auger yield of the $2D$ state, and $\sigma(M_L = 0)$ is the $M_L = 0$ component of our calculated cross sections presented in Figure 4.9. It is also included the theoretical results from the traditional Impulse Approximation (IA) RTE [125] model which is found to be about 30% larger than our calculations and the measurements, a known deficiency for light projectile ions [92]. The Impulse Approximation is a simple model mostly valid when the collision time is much shorter than the typical ("orbiting") time of the active target in the target, i.e. when $V_P \gg v_e$ and therefore when the electron can be considered free. Then this approach to model the resonant transfer-excitation mechanism is based on the (inverse) Auger effect formalism, and improved by using the momentum distribution of the target electron, instead of a mono-kinetic electron. It has been very popular among the studies on RTE during the past decades when sophisticated approaches and calculations were not available, until the present work.

As mentioned above, one can observe clearly in this figure that our results

show two distinct peaks. The high energy peak is seen to be in excellent agreement with the measurements in both the energy dependence and the absolute scale. Its maximum is located at 6 MeV (0.5 MeV/u), as the peak predicted in the RTE IA model. This is the first coupled channel confirmation of the inverse Auger (RTE) mechanism, but with quantitative agreement and a domain of validity larger, especially at low energies. On the other hand, the low energy peak located at 2 MeV (≈ 0.17 MeV/u), traditionally attributed to the non-resonant transfer-excitation mechanism, was not recorded experimentally by our collaborators since the C^{4+} beam delivered at the "Demokritos's" accelerator was not enough intense below 4 MeV (0.3 MeV/u) energies.

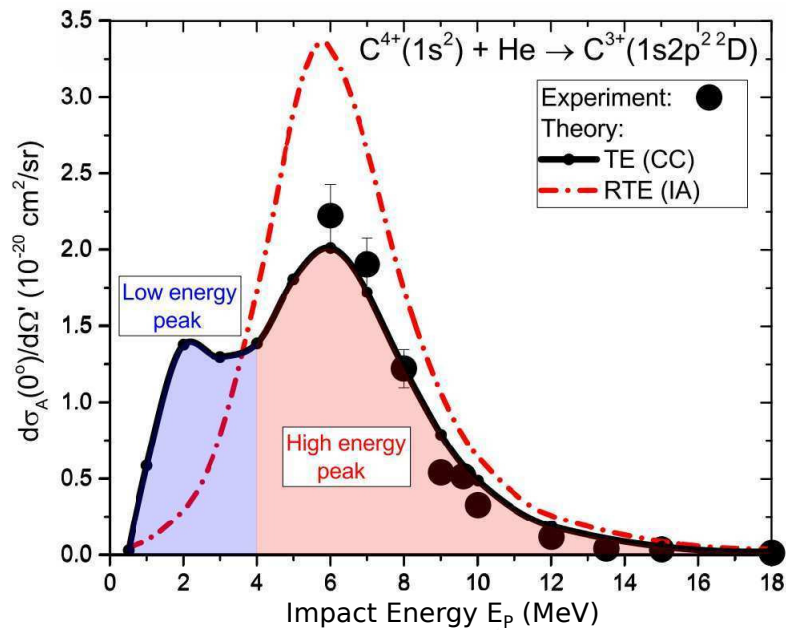


FIGURE 4.10: 0° Auger SDCS, $d\sigma_A(E_p)/d\Omega'$, for the production of 2D state. Experiment: black circles. Present results: small circles joined by black interpolation line. Conventional RTE IA (red chain line). The low (blue) and the high (red) energy peak regions are delineated.

To get further comprehension of the electronic dynamics, we performed calculations using the same close-coupling approach but with a restricted basis set including only two energy levels (the results will be labelled as 2-level CC in the following) as initially proposed by our collaborator, Prof. T. Zouros: compared to the extended (1794 states) close-coupling calculations (CC), the restricted ones use a basis set composed of only the initial states of the collision partners, i.e. the target and projectile ground states, and the final level

$C^{3+}(1s2p^2\ ^2D)$, with its five magnetic states. As in the CC calculations presented previously, they include notably the electron-electron repulsion couplings between the states. This model suppresses on purpose any two-step mechanism by removing any single capture and single excitation states, thus allowing only a simultaneous transfer and excitation processes. This can be considered equivalent to the RTE assessment model used by Fritsch and Lin [98] in their study of TE for $He^+ - H$ collisions.

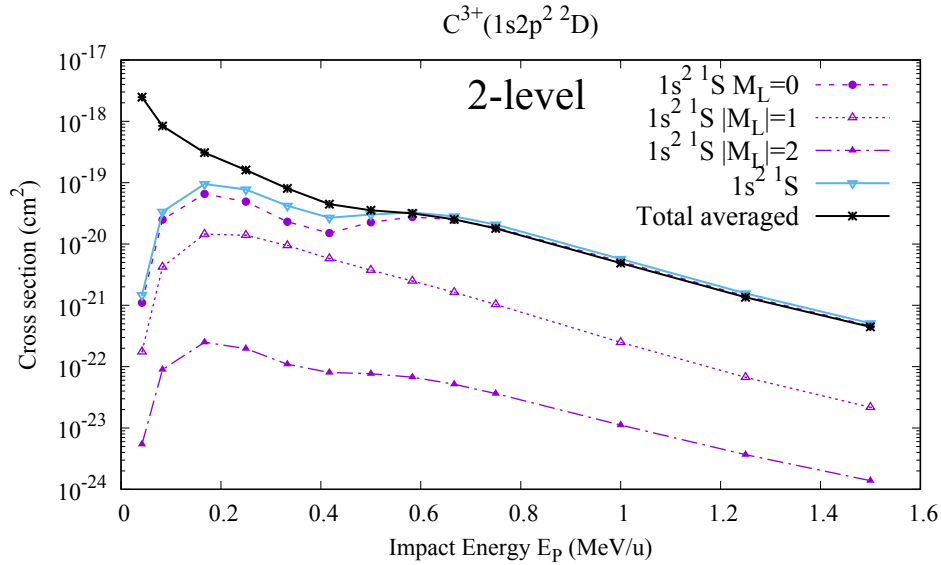


FIGURE 4.11: 2-level CC calculations: cross sections of production of the $1s2p^2\ ^2D$ states in $C^{4+}(1s^2\ ^1S) - He$ collisions: total averaged cross section (solid black line), total (solid light blue line) and magnetic components (dashed purple lines).

Figure 4.11 shows the results from this 2-level model. They can be compared to the results shown in Figure 4.7 and 4.9 which correspond to the calculations using the full basis set. One can see that these new cross sections show the same tendency as function of impact energy than the previous. The two peaks are again present, with a slight shift toward high energies for the second one. However the two series of calculations show some quantitative differences: the first peak presents a stronger maximum, at 10^{-19} cm^2 about 40% higher than the first peak in Figure 4.7, unlike the second one which is lower. When analysing the cross sections for the different M_L components, one observes again results in agreement with the results from the extended calculations: the $M_L=0$ cross section dominates, even more strongly, the other components in the complete energy range, the differences with the $|M_L|=1$ getting smaller, again, for low energies. One can draw two conclusions from this general comparison: the two-level CC calculations, which represent in a certain manner a perturbative,

minimal, representation of the process, carries the core physics which explains the transfer-excitation. However even though we are considering a high energy domain (1 MeV/u, i.e. $v_P \approx 6.2$ a.u.) this few-state model does not converge quantitatively with the many-state calculations, showing the importance of other states and of couplings between them in the production of the 2D .

In Figure 4.12 we show and comment further these two series of results (labelled "CC" and "2-level CC"), together with results obtained with a complementary, more restricted, model (labeled "2-level CC, without TCee"). The idea of this new model is to keep minimum the number of states, i.e. the initial and final channels, which have been proved to describe qualitatively the process, and perform the same calculations, but neglecting all two centre electron-electron repulsion couplings (named TCee in the caption). These latter are the bi-electronic matrix elements which couple a target electron (in a $1s$ orbital centred on He) to a projectile electron (in $2p$ or $1s$ orbital centred on C^{3+}). The electron-electron interaction is responsible, indeed, for the production of this doubly excited state and neglecting these coupling terms in our calculations forbids therefore the RTE mechanism, i.e. an inverse Auger effect, advocated to interpret the high energy peak.

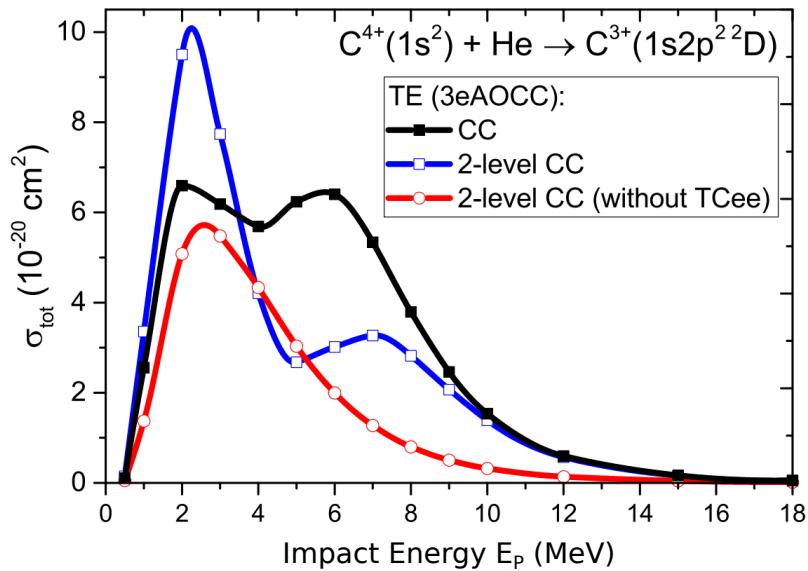


FIGURE 4.12: Cross sections for the production of the $1s2p^2 {}^2D$ states as function of impact energy. Full calculations (filled black squares), 2-level restricted calculations (open blue squares), 2-level restricted calculations, neglecting TCee (open red circles).

In Figure 4.12 we see again the agreement between the full and the 2-level

calculations, concerning the existence of the two peaks. However the cross sections from the 2-level calculations neglecting TCee present again the first peak at about the same energy but decrease monotonously for increasing energies. The absence of the high energy peak in this model demonstrates in a very convincing way the crucial role of the electron-electron interactions in the process of transfer-excitation around 6 MeV (0.5 MeV/u) energy, i.e. the resonance region predicted by the inverse Auger effect model. It is quite original to get such a probe of this RTE mechanism, using different close-coupling models, together with a near exact treatment (CC) which show very good agreement with experimental data.

We next consider the low energy peak at around 2 MeV (0.16 MeV/u), which is traditionally interpreted as a two successive steps mechanism involving electron-nucleus interactions [98, 105], the so called NTE mechanism, as previously described in this thesis. The results from the two restricted close-coupling calculations are quite illuminating for the interpretation of this peak. Indeed these two models do not include any intermediate states, i.e. pure capture states (e.g. $C^{3+}(1s^2 2p) - He^+$) and projectile excited states (e.g. $C^{4+}(1s 2p) - He$), so that the two-step mechanism is formally not described. However they both show the low energy peak, ruling out the two-step interpretation. The existence of the low energy is therefore related to a one-step correlated mechanism where both excitation and transfer are induced simultaneously, by electron-nucleus and electron-electron interactions.

A further probe of these conclusions is provided by the analysis of the differential, more fundamental, quantities that are the reduced probabilities as function of impact parameter. Figure 4.13 shows them for the three models advocated in this chapter (the left panel shows the full CC calculations and corresponds, in linear scale, to the results of Figure 4.8). The comparison of the three panels is quite striking: i) the maximum at small b is present in all the 3 panels for the three lowest energies. It is the signature of frontal collisions, involving strong electron-nucleus interactions but also an important overlap of the target and projectile electronic clouds and therefore significant electron-electron repulsion and an exchange of a target electron to the projectile ions, ii) the probabilities from the two calculations which include the two-center electron-electron couplings show a tail (or maximum) for larger impact parameters, the "2-level without TCee" results do not, which explains the absence of high energy peak for the cross sections stemming from this model. Coherently to what was discussed previously in the thesis it results that the "gentle" collision zone where the electron-electron interaction is important contributes to

the presence of the high energy resonant peak.

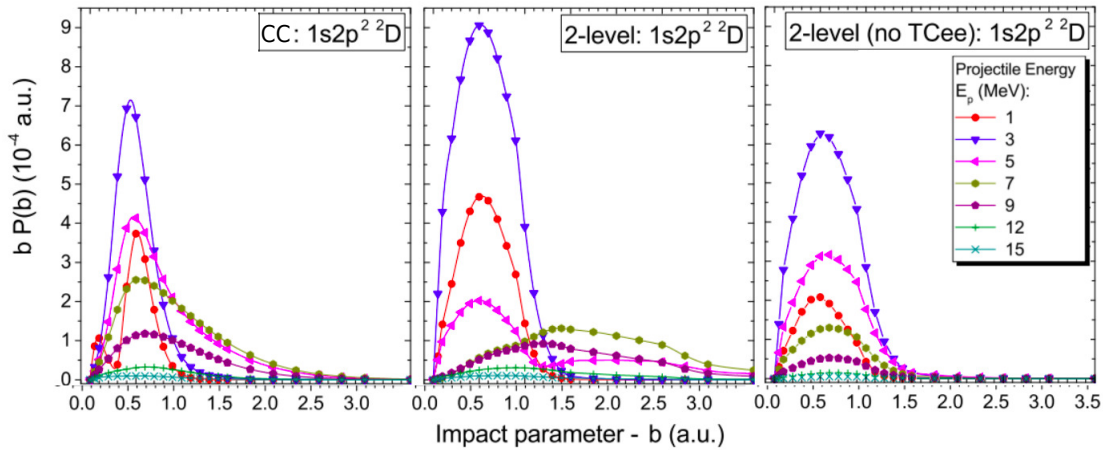
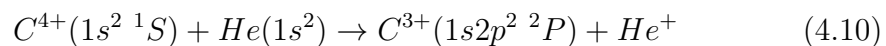


FIGURE 4.13: Impact parameter-weighted probabilities $bP(b)$ for the TE production of the $1s2p^2 \ ^2D$ state as a function of b at selected projectile energies E_P . Left panel: full close coupling calculations; Middle panel: 2-level restricted calculations; Right panel: 2-level restricted calculations neglecting TCee.

In the final part of this section, we show for comparison the cross sections for the production of the 2P states which correspond to the same electronic configuration ($1s2p^2$) as the 2D level. In Figure 4.14 the cross sections for production of $C^{3+}(1s2p^2 \ ^2P)$ are shown as function of impact energy, for the three projectile initial states considered. They can be compared to the ones for 2D production (Figure 4.7) : due to the small energy difference between these two levels, their dependence with respect of energy are quite similar, with, again, a weak transfer-excitation process from the ground state at low energies.

However the production of 2P is predicted to be about one order weaker than the one of 2D , except from the $1s2s \ ^1S$ state for which the cross sections are close and correspond to the strongest process in the whole energy range considered. For the ground state, the transfer-excitation is indeed much weaker but the cross sections present two peaks, as in the case of 2D , but located at lower energies, 0.1 and 0.3 MeV/u respectively. In Figure 4.15, as we did for a 2D level, we now concentrate on this specific channel, i.e.



and show the same cross sections in linear scale, together with the cross sections obtained by the 2-level (i.e. 1+3=4 states) model. The latter do show a unique peak, at about 0.25 MeV/u, as the full close-coupling calculations. This does not match the resonance condition predicted by the RTE mechanism: it should be

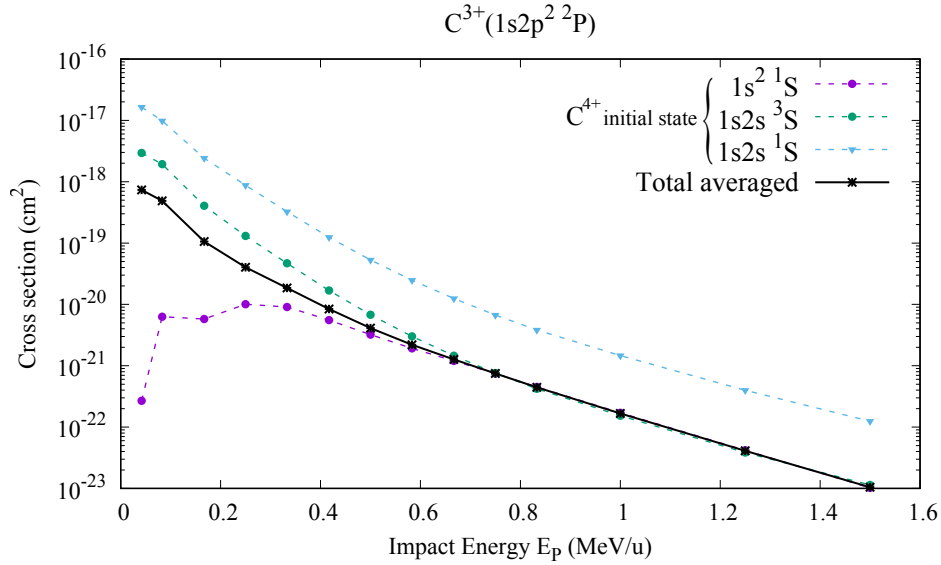


FIGURE 4.14: Cross sections for the production of the $1s2p^2\ ^2P$ state as function of energy for the three initial C^{4+} states of the projectile. Total averaged cross sections correspond to the combination of the cross sections for 75% and 25% of the $1s^2\ ^1S$ and $1s2s\ ^3S$ initial states, respectively.

at about the same energy as for 2D , i.e. 0.5 MeV/u, since these two levels have nearly same binding energy, with a difference smaller than 1 eV. The absence of the RTE peak is consistent with the inverse Auger process picture since the Auger yield is negligible compared to the 2D one.

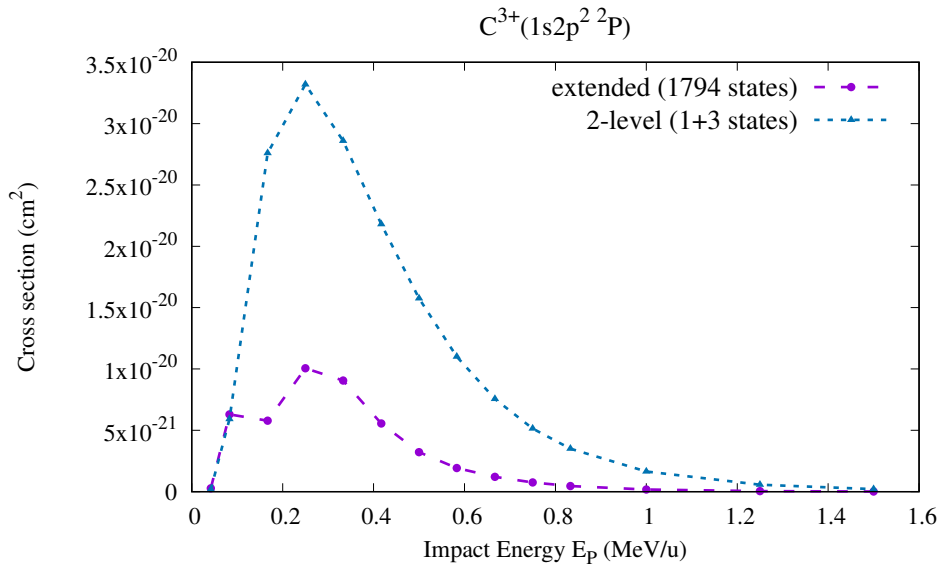


FIGURE 4.15: Cross sections of production of the $1s2p^2\ ^2P$ states, using the full close-coupling and the 2-level calculations.

This is supported by the analysis of the reduced probabilities as function of impact parameter. Figure 4.16 presents these quantities for the full calculations, as well as the "2-level" and "2-level without TCee" models. Though the panels show quantitative differences between the models, the two first ones do not show probabilities extending to large impact parameters, as for 2D , representative of important electron-electron coupling. They rather show a peaked probability distribution, dying out after 1-1.5 a.u. This structure, equivalent to the one observed for the 2D states, corresponds to the peak observed at about 0.3 MeV/u in the cross section dependences and is therefore related to the same mechanism of simultaneous, correlated, transfer-excitation advocated for 2D . Finally let us note that the peak observed in the cross sections at 0.1 MeV/u (or rather the minimum observed at about 0.2 MeV/u), with no equivalence for the 2D case, has not been analysed further but maybe related to couplings with 2S states present only in the full close-coupling calculations.

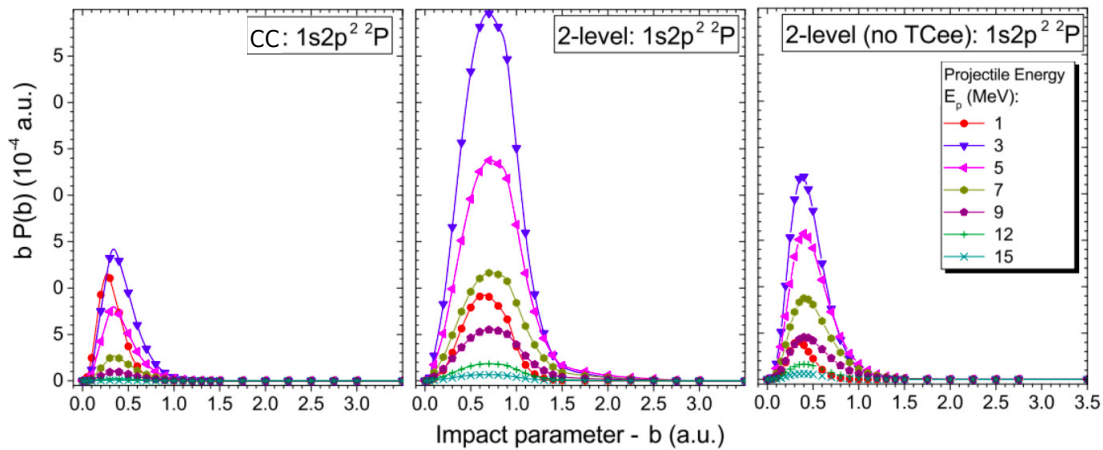
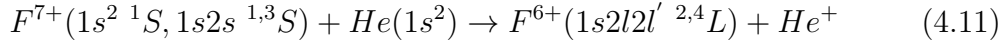


FIGURE 4.16: Impact parameter-weighted probabilities $bP(b)$ for the TE production of the $1s2p^2 {}^2P$ state as a function of b at selected projectile energies E_P . Left panel: full close coupling calculations; Middle panel: 2-level restricted calculations; Right panel: 2-level restricted calculations neglecting TCee.

4.4 The F^{7+} - He collision system

For comparison and to generalise our theoretical investigation, we study now the heavier F^{7+} - He collision system. Indeed over the last few decades, experimental works using Auger electron spectroscopy have been performed for this system, to study transfer-excitation and test the RTE mechanism interpretation [109, 115, 126]. In this context, we focus on the same Auger spectroscopy observable

states as for C^{4+} , i.e. $1s2s^2\ ^2S$, $1s2s2p\ ^2P_{\pm}$ and 4P and $1s2p^2\ ^2D$ in the



In the experimental study of this system [109, 115], the authors were not able to extract quantitatively the contribution of the different C^{4+} states present in the beam. We can therefore only compare with their results at the level of the averaged cross sections, using the few information written in the two papers: we use typical proportions of 70%, 25% and 5% for the three components, $1s^2\ ^1S$, $1s2s\ ^3S$ (whose lifetime is $\tau = 277\mu s$) and $1s2s\ ^1S$ ($\tau = 0.2\mu s$), respectively.

4.4.1 Calculation details

As for the carbon-helium system, to obtain probabilities and cross sections of interest in F^{7+} - He collisions at impact energies ranging from 0.25 to 1.9 MeV/u, we use the 3-active-electron SCAOCC method, presented in Chapter 2. We used the electronic Hamiltonian H^{el} , (eq. 2.16), with the same model potential V_T for He (see eq. 4.6 and Table 4.1). Thus, all presented results have been again multiplied by a factor 2 to account for the two target electrons, in the independent particle approximation.

For this system we use the same set of Gaussian type orbitals as for C^{4+} - He collisions, using only the Gaussian Z_P^2 scaling rule for the projectile GTOs, i.e. with exponents multiplied by a $(9/6)^2$ factor. Based therefore on a set of 7 and 22 GTOs (10 for $l = 0$, $4 \times 3 = 12$ for $l = 1$) on target and projectile respectively, the extended calculations include 1608 (808 *PTP* and 800 *PPP*) states and represent several thousands of hours of computation. The full basis set is given in the Appendix A and, in Table 4.3, we give the energies of the important F^{6+} and F^{7+} states. They are compared with the corresponding available data from the NIST tables [73] and Refs [115, 127].

The overall agreement between our basis set asymptotic energies and the available theoretical and experimental data is very good for the states of interest, at worst equal to about $\approx 0.3\%$ for the $1s2s2p\ ^4P$ states.

To solve the coupled differential equations (eq. 2.34), we use a larger collision zone compared to the carbon system since the projectile charge is larger and can induce couplings at larger internuclear distances. We extended the collision zone from 200 a.u. (from -100 to 100 a.u.) to 400 a.u. (from -200 to 200 a.u.) and increased the number of projectile positions (mesh points) from 100 to 300, for which the matrix elements are computed. Figure 4.17 shows the convergence of the cross sections calculated using three different zone density associations:

TABLE 4.3: Comparison of energies, in a.u., of F^{6+} and F^{7+} states, based on the GTO basis set and the NIST data [73] and Refs [115, 127]

| State | F^{7+} | | | State | F^{6+} | | |
|--------------|-----------|-----------|---------------|------------------|-----------|-----------|---------------|
| | E_{GTO} | E_{Ref} | $\Delta(\%)*$ | | E_{GTO} | E_{Ref} | $\Delta(\%)*$ |
| $1s^2 \ ^1S$ | -75.4472 | -75.5939 | 0.194 | $1s2s^2 \ ^2S$ | -56.1623 | -55.2674 | 0.231 |
| $1s2s \ ^3S$ | -48.9367 | -48.6974 | 0.188 | $1s2s2p \ ^4P$ | -56.0164 | 56.1999 | 0.325 |
| $1s2s \ ^1S$ | -48.6058 | -49.0303 | 0.191 | $1s2s2p \ ^2P_-$ | -55.6259 | -55.7378 | 0.201 |
| | | | | $1s2s2p \ ^2P_+$ | -55.3951 | -55.5430 | 0.266 |
| | | | | $1s2p^2 \ ^2D$ | -55.1991 | -55.3409 | 0.256 |

$$* \Delta = |(E_{GTO} - E_{Ref})/E_{Ref}| \times 100$$

in the caption, for example “-200 200 300” means a collision zone extending from -200 to 200 a.u., with 300 mesh points. We show this comparison for five different F^{6+} channels for two F^{7+} initial states, $1s^2 \ ^1S$ (panel a) and $1s2s \ ^3S$ (panel b).

It can be seen that the convergence between the three different calculations is excellent for the low impact energies. On the contrary, for high impact velocities, disagreements exist, up to about 20%. The results presented in the following stem from calculations using the larger zone and number of mesh points, i.e. “-200 200 300” (B) parameters.

4.4.2 Results and discussion

In Figure 4.18 we present as function of impact energy, zero angle singly differential cross sections (SDCS)

$$\frac{d\sigma_A(0^\circ)}{d\Omega'} = \xi \frac{2L+1}{4\pi} \sigma(M_L=0) \quad (4.12)$$

(with $L = 0, 1$ and 2 for S, P and D levels) extracted from our calculations, in comparison with the experimental results reported in [109, 115]. They are shown for the $1s2p^2 \ ^2D$ (panel a), $1s2s2p \ ^2P_+$ (panel b), $1s2s2p \ ^2P_-$ (panel c) and $1s2s^2 \ ^2S$ (panel d) and correspond to the cross sections averaged over the assumed contributions of the three F^{7+} states present in the beam (70%, 25%, 5%, see text above). We are aware that although these ratios are realistic, the comparison may be biased by these assumptions and by the fact we used the same ones, independently of the impact energy. However the comparison is reasonable even though the decrease of the experimental cross sections for increasing energies is faster than ours. Remembering the state-to-state cross

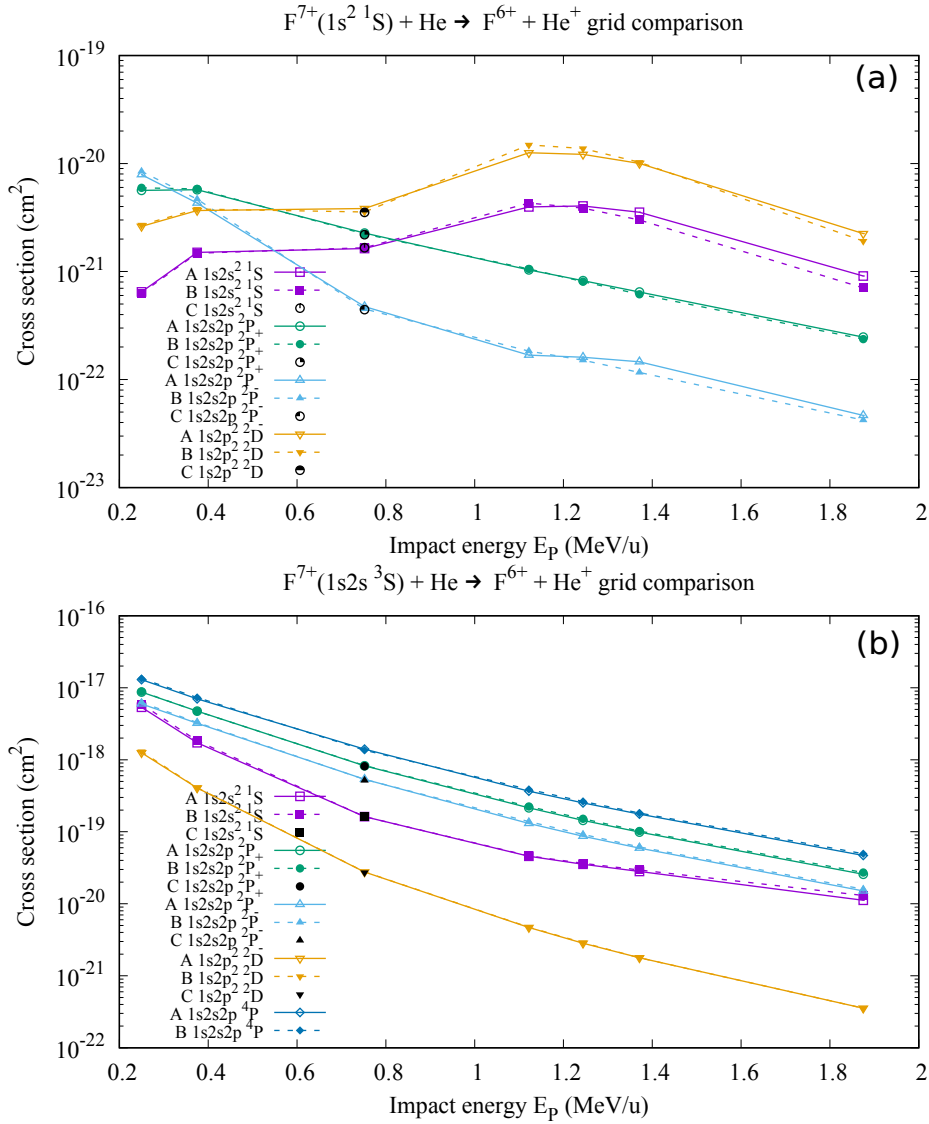


FIGURE 4.17: Convergence of the cross sections of 5 typical channels ($1s2s^2\ ^2S$, $1s2s2p\ ^2P_{\pm}$ and 4P and $1s2p^2\ ^2D$) for two F^{7+} initial states $1s^2\ ^1S$ and $1s2s\ ^3S$ in panels (a) and (b), respectively. A, B and C stand for the three different sets which define the collision zone, "-100 100 100", "-200 200 300" and "-200 200 200", respectively. See text for explanation.

sections present very different values and energy dependencies for the C^{4+} - He system (see also the following Figures 4.20-4.23), one may imagine that an exact knowledge of the metastable states contributions may change significantly the observed differences, especially when taking into account their energy dependences: 10% of differences in the contribution of an initial state which has 1 or 2 orders of magnitude larger cross sections may change drastically our averaged cross sections shown in Figure 4.18.

We are now going to show the state-to-state cross sections for the states

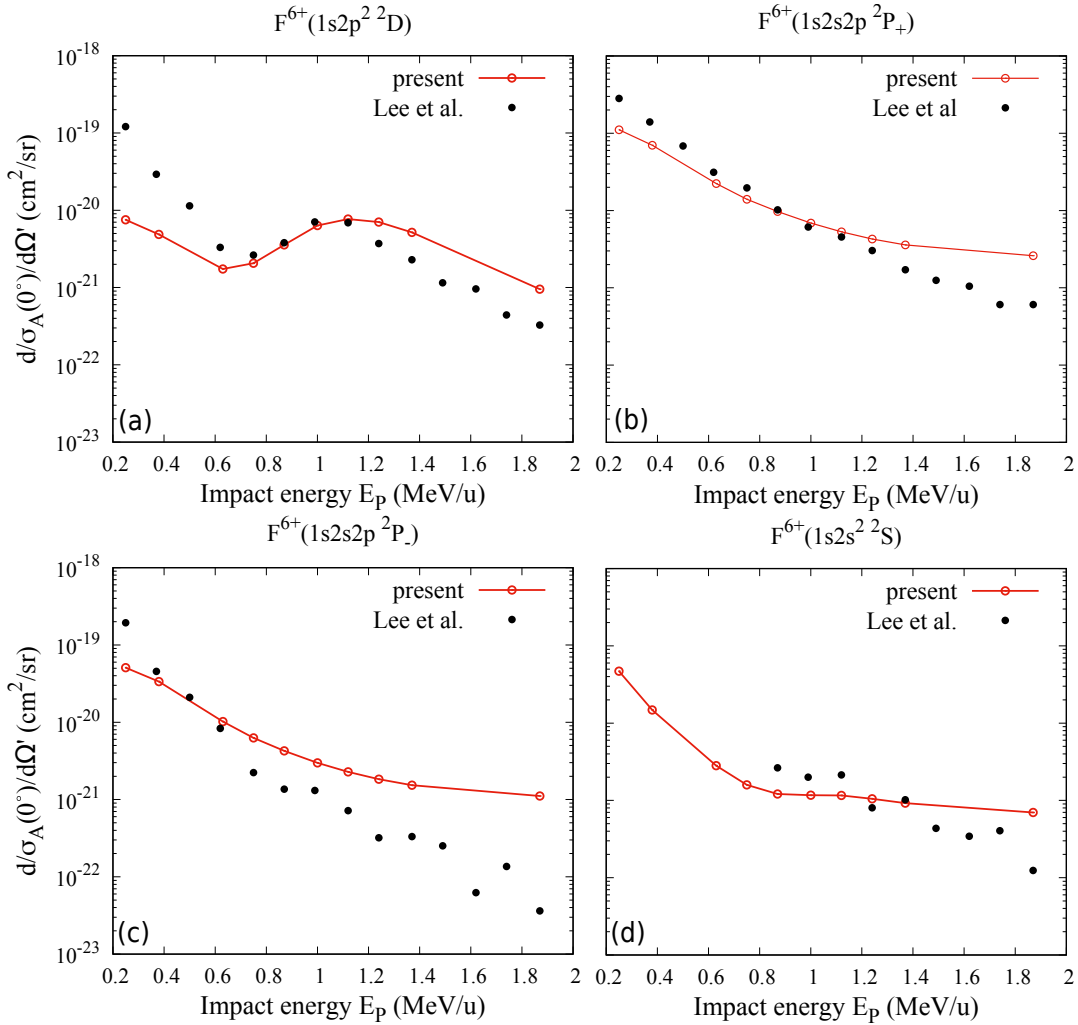


FIGURE 4.18: The Auger SDCS for the four states (a) $1s2p^2\ ^2D$, (b), (c) $1s2s2p^2\ P_{\pm}$ and (d) $1s2s^2\ ^2S$. Our present calculations are shown in open red circles linked with red line while Lee et al. [115] experiment in solid black circles.

of interest, including all M_L components. Figure 4.19 shows the cross sections for production of the $F^{6+}(1s2s^2\ ^2S)$ for the three initial F^{7+} states with the averaged one. As for carbon projectile, the single electron transfer to $1s2s\ ^3S$ dominates, followed by the one to $1s2s\ ^1S$ whose cross sections evolves parallelly in the whole energy domain. For the initial ground state case, the transfer-excitation is much weaker since of bi-electronic nature, especially at low energies, for the same reasons as the ones exposed for carbon projectile. However one can observe a resonant peak around 1.1 MeV/u, i.e. 21 MeV, as predicted in the Impulse approximation RTE calculations shown in [115]. This results in a shallow shoulder of the averaged cross sections which can be seen Figure 5(d) of [115]. If we had increased the ground state contribution 5-10%, i.e. from

70% to $\approx 75\%$, the agreement with Lee experiments (Figure 4.18(d)) would be much better. Note that the magnitudes of the cross sections are quite close to the ones calculated for the C^{4+} projectile.

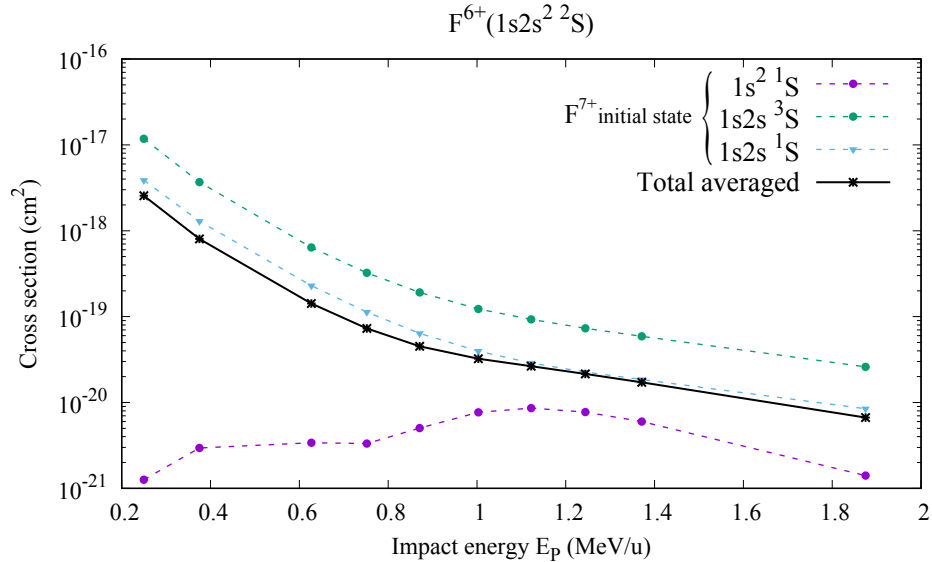


FIGURE 4.19: Total cross sections of production of the $1s2s^2\ ^2S$ state in solid black line along with the cross sections averaged over our hypothetical contribution of the three F^{7+} states in the beam.

Let us turn to the production of the two $1s2s2p\ ^2P_{\pm}$ by single electron transfer. The related cross sections are presented in Figure 4.20 (left panels for $^2P_+$ and right for $^2P_-$), which includes also the M_L -resolved cross sections (lower panels). For the two levels, the present cross sections are lower in magnitude compared to the C^{4+} projectile case but show similarities with the previous system: the total dominance of the single electron transfer to the metastable states and the negligible cross sections for the transfer-excitation for F^{7+} ground state. The $M_L = 0$ components are again the main channels induced during transfer and transfer-excitation processes.

For completeness, Figure 4.21 shows the cross sections of formation of the last level related to the $1s2s2p$ electronic configuration, i.e. the quartet 4P states, evidently possible only from the initial $1s2s\ ^3S$ state. The 4P corresponds to the largest cross sections, as for C^{4+} projectile in the previous section.

Finally we focus on the $1s2p^2\ ^2D$ states which can be produced by transfer-excitation for the three initial F^{7+} states considered. Figure 4.22 shows the cross sections of formation of the 2D from the three initial projectile states. Similarly to the case of carbon projectile, one can clearly observe the resonant peak attributed to RTE, though shifted to somewhat higher collision energies,

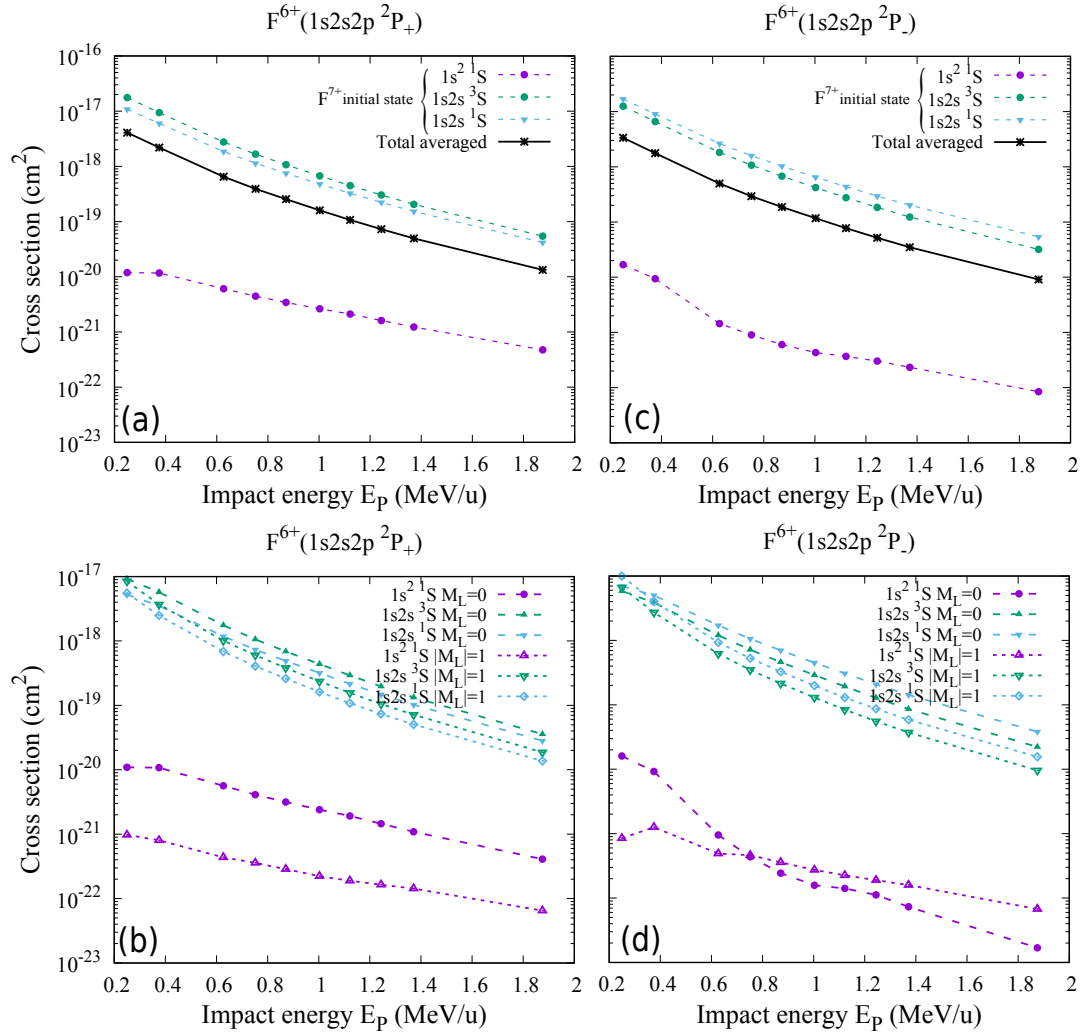


FIGURE 4.20: Cross sections for the production of the $1s2s2p\ ^2P_+$ (left panels) and $^2P_-$ (right panels) for the three projectile initial states. The two upper panels show the total cross sections while the two lower panels the cross sections of the M-components of the $1s2s2p^2P_{\pm}$. In the upper panels, the solid lines show an averaged cross sections, using 70%, 25% and 5% for $1s^2\ ^1S$, $1s2s\ ^3S$ and $1s2s\ ^1S$, respectively.

at around 1.1 MeV/u (21 MeV) due to the difference in resonance energy for this system. However it is a bit shifted compared to the experimental results (see Figure 4.18 (a)) and the impulse approximation RTE calculations reported in [109], which show a peak centred at 20 MeV. This difference is rather small but may question the accuracy of the impulse approximation and also on the ratios used in our procedure to average the cross sections shown in Figure 4.18 (a).

Unlike the C^{4+} projectile case, the transfer-excitation process from the $1s2s\ ^3S$ initial state dominates strongly the ones from the $1s2s\ ^1S$, with cross

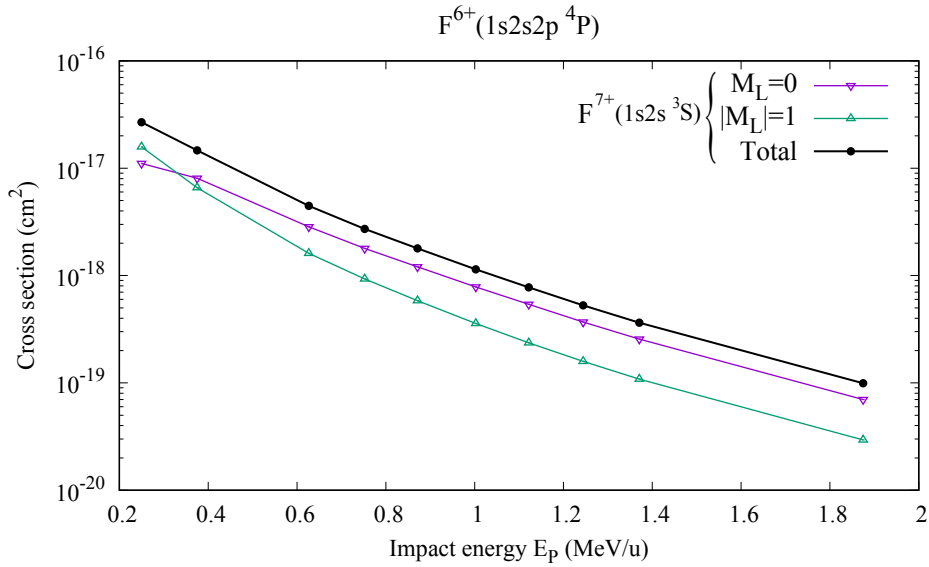


FIGURE 4.21: Cross sections for the production of the quartet state $1s2s2p\ ^4P$ by capture from the $F^{7+}(1s2s\ ^3S)$ initial states.

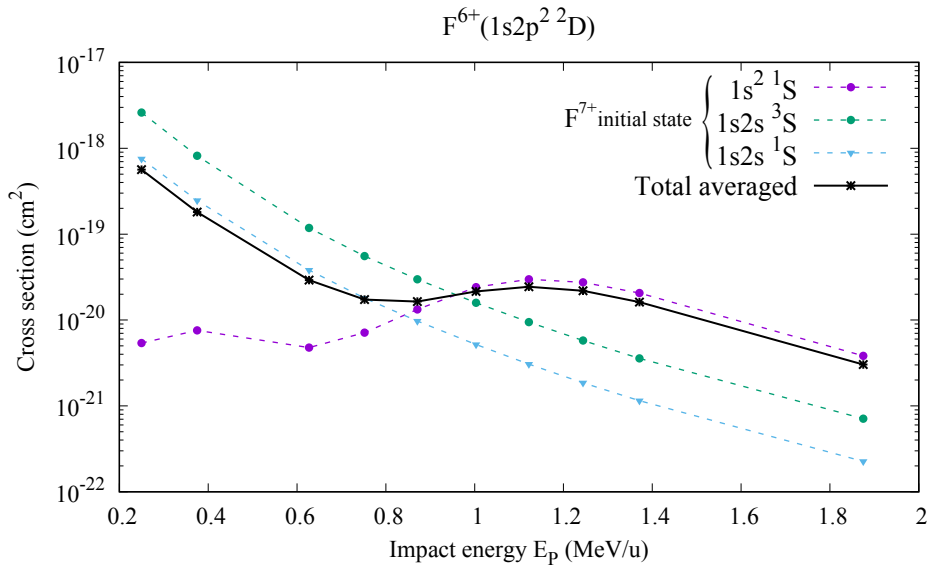


FIGURE 4.22: Cross sections for the production of the $1s2p^2\ ^2D$ state as function of energy for the three initial F^{7+} states. Total averaged cross sections correspond to the combination of the cross sections for 70%, 25% and 5% of the $1s^2\ ^1S$, $1s2s\ ^3S$ and $1s2s\ ^1S$ initial states, respectively.

sections about four times larger in the whole energy domain. At low energies, below 0.6 MeV/u, the cross sections for the $1s^2\ ^1S$ initial states are from 1 to 3 orders of magnitude smaller than the ones for $1s2s\ ^3S$ and one can imagine again that a small difference, i.e. about 5%, in the contribution of the latter state in the beam would change significantly the results shown in Figure 4.18(a).

As for the C^{4+} case, to investigate further the production of $1s2p^2\ ^2D$ we show in Figure 4.23 the M_L -resolved cross sections for the important initial states, i.e. the two main F^{7+} states lying in the projectile beam in experimental investigations. For the ground state, one can observe that transfer-excitation process mainly produces the $M_L = 0$ magnetic state, as for C^{4+} collisions, except at the lowest energies where the cross sections for $M_L = 0$ and $|M_L| = 1$ get very close. As mentioned for C^{4+} , in the RTE peak region where the production of $M_L = 0$ magnetic state dominates largely, the electron-electron interaction is important since explaining the process in the inverse Auger process interpretation and no significant transfer of angular momentum occurs during the collision [120]. For the $1s2s\ ^3S$ initial state, the production of 2D in the $|M_L| = 1$ magnetic states dominates the transfer-excitation process, as for C^{4+} : the inverse Auger process cannot be advocated in this case and the electron-nucleus couplings play also an important role, affecting the population of the three magnetic substates of 2D . Indeed in this case, the population of the $|M_L| = 2$ components is not negligible at low energies, this effect being weaker for C^{4+} projectile.

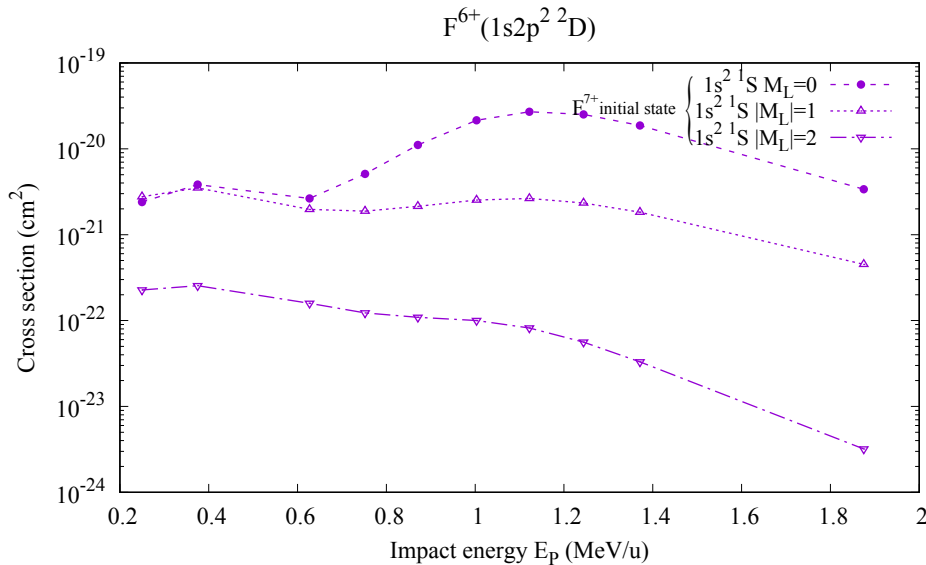


FIGURE 4.23: The energy dependence of $F^{6+}(1s2p^2\ ^2D)$ M_L -resolved cross sections for the $1s^2\ ^1S$ projectile ground state.

To get further insight on the transfer-excitation to produce the 2D from the F^{7+} ground state, we have performed restricted close-coupling calculations, limiting the basis set (used in the calculations presented so far and including 1608 states) to solve the coupled differential equations (eq. 2.34):

- A first one where we included only the initial and final channels (6 states in total): it is named "2-level CC" in the following and equivalent to the ones used for C^{4+} case. This model, somewhat equivalent to a perturbative approach, is designed to probe the existence of the high energy peak (we include the two-centre electron-electron interaction) and also of the, not yet commented, low energy peak.
- A second one where we included the initial channels and $1s2s^2\ ^2S$, $1s2s2p\ ^2P_+$ and $^2P_-$ and the $1s2p^2\ ^2D$ (13 states in total) transfer-excitation channels of interest in this section and is named "5-level CC" in the following. This model is only designed to probe the validity of the results of the 2-level models, with respect to the more converged ones, stemming from the large basis sets described at the beginning of this section.

The cross sections for 2D production (corresponding to all M_L magnetic states and to the only important $M_L = 0$ one) from these two models are presented in Figure 4.24, together with the results from the full close-coupling calculations (as shown in Figure 4.22 and 4.23).

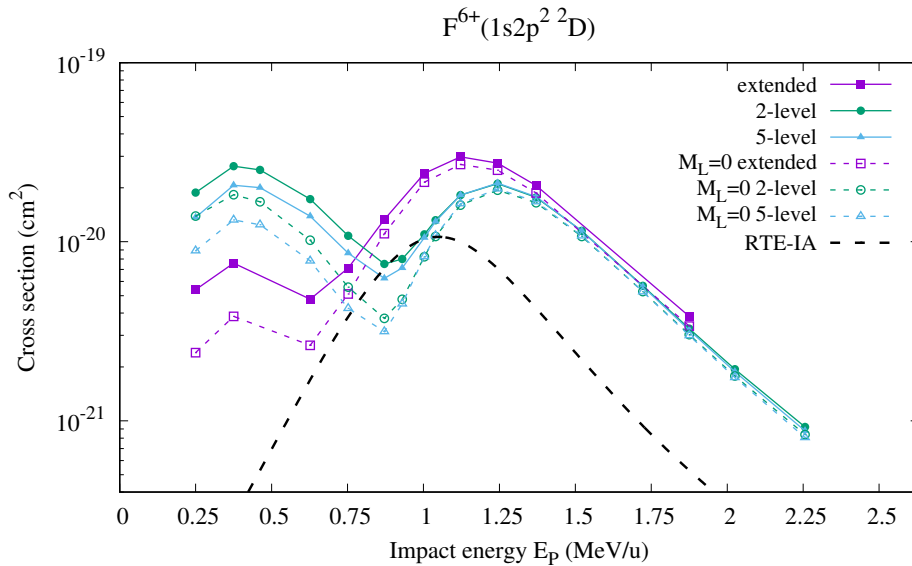


FIGURE 4.24: Cross sections of production of $1s2p^2\ ^2D$ and its $M_L = 0$ component as function of impact energy. Violet lines and squares: Full (extended) close-coupling calculations; Green lines and circles: restricted 2-level CC calculations; Light blue lines and triangles: restricted 5-level CC calculations. The solid lines stand for total cross sections and the dashed ones for the $M_L = 0$ cross sections. Impulse approximation results are presented in dashed black line.

It is quite interesting to observe that the results from the three calculations present very similar behaviour with respect to impact energy: a low energy peak, at about 0.35 MeV/u, followed by the high energy peak predicted at 1.1 MeV/u, as mentioned before, by the extended calculations and at 1.2 MeV/u by the two restricted ones, which converge for energies above 1 MeV/u. The proportion of the $M_L = 0$ component in the total cross sections is quite close in the three series of results. These similarities and differences, notably the 0.1 MeV/u shift of the maximum of the second peak, may shed light on the process of transfer-excitation and on its modelling:

- Firstly, the convergence of the two limited basis calculations at high energies ($E_P > 1$ MeV/u), also with the extended ones at E_P larger than 1.5 MeV/u, shows the soundness of the close-coupling results, free of numerical and basis dependence problems which may occur in close-coupling calculations.
- Secondly, the similarity of the energy dependence of the cross sections from these limited basis and the extended basis calculation indicates the same soundness. However the small shift of the second peak maximum tends to demonstrate that the mechanism responsible from this structure involves indeed a resonant phenomenon between the initial and the final channels but also couplings between other non autoionising states included in the extended basis but absent in the 2-level and 5-level CC models. It is therefore not surprising to observe a difference between our results and the simple impulse approximation RTE model (also included in Figure 4.24) which predicts a maximum at 1 MeV/u. The latter approximation gives a first reasonable prediction of the position of the maximum and on the main interactions responsible of transfer-excitation in this energy range (with the elucidating picture of inverse Auger process) but not fully quantitative information, notably in term of strength of the process.

In addition, the differences in actual values of the cross sections stemming from our three calculations demonstrate also that, in this range of rather high impact energies, non perturbative approaches are required to reach convergence.

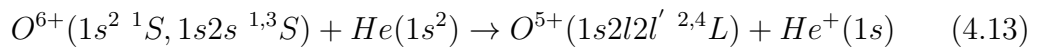
Finally, turning to the low energy peak, the remark just above gets even more evident. Concerning the mechanism responsible of this structure, the model of successive and independent projectile excitation and transfer advocated qualitatively in the past [98, 128] is not demonstrated by our restricted basis calculations. In this regime transfer-excitation proceeds through a more complex and correlated mechanism. However, for this system, the rather old

experimental results, though statistically converged and covering the full energy range of interest, cannot be straightforwardly used to probe theory and models since the extraction of the different components ratio in the ion beam could not be figured out.

There exist convergence points between our studies of transfer and transfer-excitation for C^{4+} and F^{7+} projectile colliding on He. Since for the latter case only rather old results exists, with the limitations mentioned just above, it would be interesting to tackle other collision systems, with results stemming from new converged results of theoretical and experimental investigations. It is what was planned with our collaborators working at "Demokritos's" accelerator facilities in Greece and the aim of the following section.

4.5 The O^{6+} - He collision system

We extend the study of transfer and transfer-excitation to another helium-like projectile. We chose an intermediate ion between C^{4+} and F^{7+} , and O^{6+} seems to be a good candidate, also from an experimental point of view. We focus on the same Auger spectroscopy observable states as for C^{4+} and F^{7+} , i.e. $1s2s^2\ ^2S$, $1s2s2p\ ^2P_{pm}$ and 4P and $1s2p^2\ ^2D$, i.e.,



for collision energies ranging from 0.45 to 1.5 MeV/u. As in the previously discussed collision systems, experimental investigations shall again face the problem of mixed state projectile beam and therefore, we present here the results from calculations performed for the same three initial states of O^{6+} , ground state $1s^2\ ^1S$ and metastable $1s2s\ ^1,3S$.

Note also that this collision system have been already studied thoroughly both theoretically and experimentally, concerning one- and two-electron processes, among others let us mention at low energies [129–133] and at high energies [134, 135]. Our recent calculations may allow to go back to some of these studies and elucidate the interpretations, especially concerning the two-electron processes, but, in this thesis, we shall focus on the same goal as for C^{4+} and F^{7+} , for coherence.

4.5.1 Calculation details

The results presented in this section correspond to the same approach used for C^{4+} and F^{7+} projectiles. For the projectile, the GTO set has been obtained

using the same Z_P^2 , scaling law as for carbon, i.e. by multiplying the exponents used for carbon by a factor $(8/6)^2$ (they are listed in Appendix A). This means a similar quality for the energies of the states of interest in the present study, given in Table 4.4 for O^{5+} and O^{6+} , with the corresponding experimental data [73, 136], for comparison. Again, we see a very good agreement with these data, better than around 0.2%. This GTO set allows us to build a basis set composed of 1357 (694 PPP and 663 PTP) states, representing several thousands of computation hours. Following the test we did for F^{7+} projectile, we use a (-200,+200) collision zone and 300 mesh points to ensure good convergence with respect to these parameters.

TABLE 4.4: Comparison of energies, in a.u., of O^{5+} and O^{6+} states, based on the GTO basis set and the NIST data [73] and reference [136]

| State | O^{6+} | | | State | O^{5+} | | |
|--------------|-----------|-----------|---------------|------------------|-----------|-----------|---------------|
| | E_{GTO} | E_{Ref} | $\Delta(\%)*$ | | E_{GTO} | E_{Ref} | $\Delta(\%)*$ |
| $1s^2 \ ^1S$ | -59.1298 | -59.1935 | 0.108 | $1s2s^2 \ ^2S$ | -43.9811 | -44.0354* | 0.123 |
| $1s2s \ ^3S$ | -38.5335 | -38.5777 | 0.115 | $1s2s2p \ ^4P$ | -43.8502 | -43.9012 | 0.116 |
| $1s2s \ ^1S$ | -38.2463 | -38.2873 | 0.107 | $1s2s2p \ ^2P_-$ | -43.5165 | -43.5944 | 0.179 |
| | | | | $1s2s2p \ ^2P_+$ | -43.3077 | -43.3878 | 0.185 |
| | | | | $1s2p^2 \ ^2D$ | -43.1401 | -43.2303 | 0.209 |
| | | | | $1s2p^2 \ ^2P$ | -43.1013 | -43.1105 | 0.201 |

* $\Delta = |(E_{GTO} - E_{Ref})/E_{Ref}| \times 100$

* Reference [136]

4.5.2 Results and discussion

The cross sections of production of the $1s2s^2 \ ^2S$ and $1s2s2p \ ^2P_{\pm}$ are presented in Figures 4.25 and 4.26, respectively, for the three initial states potentially present in beams produced in tandem accelerators. To give information about the magnitude of the yields which can be directly measured in experiments, we show also the averaged cross sections using the (typical) contributions of the three initial states assumed for F^{7+} , i.e. 70% for ground state, 25% for $1s2s \ ^3S$ ($\tau = 960\mu s$) and 5% for $1s2s \ ^1S$ ($\tau = 0.43\mu s$).

In Figure 4.25 one can observe again the weakness of the transfer-excitation process from the projectile ground state, compared to single transfer to $2s$ on $O^{6+}(1s2s)$ initial states. The resonance peak at about 0.9 MeV/u observed for the ground state is present, as for fluorine, but with a smaller magnitude. The averaged cross sections show a much weaker decrease (about a factor 20) for

increasing impact energies compared to the two previous projectiles (1-2 orders of magnitude), so that their values are somewhat larger for high energies and much smaller for the lowest considered energies.

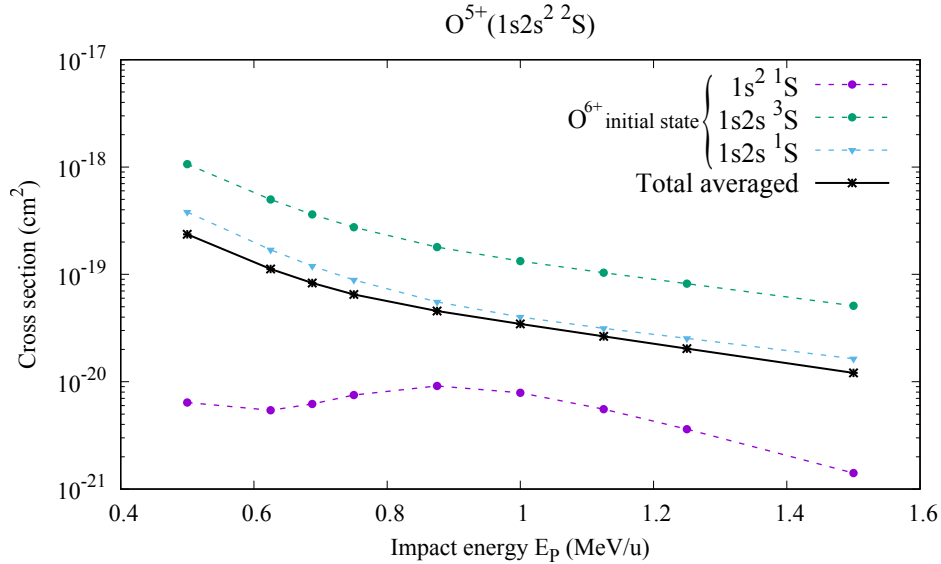


FIGURE 4.25: Cross sections of production of the $1s2s^2\ ^1S$ state as function of impact energy for $O^{6+}(1s^2\ ^1S, 1s2s\ ^{1,3}S)$ collision with He. As for F^{6+} - He collision system, the averaged cross section is evaluated with the combination of 75%, 20% and 5% of the $1s^2\ ^1S$, $1s2s\ ^3S$ and $1s2s\ ^1S$ initial states, respectively.

Regarding the $1s2s2p\ ^2P_{\pm}$ states production, Figure 4.26 shows an analogous behaviour of the cross sections compared to the carbon and fluorine cases. The production of the two 2P levels is favoured from the initial metastable states, i.e. the single electron transfer being largely more likely than transfer-excitation. This difference seems to be significantly more pronounced than for the two other projectile. This may result in a problem to extract the different contribution from experimental measurements. However since, again, the energy dependence of the cross sections is weaker in the O^{6+} case, the averaged cross sections are then smaller at low energies (due to the 70% weighting factor of transfer-excitation from ground state) but larger at high energies. Finally, the lower panels of Figure 4.26 show that the M_L dependence of the cross sections is quite similar to the previous cases.

Figure 4.27 shows the M_L -resolved cross sections for the formation of the quartet state $1s2s2p\ ^4P$ by single transfer from the metastable $1s2s\ ^3S$ state: this is the dominant channel among the two other ones related to the $1s2s2p$ electronic configuration. The process is less likely than for carbon and fluorine projectile. Again we observe a striking difference since in the present case,

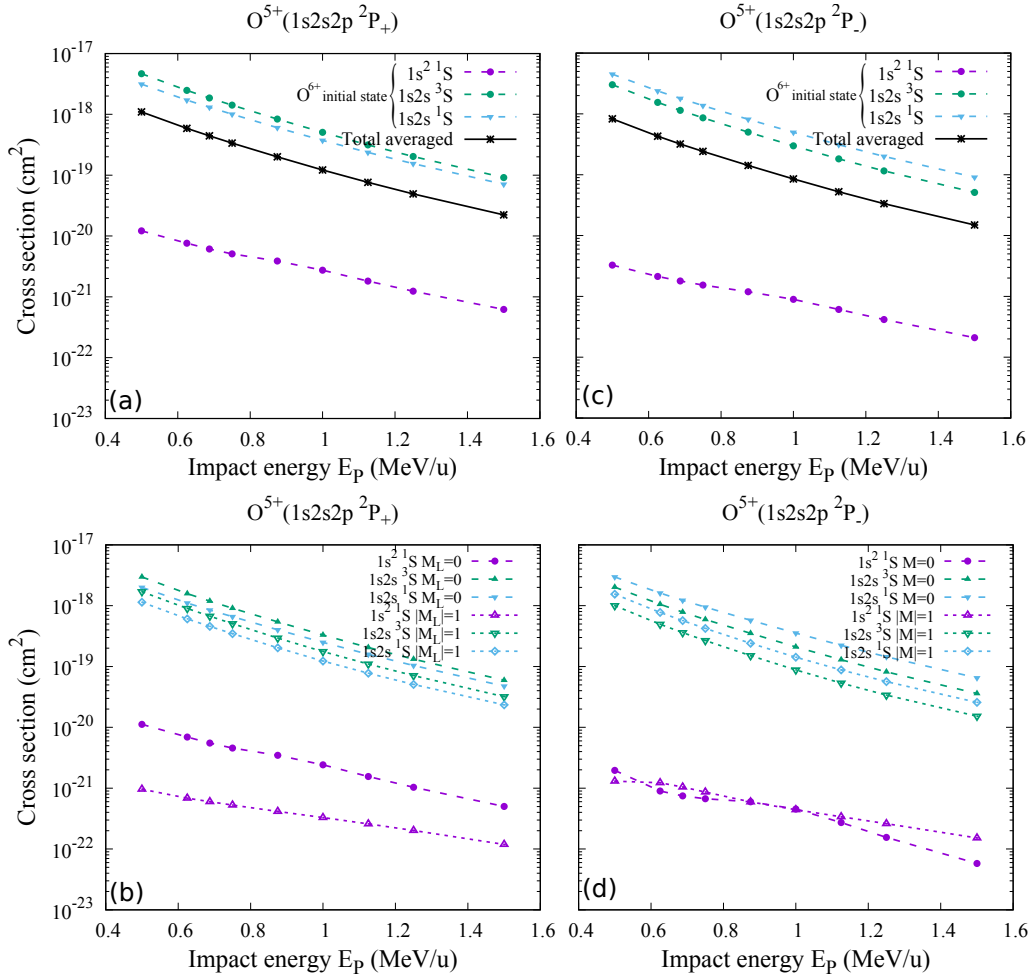


FIGURE 4.26: Cross sections for the production of the $1s2s2p\ ^2P_+$ (left panels) and $\ ^2P_-$ (right panels) for the three projectile initial states. The two upper panels show the total cs while the two lower panels the cs of the M_L -components of the $1s2s2p\ ^2P_{\pm}$. In the upper panels, the solid lines show an averaged cs , using 70%, 25% and 5% for $1s^2\ ^1S$, $1s2s\ ^3S$ and $1s2s\ ^1S$, respectively.

the cross sections vary in a ratio of 1/40 while for C^{4+} it is 1/10000 and for F^{7+} 1/300, when the impact energy is increased. This difference would require a deeper analysis of the results, also with respect to the electronic energy diagrams of these different ions. Last, the $M_L=0$ component is again the most likely populated and doesn't seem to show the inversion observed for carbon and fluorine at the lowest energies.

Next we study the formation of the $1s2p\ ^2D$ states, the cross sections of which are shown in Figure 4.28. We observe again the dominant transfer-excitation process from the ground state at high energies where the inverse Auger process is qualitatively illuminating, with a peak centred around 0.9

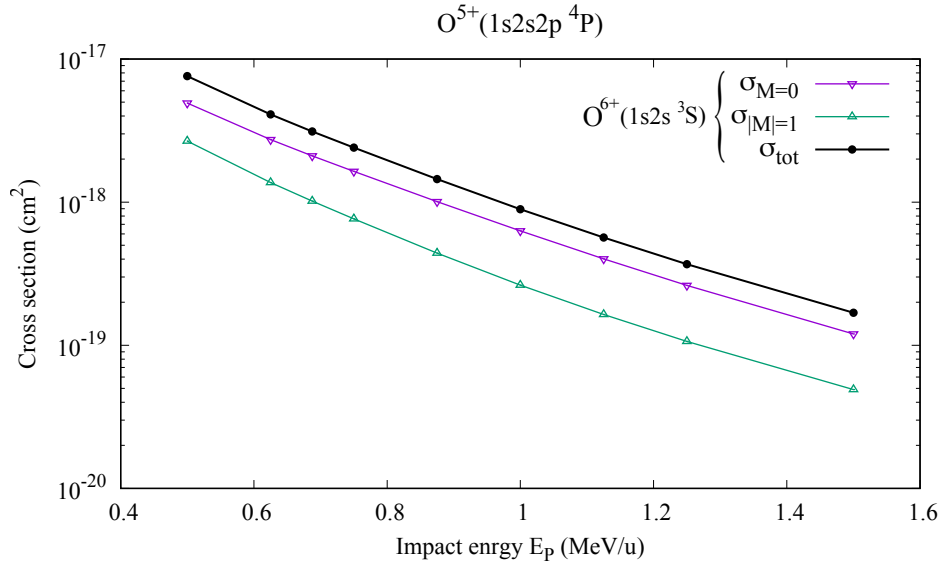


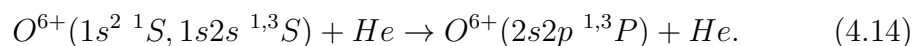
FIGURE 4.27: Cross sections of production of the quartet state $1s2s2p\ ^4P$ by capture from the $O^{6+}(1s2s\ ^3S)$ initial state.

MeV/u. The low energy peak is not visible in the figure since expected to appear at lower energies. At low energies, the dominant transfer-excitation process is the one from the metastable initial states. It is interesting to note that the cross section ratio between $1s2s\ ^3S$ and $1s2s\ ^1S$ states is about the spin statistic ratio, i.e. 3 in favour of the $1s2s\ ^3S$, for the whole energy domain. This feature is found in F^{7+} while for the C^{4+} case the ratio is smaller than 2. When considering the averaged cross sections, from carbon to fluorine, one can observe a progression in the shape of the RTE peak, from a shoulder to a clear peak.

In the last part of this work, we present in Figure 4.29 the M_L -resolved cross sections for the 2D production from the $1s2\ ^1S$ initial state. They present very similar tendencies as the ones observed for the two other ions: a large dominance of the $M_L = 0$ components for the whole energy region, while the cross section for $|M_L| = 1$ are negligible, except to the lowest energy considered.

4.5.3 Projectile excitation to $2s2p\ ^{1,3}P$

For this system and due to ongoing experimental investigations we have focused also on O^{6+} excitation process to produce doubly excited states, and more specifically, on the channels



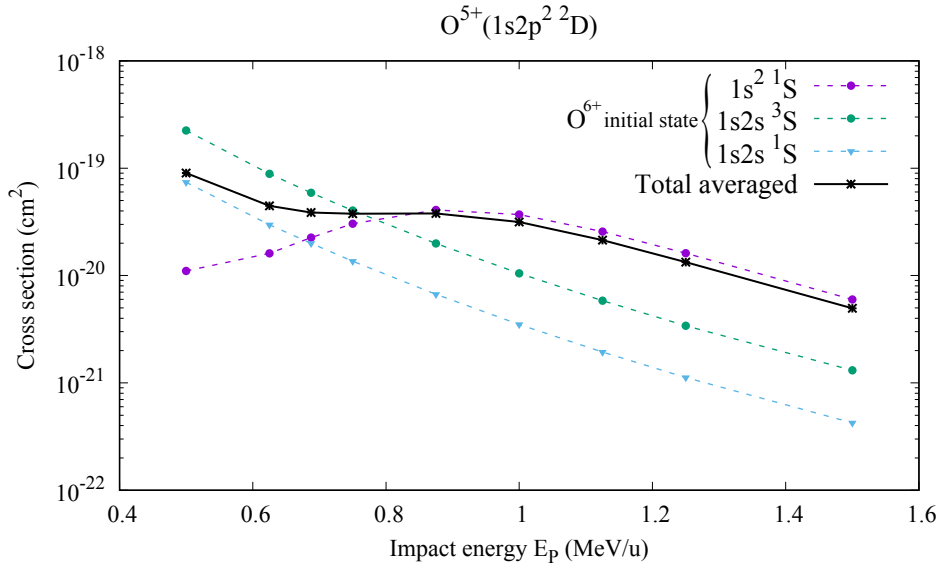


FIGURE 4.28: Cross sections for the production of the $1s2p^2\ ^2D$ state as function of energy for the three initial O^{6+} states. Total averaged cross sections correspond to the combination of the cross sections for 70%, 25% and 5% of the $1s^2\ ^1S$, $1s2s\ ^3S$ and $1s2s\ ^1S$ initial states, respectively.

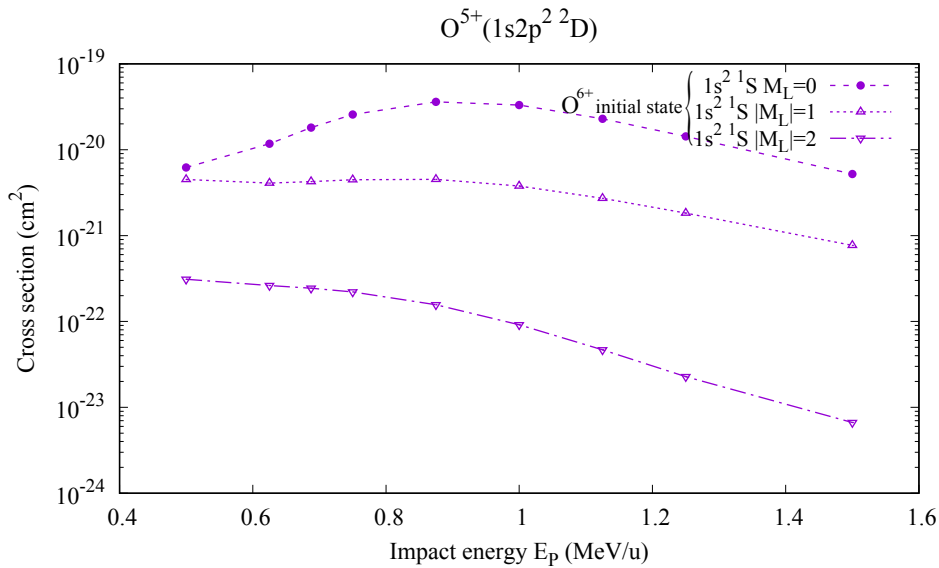
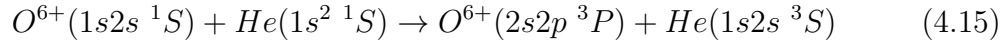


FIGURE 4.29: The energy dependence of $O^{5+}(1s2p^2\ ^2D)$ M_L -resolved cross sections for the $1s^2\ ^1S$ projectile ground state.

Before the presentation and discussion of our results, it is important to note that the triplet and singlet $2s2p$ doubly excited states can be both produced by either singlet ($1s^2$ and $1s2s\ ^1S$) and triplet ($1s2s\ ^3S$) projectile initial states. Indeed, for example, the production of $1s2p\ ^3P$ from $1s2s\ ^1S$ is not spin forbidden when the process is accompanied by a target excitation to triplet states,

e.g.



Our three-electron description of the collision system, and particularly the single electron approximation used to model the helium target, cannot account for such simultaneous excitation of the target and projectile centres. However this double excitation process is expected to be far less likely than the single electron excitation process. It is even more true when considering the same process from $O^{6+}(1s^2\ ^1S)$ since the production of $2s2p\ ^3P$ requires a tri-electronic process, with a double excitation of the projectile, simultaneously with the target excitation to a triplet state. We therefore restrict our results to the excitation process conserving the spin state of the projectile.

In Figures 4.30 (a) and (b) we show the cross sections of production of $2s2p$ in the singlet and triplet spin states, respectively. Since the singlet state is reachable from the ground $1s^2$ and metastable $1s2s\ ^1S$ states, the averaged cross sections which could be measured in experiments is also included in Figure 4.30 (a), using, respectively, 70% and 5% as typical weights of these initial states in a O^{6+} beam. Similarly the averaged cross sections presented in Figure 4.30 (b) correspond to the cross sections of productions of $2s2p\ ^3P$ multiplied by 25%, for comparison with raw experimental data, before extraction of state-to-state cross sections.

We can observe that the dominant process is the single electron excitation $1s \rightarrow 2p$ from the metastable initial configuration $1s2s$. For the singlet case, the cross sections stemming from the collisions with the projectile ground state are two orders of magnitude lower. It is not surprising since this channel is of two-electron nature and highly endoergic compared to the same process from the singlet metastable, with Q value about 44.6 a.u. (1214 eV) and 23.7 a.u. (645 eV), respectively. The averaged cross sections are therefore totally dominated by the ones obtained for the singlet metastable initial state, and one can imagine again some difficulties to compare with experimental results due to the uncertainty of the contributions of the different components of the beam. In the energy range considered, the cross sections for the two main channels show a quite weak energy dependence, with a slight increase for increasing energies. One can observe that the excitation processes to $2s2p$ in the singlet and the triplet cases are equally likely with cross sections differing from each other by no more than 10%. On the other hand, for the ground state case, we scan the domain where the maximum of the cross sections is located, at about 1 MeV/u,

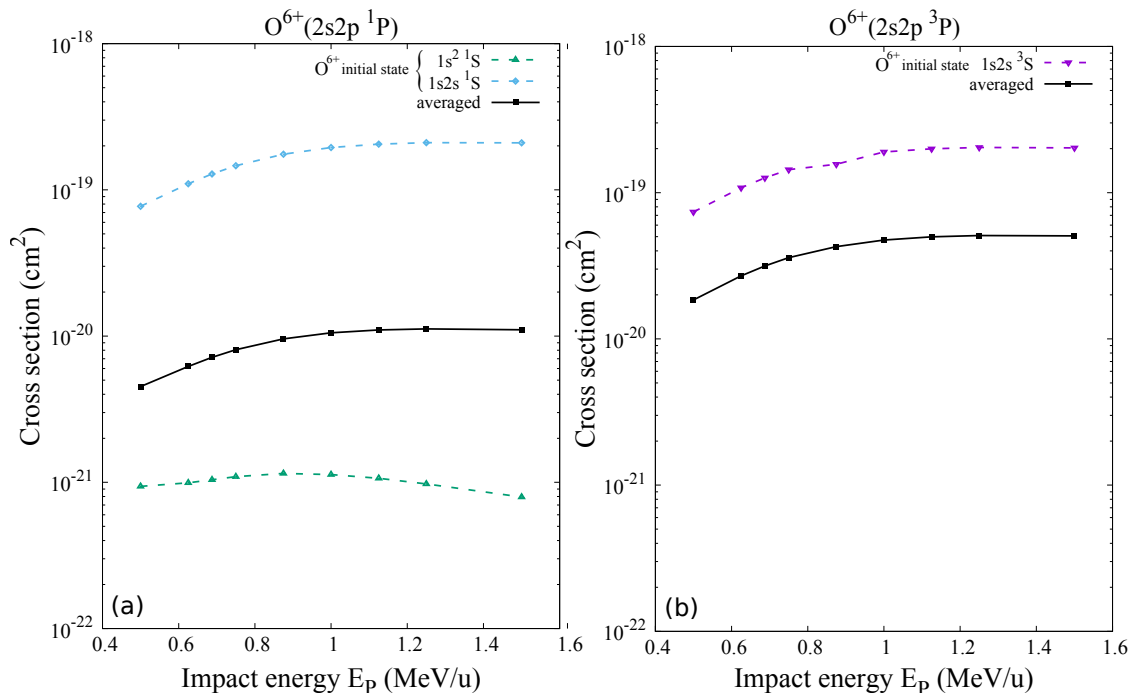


FIGURE 4.30: Cross sections of the production of the (a) $2s2p\ ^1P$ and (b) $2s2p\ ^3P$ doubly excited states. The averaged cross sections correspond to the combination of the cross sections for (a) 70% and 5% of the $1s^2\ ^1S$ and $1s2s\ ^1S$ and (b) 25% of the $1s2s\ ^3S$.

so that the values of the cross sections are about $10^{-21}\ \text{cm}^2$ ($\pm 20\%$) in the energy domain considered.

4.6 Conclusion

In this chapter we have investigated mono- and bi-electronic processes, namely single electron capture and transfer-excitation, occurring in MeV/u collisions between helium-like ions ($Z_P = 6, 8$ and 9) and helium atoms. More specifically we have mainly investigated the production of doubly-excited states $1s2l2l'\ ^{2S+1}L$ after the transfer of a target electron to the projectile initially in the ground state $1s^2\ ^1S$ or in metastable $1s2s\ ^{1,3}S$ states. These latter were considered in relation with experimental studies performed using an up-to-date zero-degree Auger projectile spectrometer setup at Demokritos accelerator facilities in Greece. The originality and the complexity of this work are related to the theoretical description of up to three open sub-shells systems, resulting in a large number of energy levels and the necessity to use a non-mono-electronic treatment. For that purpose we used a close-coupling approach with three active electrons to

describe as well as possible the projectile states under consideration. We have analysed the energy dependence of the cross sections of several of these doubly excited states for different projectile ions and developed mechanisms responsible for these processes. Notably the production of $1s2p^2\ ^2D$ for projectile ground state by transfer-excitation was studied in detail, comparing the results of extended basis calculations with limited ones, including all couplings between the states or neglecting some of them, especially the two-center electron-electron interactions.

For the first time, we were able to validate with an ab-initio treatment, the process of resonant transfer-excitation, signed with a clear peak in the spectra and modelled in the past using an inverse Auger process mechanism. A second structure appearing at lower impact energies and interpreted qualitatively as successive and independent transfer and excitation processes was observed in our results, but this model was questioned for the benefit of a complex correlated mechanism only observable in calculations by close-coupling treatment. This latter was clearly shown to be essential to describe the dynamics of these collision systems despite the high energy domain considered.

Finally we found good agreement with available experimental data, especially for carbon projectile, but for fluorine, the comparison was somewhat less clear since in the quite old experimental investigation, the content of the beams was not clearly defined. The oxygen results were presented for future comparison with ongoing measurement campaign and data analysis.

Chapter 5

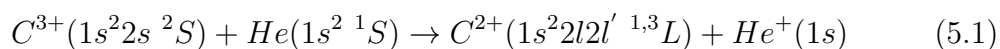
C^{3+} - He collisions: State selective cross sections at low and intermediate energies

5.1 Introduction

As mentioned in the previous chapters, electron transfer processes in highly stripped ions is of great importance not only in fundamental atomic collision physics but additionally in various other fields such as controlled thermonuclear fusion research, and astrophysics.

For example, in the x-ray ionised astronomical environment charge transfer provides a recombination mechanism for multiply charged ions [138]. Furthermore, regarding the thermonuclear fusion technology, carbon is among the major impurities in the magnetic confinement fusion reactors which are also full of the fusion produced helium. Thus the modelling of the electronic processes between these two elements, becomes an important tool for understanding in the plasma ionisation and recombination balance and in the radiative energy loss [139]. Moreover, the charge exchange spectrum, produced by neutral beam injection in tokamak reactor divertors, is also a powerful method for diagnosing any ionic, atomic and molecular impurities of these complex macroscopic systems [140].

In the present chapter, we study again carbon - helium collision system, but for a different charge state of carbon projectile, and focusing on single electron capture and transfer-excitation, that is



for energies ranging from 0.5 to 400 keV/u.

We shall examine the single electron capture process, producing C^{2+} ion, in the $1s^22s^2\ ^1S$, $1s^22s2p\ ^1P$ and $1s^22p^2\ ^1D$ singlet and $1s^22s2p\ ^3P$, $1s^22p^2\ ^3P$ triplet states. This collision system and these specific channels have been already studied theoretically [129, 141–143] and experimentally [129, 141, 143–146] and comparisons will be given for the overlapping collision energies. Furthermore the present work has been initiated after discussion with the group of Prof. X. Zhu in the Institute of Modern Physics of the Academy of Sciences, in Lanzhou, and comparison with their preliminary results will also be provided.

5.2 Calculation details

The calculations performed to obtain the cross sections presented in this chapter are based on the semiclassical close-coupling approach described in Chapter 2, using three active electrons. Indeed, since (i) to allow five active electrons is out of reach in the present time due to computation cost and (ii) the two core electrons are deeply bound and therefore do not participate to the dynamics of the system in the energy range under consideration, the use of the frozen core approximation is possible (and unavoidable). The three-electron treatment allows to take into account 1 electron on C^{3+} simultaneously with 2 electrons on He (and alternatively 2 electrons on C^{2+} and 1 on He^+) giving an excellent description of the valence shell of the two collision partners. For $C^{4+}(1s^2)$ we therefore use the model potential

$$V_P(r) = -\frac{1}{r} \sum_{i=1}^3 c_i e^{-\beta_i r^2}, \quad (5.2)$$

where the values of c_i and β_i (see Table 5.1) were optimised to describe as well as possible the C^{2+} and C^{3+} states. For the carbon centre, we have created

TABLE 5.1: Coefficients and exponents used to represent the system $C^{4+} + e^-$ by the model potential eq. 5.2

| i | 1 | 2 | 3 |
|-----------|-----|-------|-------|
| c_i | 4.0 | 1.465 | 0.535 |
| β_i | 0.0 | 10.75 | 850.5 |

by optimisation a set (called $B_{C_1}^{3e}$, available in Appendix A.6) of 30 GTOs, including 7 for $l = 0$, 4×3 for $l = 1$ and 2×5 for $l = 2$. For helium we used a set (called $B_{He_1}^{3e}$, available in Appendix A.6) of 14 GTOs with 5 orbitals for $l = 0$ and 3×3 orbitals for $l = 1$. With these two sets, the diagonalisation of the C^{3+} , C^{2+} , He^+ and He Hamiltonian allows to produce a basis set of 1542

atomic states, including 442 describing C^{3+} - He channels and 1100 for the C^{2+} - He⁺ channels, some of those states being pseudo-states laying below ionisation threshold and some above, i.e. modelling somewhat ionisation.

In Table 5.2 we present the energies of the atomic states important in our study, for the projectile and target. They are compared with data provided by National Institute of Standards and Technology (NIST) [73] and an excellent agreement is observed with differences below 1%.

TABLE 5.2: Comparison of energies, in a.u., of C^{3+} and C^{2+} , triplet and singlet, based on the GTO basis set and the NIST data

| | | C^{3+} | | | C^{2+} | | | |
|----------------|-----------------|-----------|------------|---------------|--------------------|-----------|------------|---------------|
| | State | E_{GTO} | E_{NIST} | $\Delta(\%)*$ | State | E_{GTO} | E_{NIST} | $\Delta(\%)*$ |
| $B_{C_1}^{3e}$ | $1s^2 2s \ ^2S$ | -2.3658 | -2.3701 | 0.179 | $1s^2 2s^2 \ ^1S$ | -4.1198 | -4.1299 | 0.246 |
| | $1s^2 2p \ ^2P$ | -2.0705 | -2.0763 | 0.281 | $1s^2 2s 2p \ ^3P$ | -3.8813 | -3.8912 | 0.255 |
| | | | | | $1s^2 2s 2p \ ^1P$ | -3.6460 | -3.6636 | 0.480 |
| | | | | | $1s^2 2p^2 \ ^3P$ | -3.4916 | -3.5036 | 0.343 |
| | | | | | $1s^2 2p^2 \ ^1D$ | -3.4494 | -3.4653 | 0.459 |
| | | | | | $1s^2 2p^2 \ ^1S$ | -3.2779 | -3.2983 | 0.620 |

$$* \Delta = |(E_{GTO} - E_{NIST})/E_{NIST}| \times 100$$

In addition, we use also the close-coupling approach restricted to only two active electrons (resulting in much faster computations), i.e. keeping only a single electron on He and therefore using the model potential shown in eq. 4.2 for the He⁺ centre. In this model, we used the same GTOs set on carbon and helium and produced a basis set for the collision which included 557 states, spanning 165 C^{3+} - He channels and 205 (187) singlet (triplet) C^{2+} states.

5.3 Results and discussion

5.3.1 Single electron transfer & transfer-excitation cross sections

We have performed calculations with our 3-electron close-coupling code in the large energy domain 0.5 - 400 keV/u. In limited energy ranges some results were already published theoretically by Wu et al. [142] and experimentally by Lennon et al. [146] and also by our colleagues from the Institute of Modern Physics in Lanzhou who collected new preliminary data, sent to us as private communication. Since the latter results were known only as ratio, we present in Figure 5.1 the cross sections for five important channels (and combination

of them) involving the transfer of one electron from the target to the projectile, normalised over the sum of these cross sections, which represent the main contribution of the total production of C^{2+} ions. For the three other series of results, the same ratio is presented, so that the sum of the five different results are equal to unity for the four investigations. In this figure, one can observe clearly that the most dominant channels are the production of $1s^2 2s 2p$ (in singlet and triplet projectile) for the whole energy domain, the sum of them representing from 70% to 90% of the channels under consideration. While the capture to $1s^2 2s 2p \ ^3P$ increases monotonously for increasing energies, the singlet one decreases before reaching a plateau, contributing to about 20% of the considered channels from 50 to 400 keV/u. This opposite behaviour explains why the $1s^2 2s 2p \ ^3P$ channel becomes largely the dominant one at energies above 1 keV/u. On the other hand, the cross sections of transfer to produce $1s^2 2s^2 \ ^1S$ and of transfer-excitation to $1s^2 2p^2 \ ^3P + \ ^1D$ show a maximum at about 17 keV/u and 2 keV/u, respectively.

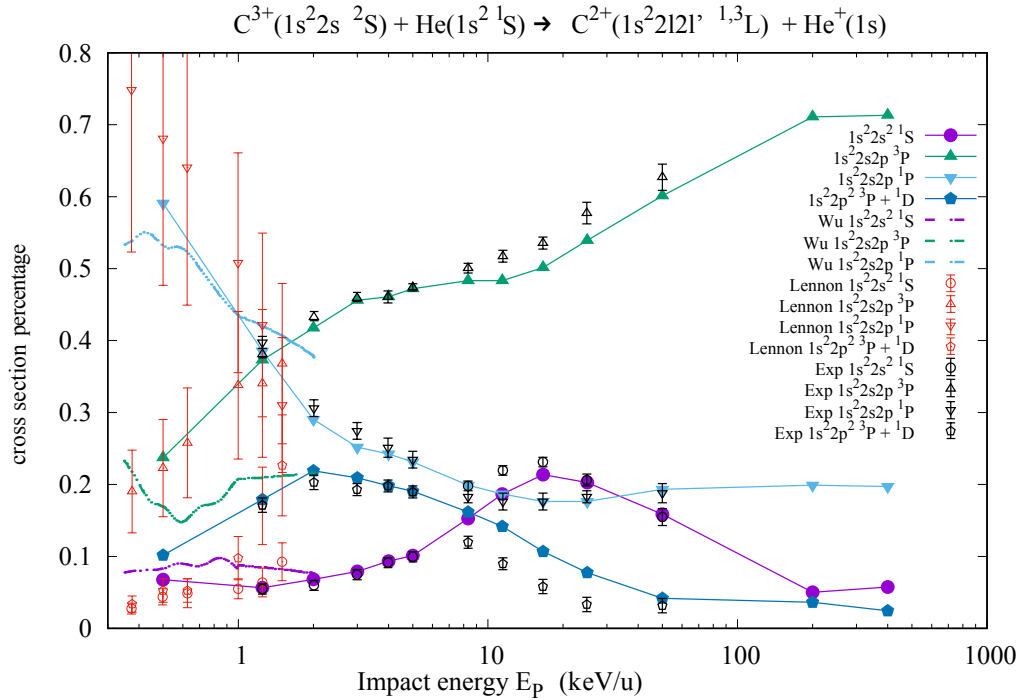


FIGURE 5.1: Normalised (see text) cross sections for the production of $C^{2+} 1s^2 2l 2l' \ ^1,^3L$ states as function of impact energy: $1s^2 2p^2 \ ^3P + \ ^1D$ (blue line with solid pentagons), $1s^2 2s^2 \ ^1S$ (purple line with solid circles), $1s^2 2s 2p \ ^1P$ (light blue line with solid reverse triangles), $1s^2 2s 2p \ ^3P$ (green solid triangle line). Calculations of Wu et al. [142] (same colouring lines). The experimental data are shown with the same marks, red for Lennon et al. [146] and black for Zhu's group experiment [147].

Together with our present theoretical treatment, Figure 5.1 includes the experimental results provided by Lanzhou's team [147]. In this last campaign they managed to distinguish the different channels under consideration, using a high resolution COLTRIMS imaging setup to measure the recoil momenta for each of these channels and obtaining relative related cross sections. The comparison between our results and their experimental data show very good agreement in the entire overlapping energy range 1.25 - 50 keV/u. We agree both qualitatively and quantitatively, especially regarding the two major states produced, $1s^22s2p\ ^1P$ and $1s^22s2p\ ^3P$. The largest disagreement (with differences up to 25%) is observed at 8 - 25 keV/u energies for the weaker channel, the $1s^22p^2\ ^3P + ^1D$ transfer-excitation channel. Figure 5.1 presents also experimental data reported in Lennon et al. [146] for low energies ranging from 0.37 to 2.5 keV/u. These authors have reported measurements on state selective cross sections, normalised to the total SEC cross sections obtained by Iwai et al. [145]. These data were not reported with individual uncertainties but claimed by the authors to have an estimated accuracy well within 20%; we used this latter value to show error bars for this series of data. A quite reasonable agreement is found between these measurements, within their errors bars, and our results, except at specific impact energies for the weakest channels (production of $1s^22s^2\ ^1S$ and $1s^22p^2\ ^3P + ^1D$). This validates our approach and results for such low impact energies, in particular regarding the production of $1s^22s2p\ ^{1,3}P$. On the other hand we show quite significant differences with Wu et al. [142], whose results stem from a quantum mechanical Molecular Orbital Close Coupling treatment. Except the same tendency shown for the dominant process at low energies (production of $1s^22s2p\ ^1P$), these results seem to fail for the other channels states studied. In particular there is large discrepancy, in actual values and energy dependence, concerning the production of $1s^22s2p\ ^3P$, with our results and the experimental data, as can also be seen in Figure 6 of [142] for the comparison of their results with Lennon et al [146] data.

5.3.2 Spin statistics on production of $C^{2+}(1s^22s2p\ ^{1,3}P)$

We focus now on the triplet to singlet ratio ($R = ^3P/^1P$) of the cross sections for production of $1s^22s2p$ electronic configuration. Indeed, the study of this ratio is of interest from a fundamental point of view since it measures, as function of impact energy, the role of electronic exchange effects, energy difference between the related channels and divergence from pure spin statistics (i.e. $R \rightarrow 3$ in

our case)¹. For example, for our collision system, one may expect large difference with this limit at low energy where molecular mechanisms, for example at avoided crossings, are important and depend strongly on the energies of the channels under consideration. At high energy collisions for which 2-state perturbative models may be applied this energy difference becomes less critical and the ratio of the cross sections is expected to reach this pure spin statistical limit.

However to test theoretically this behaviour one needs to perform multi-electron calculations in which the electron exchange terms are taken into account and split energy levels into several spin states, following Pauli exclusion principle. Indeed with single electron approaches and the use of model potentials to describe this degeneracy breaking, the cross sections of different spin (S) states are very close and one has to multiply them by the ad hoc $2S + 1$ factors to take into account the spin of the considered states. It is therefore interesting to use our multi-electronic approach to evaluate this ratio on a wide impact energy and compare with experimental data. Figure 5.2 shows the ratio $R = {}^3P/{}^1P$ obtained in the present work, in comparison with results obtained experimentally [146,147] and theoretically [142]. Our calculations come in good agreement with both Lennon et al. [146] and Zhu's group [147] experiments. On the other hand Wu's calculations [142] present severe discrepancies with the other results, both in shape and absolute values, maybe due to the neglect of the electron translation factor and of the rotational couplings in their calculations.

In Figure 5.2 one can observe that the ratio is smaller than unity for energies below about 1 keV/u. This can be readily explained by the molecular curves of the CHe^{2+} system shown in Figure 5.3 where we use Figure 1(a) of [142] augmented by the information concerning the asymptotic states correlated to the adiabatic energy curves of Σ symmetry. Indeed in Figure 5.3 one can see that the curves, correlated asymptotically to the initial channel experiences an avoided crossing at internuclear distance around 5 a.u. with the one correlated to the $1s^2 2s 2p {}^1P$ transfer channel. This avoided crossing explains the dominance of the transfer to singlet states at low impact energy (e.g. 0.5 keV/u, i.e. velocity $V_P \approx 0.14$ a.u.) while for increasing velocities the avoided crossings at smaller distances get activated to promote the triplet transfer channel (and also the production of $C^{2+}(1s^2 {}^1S)$, as can be seen in the maximum located at about 15 keV/u in Figure 5.1).

This is corroborated by the Figure 5.4 where the reduced probabilities for

¹As in our theoretical treatment, we assume that spin-orbit coupling effects are negligible in the following discussion.

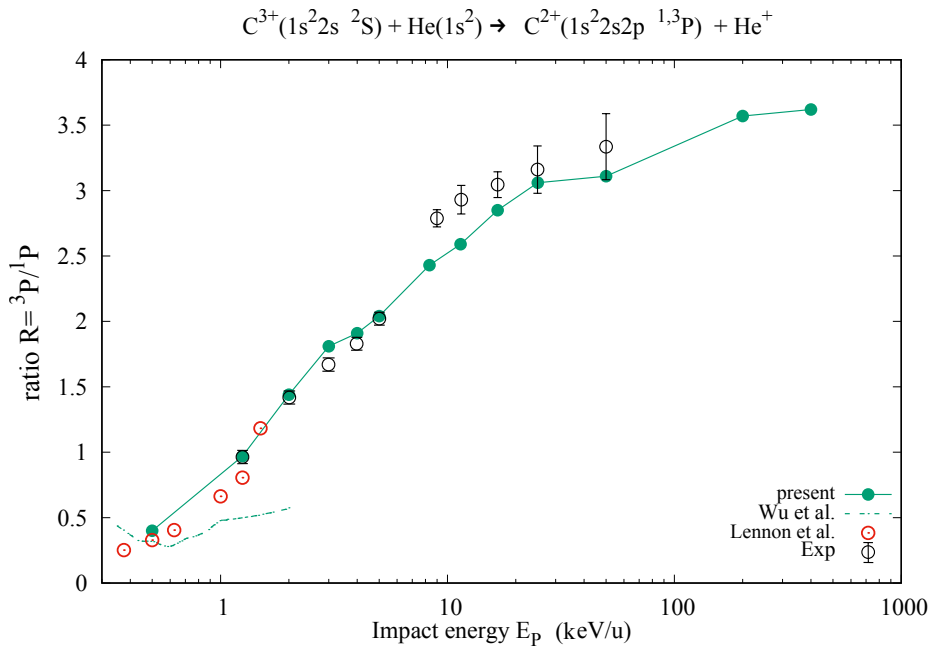


FIGURE 5.2: Triplet over singlet ratio R of SEC to $1s^2 2s 2p^1, ^3P$ in $C^{3+} + He$ collision system. Present calculations (green solid circle line). Calculations of Wu et al. [142] (green dashed line), experimental data of Lennon et al. [146] (red open circles) and Zhu's group experiment [147]. (black open circles)

the two channels $1s^2 2s 2p^1, ^3P$ are shown as function of impact parameter b and for four typical impact energies. For the low energy, panel (a) shows clearly a peak at about $b = 4$ a.u. (followed by typical oscillations) when the system can cross the avoided crossing which explains the transition to the 1P channel, while 3P shows a smaller maximum at 3.5 a.u. For increasing, but still low, energies (panels b and c) the balance between the two avoided crossings changes, favouring the 3P channel. Then, for higher energies (panel d), these complex molecular-type mechanisms cannot be advocated anymore and the results can be qualitatively interpreted by a direct, atomic-type, mechanism and spin statistics. Since the two singlet and triplet channels are asymptotically separated by about 6.5 eV (0.24 a.u., see Table 5.2), the direct mechanism should give close cross sections while the spin statistics will favour notably the triplet channels, with a ratio reaching a value of about 3. However, both our results and the experimental ratio, in agreement with each other, reach a larger value, about 3.3 at 50 keV/u. We have very recently extended our calculations to larger energies, not reachable experimentally in the present time, where the ratio continues to increase and reaches a value of 3.6 at 400 keV/u. This somewhat surprising result is currently being studied for interpretation, the next section showing

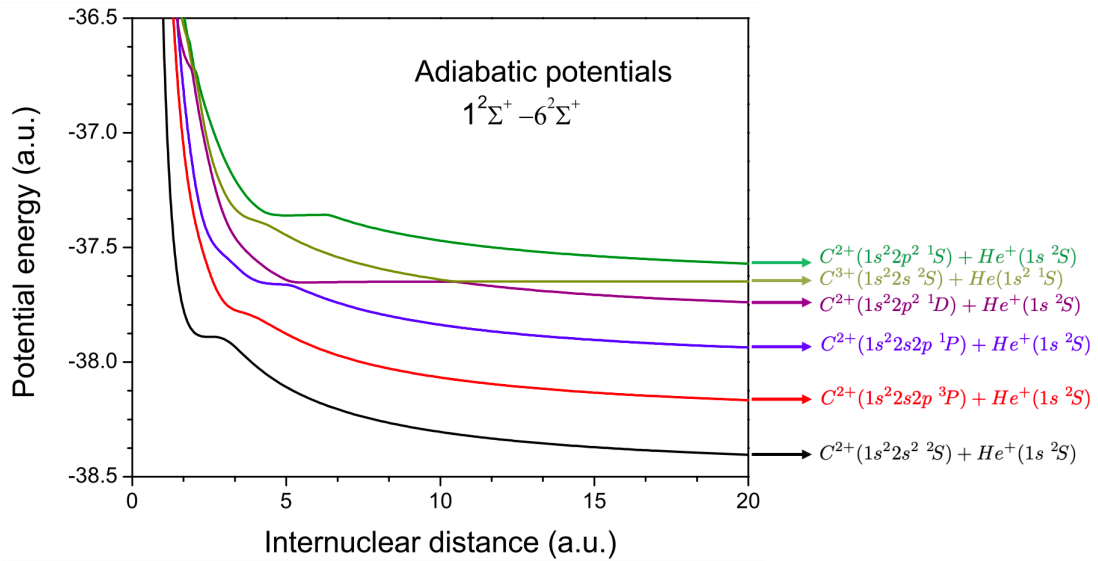


FIGURE 5.3: CHe^{3+} adiabatic Σ energy curves (from Figure 1(a) in Wu et al. [142]). The asymptotic states correlated to the 6 curves are shown on the right side and notably the three channels under consideration: the initial $C^{3+}(1s^2 2s ^2S) - He(1s^2 ^1S)$ one (olive line), and the two transfer channels $C^{2+}(1s^2 2s 2p ^1P) - He^+(1s ^2S)$ (blue line) and $C^{2+}(1s^2 2s 2p ^3P) - He^+(1s ^2S)$ (red line).

one of the direction that we followed.

5.3.3 Two-electron versus three-electron close-coupling approach

Three-electron close coupling investigations, as the present ones, are very rare and require extremely time consuming computations. We have been able to manage such an approach for C^{3+} - He collisions and obtain very good agreement with experiments. It was then tempting to study the same system and processes with a two-electron approach in which one of the electron on He is frozen. We presented in section 5.2 the model potential and basis set used for such calculations. An important point was to keep the same GTO sets as for the three-electron calculations so that the C^{3+} and C^{2+} states were described in exactly the same way, the differences being the description of the active electron states (though expressed with the same GTO set) and the neglect of all couplings involving this second electron (taken into account in the three-electron calculations).

To evaluate the cross section for a process $i \rightarrow f$, we used the independent electron approximation so that the probability $P_{fi}^{He(1s^2)}$ for the process is given

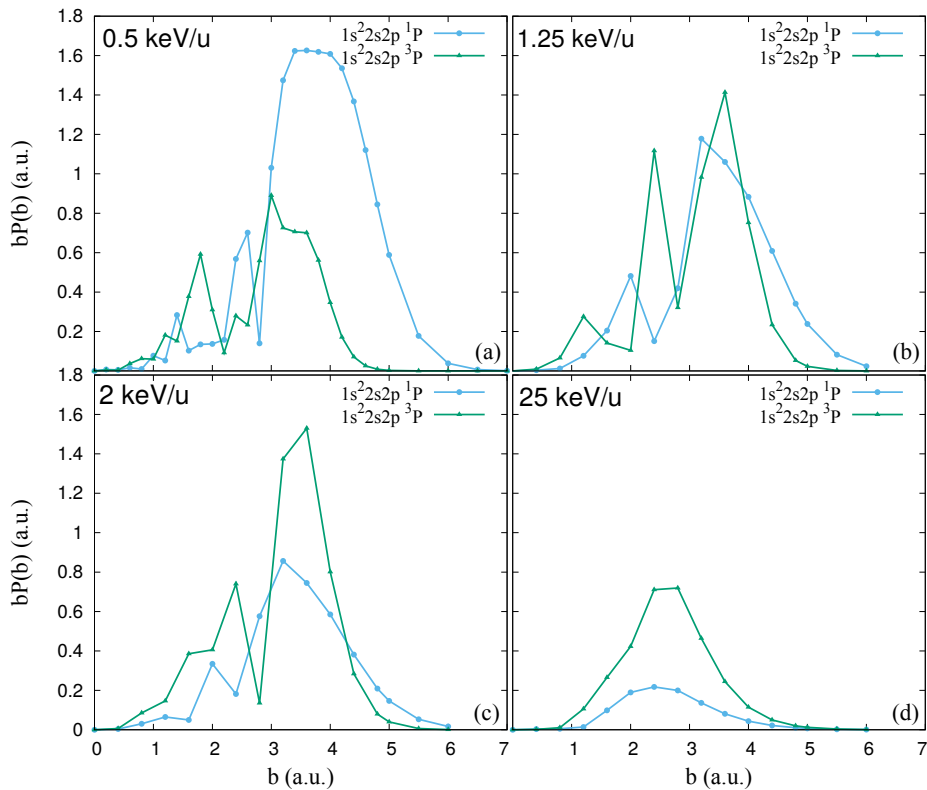


FIGURE 5.4: The reduced probabilities $bP(b)$ for the production of $C^{2+}(1s^22s2p^1P)$ and $C^{2+}(1s^22s2p^3P)$ in light blue and green lines, respectively, at impact energies (a) 0.5 keV/u, (b) 1.25 keV/u, (c) 2 keV/u and (d) 25 keV/u.

by a binomial distribution expressed as

$$P_{fi}^{He(1s^2)} = 2P_{fi}^{He(1s)}(1 - P_{trans}^{He(1s)}) \quad (5.3)$$

where $P_{fi}^{He(1s)}$ is the probability for process $i \rightarrow f$ obtained in the 2-electron calculations and $P_{trans}^{He(1s)}$ the probability of any transfer processes, i.e. of production of C^{2+} . This formula takes into account the transfer of electron 1 to state f while electron 2 is not transferred to the projectile, the factor 2 stemming from the interchange between electron 1 and electron 2. This model is known to overestimate two-electron processes which may be unlikely in reality, underestimating therefore the one-electron processes [148]. In that context, we have done two series of checks:

- In the electronic state basis set we have included C^+ states (opening therefore double capture channels) and performed close-coupling calculations for three energies: the cross sections of production of $C^{2+}(1s^22s2p^{1,3}P)$ were hardly changed ($< 1\%$), by the inclusion of double capture channels.

- We calculated the cross sections for the production of $C^{2+}(1s^2 2s 2p \ ^{1,3}P)$, simultaneous to the excitation of the He^+ . These 2-electron processes were found very weak (about 2 orders of magnitude less probable) at low energies, their contribution increasing for increasing energies, with cross sections about three times smaller at 400 keV/u.

In Figure 5.5 we compare the cross sections normalised to the sum over them (as in Figure 5.1) stemming from the three- and the two-electron approaches. One can observe quite important quantitative differences between these two series of results, though the relative strength of each channel is qualitatively verified. Indeed the main channel is the production of $C^{2+}(1s^2 2s 2p \ ^3P)$ states, except at low energies for which the 1P related states take over. The productions of $C^{2+}(1s^2 2p^2 \ ^1D, \ ^1S)$ and $C^{2+}(1s^2 2s^2 \ ^1S)$ are again the weaker channels but the cross section ratio for the latter shows a larger maximum at about 17 keV/u, as previously observed, and a sudden and surprising increase for energies beyond 200 keV/u.

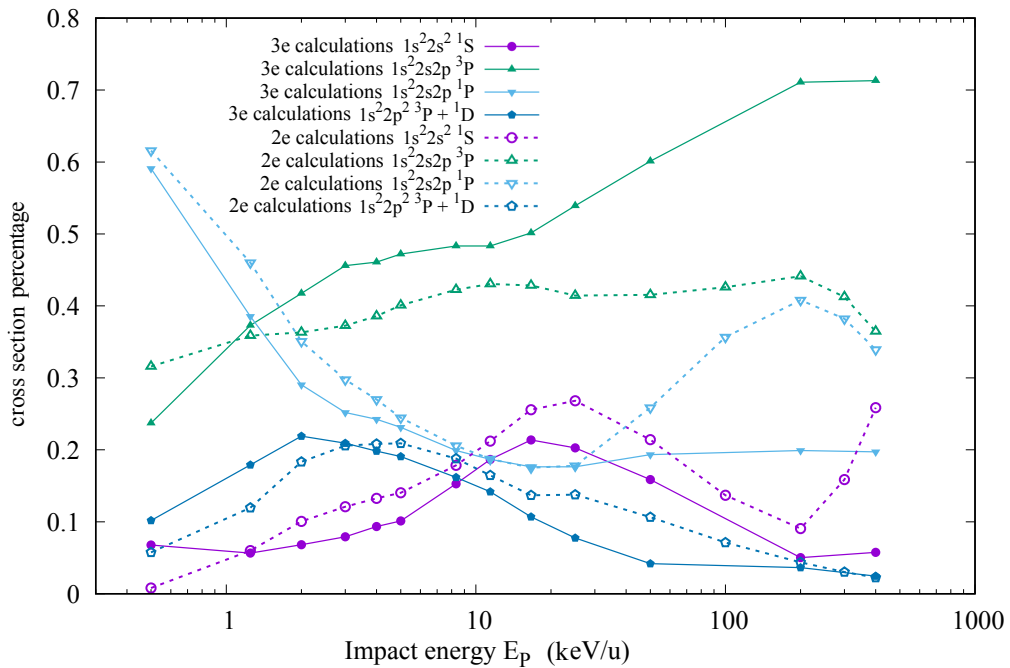


FIGURE 5.5: Comparison of the normalised cross sections as in Figure 5.1 with the ones calculated with the 2-electron approach.

We turn now to the comparison of the ratio R obtained by these two approaches. Before the presentation and discussion of these results, we must describe some important drawbacks of the 2-electron calculations. Indeed, since we describe the helium with a single electron approximation, the target states

are doublet, as the projectile ones. Then, in order to evaluate the cross sections of the states under consideration, we have to perform two series of independent computations, one with singlet and one with triplet total spin. Therefore, with this unavoidable way to take into account singlet and triplet channels, i) we decouple them in an energy range where close-coupling is supposed to be important (below, say, 100 keV/u), and ii) we have to multiply the ratio R by 3 to take into account the spin statistics². Figure 5.6 shows the ratio $R = {}^3P/{}^1P$ from the 3-electron calculations (called R^{3e} in the following) and from the 2-electron calculations using the binomial distribution eq. 5.3, with $R_{\times 3}^{2e}$ the scaling factor 3 and without, R^{2e} .

We observe important differences between the results from the 3-electron approach (in agreement with two series of experimental data, see Figure 5.2) and the two-electron approach. For impact energies below about 20 keV/u, the raw (not scaled by the spin statistic factor) 2-electron results follow, surprisingly, the same trend as the 3-electron ones, with differences smaller than 20%, the ratio monotonously increasing to about 2.5. One may understand this result by the fact that in this energy domain the relative magnitude of the cross sections of 3P and 1P states is mainly controlled by the corresponding energy curves of CHe^{3+} molecular ion and the presence, and the characteristics, of the important avoided crossings. These states seem to couple weakly so that our treatment with two independent singlet and triplet calculations is reasonable. However the spin statistics factor is unavoidable in this approach and the ratio $R_{\times 3}^{2e}$ is in total disagreement with the ratio obtained by 3-electron calculations. Beyond this energy, R^{2e} splits from R^{3e} , decreasing to about 1.07 at the highest energy considered. Accordingly, $R_{\times 3}^{2e}$ decreases towards R^{3e} and tends to a value of 3.2 at 400 keV/u. This result is consistent since, as mentioned before, for the high energy, quasi perturbative, domain, the asymptotic 3P and 1P states correspond to close energy values so that their related cross sections should be comparable (as shows R^{2e}), apart from the spin statistics factor.

Finally, we see in Figure 5.6 the ratio R tends to values larger than 3, i.e. 3.6 at 400 keV/u in our results³, while $R_{\times 3}^{2e}$ reaches only 3.2 at 400 keV/u. This significant difference is certainly due to the electron-electron exchange couplings related to the second target electron, present in the 3-electron calculations.

In summary, we observed an excellent agreement between recent experimental data and our three-electron calculations in the whole energy domain

²The results in Figure 5.5 are ratio for each total spin states and therefore independent of this scaling factors.

³Again, the ratio is measured by the Lanzhou team to be 3.3 already at 50 keV/u energy, the highest reachable one at their experimental facilities.

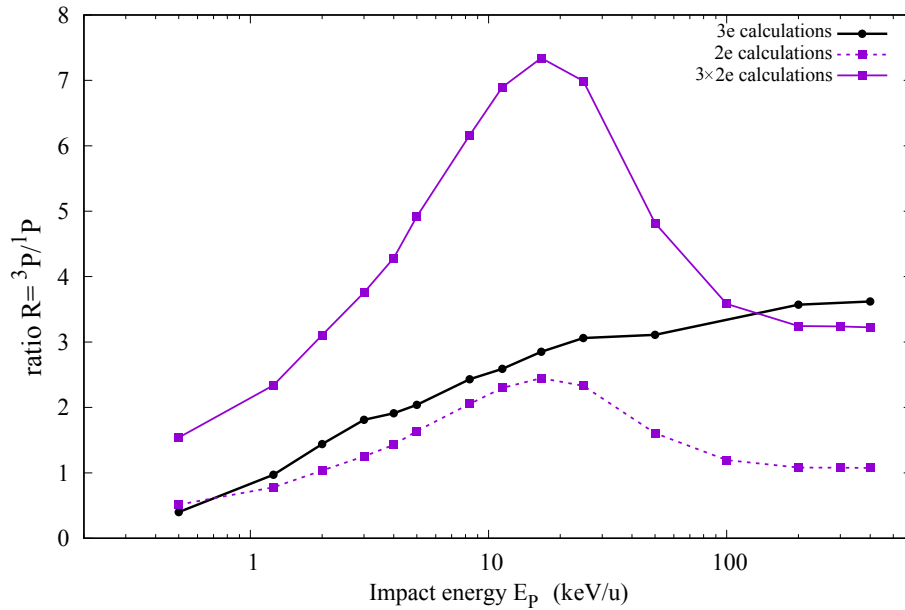


FIGURE 5.6: Ratio $R = {}^3P/{}^1P$ of the cross sections of production of $C^{2+}(1s^22s2p\ ^1,{}^3P)$ as function of energy. Black solid line: 3-electron calculations. Red lines: 2-electron calculations with eq. 5.3, including the scaling factor 3 (solid line) and without (dashed line).

considered while restricted two-electron calculations fail to reproduce the energy dependence of the ratio. One can conclude from these outcomes that, though the second target electron does not play a significant role in the collision, i.e. the processes involving the two target electrons are weak and have little interactions with the processes involving only one, modelling with a frozen electron cannot describe the relative strength of the single electron transfer to produce either singlet or triplet states of the same electronic configuration. In this restricted two-electron model the "loss" of total spin symmetry prevents the exact taking into account of the couplings (and notably the electron-electron exchange terms) between these states, which tends to give approximatively the spin statistics weight at high energies. This shows the extreme attention that must be paid to detailed results (as the ratio R) obtained in the frozen core approximation when it concerns equivalent electrons, as the two electrons of He in its ground state.

5.4 Conclusion

Single electron capture and transfer-excitation processes have been studied in C^{3+} - He collisions in a wide energy range, covering the low and intermediate

regime. The relative cross sections for production of $C^{2+}(1s^22l2l')$ states appear to be in excellent agreement with very recent experimental data while previous treatment failed to reproduce them.

Focusing on the two most dominant capture states $C^{2+}(1s^22s2p\ ^1,^3P)$, the ratio of cross sections $R = ^3P/^1P$ was found to increase from about 0.5 to about 3.6 for increasing energies, in near perfect agreement with the results from the Lanzhou team up to 50 keV/u, beyond which the experiment was not able to be carried out. Restricted 2-electron calculations fail to give similar results in the whole energy domain, showing the necessity of including the two electrons on He target and the failure of the frozen core approximation when focusing on highly detailed observables, as the ratio R .

Chapter 6

Conclusions and future work

In the present thesis, we have applied a non perturbative theoretical approach to describe multi-electronic processes occurring in ion-atom collisions at intermediate and high impact energies, from 100 eV/u to a few MeV/u. The treatment is semiclassical where the relative target-projectile motion is described by classical straight-line constant velocity trajectories. On the other hand, the electronic dynamics is treated quantum mechanically, by solving non perturbatively the time-dependent Schrödinger equation. In our group there have been developed several atomic orbital close-coupling codes to solve the TDSE to describe the dynamics of up to 4-active-electrons, within a full configuration interaction approach. Their use has been strongly focused on taking into account all kinds of electronic processes such as capture, excitation and ionisation and their combinations. This still remains very challenging for the theoretical and numerical description of collisions. They correspond to several thousand lines written in Fortran and are able to be applied for numerous collision systems.

The method has been applied to collisions mostly concerning light, highly charged projectiles for the needs of fundamental atomic physics and of related domains as plasma physics which require the knowledge of cross sections for various processes. Firstly in Chapter 3, we investigate Li^{2+} - H collisions. In this chapter the electron capture and electron excitation have been studied by using the two-active-electron SCAOCC presented in Chapter 2 in the energy range 0.1 - 250 keV/u. The present results come to a good agreement with previous available experimental data and theoretical calculations. Our study extends the calculations to impact energies as low as 0.1 keV/u, determining the dominant capture shell and sub-shell channels and validating or invalidating previous studies. Additionally, we have studied and analysed an anisotropy spin effect we have discovered in electron transfer at high impact energies: the production, by electron transfer, of $1snp\ ^3P$ is favoured compared to the 1P counterpart while this asymmetry is not observed for $1sns$ and $1snd$ configurations. For the needs

of understanding of this effect we developed a model based on Oppenheimer-Brinkman-Kramers approximation and we applied the close-coupling approach for three other two-electron related collision systems, i.e. He^+ , B^{4+} , C^{5+} - H. We found that this surprising effect was related to electron-electron exchange terms, introducing, at first order, a selection rule explaining the asymmetry for P states.

In Chapter 4 we focus on the formation of doubly excited $1s2l2l' \ ^{2,4}L$ states in collisions between He atoms and helium-like ions. We investigate three different projectiles, C^{4+} , O^{6+} , F^{7+} initially (prior the collisions), in their ground state or in metastable states $1s2s \ ^1S$ and $1s2s \ ^3S$, the latter two being considered for an experimental point of view, the ion beams delivered by accelerators being composed by ions in mixed states. The processes we mainly studied are the single electron capture and the transfer-excitation. We investigate further the bi-electronic process that is transfer-excitation for production of $1s2p^2 \ ^2D$ states from ground state projectile, trying to interpret and support mechanisms previously advocated to explain structures (peaks) observed in spectra as function of impact energy. The discussion we develop is of course based on the main, extensive, close-coupling calculations but also on restricted ones, with minimum numbers of states involved in the dynamics or neglecting the important couplings that are related to two-center electron-electron interaction. We support quantitatively the qualitative mechanism of resonant transfer-excitation, as inverse Auger effect, responsible of the high energy peak and interpret the low energy one as complex correlated mechanism, invalidating the intuitive representation of this process as a successive and independent excitation and transfer processes, named non resonant transfer-excitation in the literature.

Finally in Chapter 5, we have applied the close-coupling method for single electron capture process, focusing on the $\text{C}^{2+}(1s^22l2l' \ ^{2S+1}L)$ state-selective cross sections obtained in C^{3+} - He collisions for impact energy ranging from 0.5 to 400 keV/u. The calculated relative cross sections come in very good agreement with experimental data available while previous treatment failed to reproduce the experiment. We finally investigate the dependence of the relative strength of two transfer processes, producing triplet and singlet states of a given electronic configuration, $\text{C}^{2+}(1s^22s2p)$ and we obtain excellent agreement with very recent experimental data. Comparing our results, from the full three-electron approach with experiment and a standard, much less computationally expensive, two-electron approach, we invalidate the frozen core approximation, when concerning equivalent electrons, to predict detailed information on the outcomes of multi-electronic collision systems.

Considering the future of the present work, one can imagine several interesting developments. In the first term, the completion of some of the investigations presented in this thesis and which have been developed in the context of collaborations with experimentalists. Indeed there are still some challenges and question marks in the studies of Chapters 4 and 5. Further understanding requires to tackle other related collision systems and processes to generalise the conclusions drawn from the present studies. Experiments that always have the last word are very important in that context.

In a second time, an important effort must be made to optimise the code even better than it is currently. Indeed the calculations we have presented in this thesis represent several tens of thousands of hours of computer time (on 56 threads workstations). The optimisation of specific part of the code (with the use of GPU for example), together with the optimisation of the parallelisation strategy used in the present version, would be of great interest. A second and very important direction of optimisation corresponds to the actual description of the states involved in the dynamics: this may be done by coding the automatism of the optimisation of the GTO sets, to get better eigenstates and eigenvalues with smaller number of orbitals. Indeed the computer resources (CPU and memory) required to perform the calculations are approximatively scaled by a N^n law, where N is the number of GTO and n the number of active electrons, making quite awkward the extension of the code to systems with more than 4 electrons. The development of the code in that direction is challenging and imposes further research on new mathematical and programming techniques.

In the medium and long terms, the future of this theoretical development in atomic and molecular physics and physical chemistry, concerns the collision systems to be studied. Collision systems regarding mainly life science and clean energy production shall be of most interest. This requires the description of multi-electron multi-center neutral or ionised systems in interaction with strong and fast perturbations, also embedded in specific environments. Regarding life sciences, significant progress must be done in the description of electronic processes involving molecules, and particularly water molecule which constitutes more than 70% of the human body mass. Concerning fusion plasma devices, an interesting and new direction would be to incorporate a magnetic (but also electric) environment in which the collisions take place in these complex systems. In this context, but also for more general purposes concerning heavy atoms and ions, the inclusion of spin-orbit coupling would be challenging in ion-atom/molecule collision physics. But, finally, let us not forget that to be

able to deal with such complex systems, one shall need approximations and models. The development and the test of these latter on "simple" benchmarks collision systems are very interesting and are still original perspectives in fundamental research.

Appendices

A Gaussian Type Orbitals basis sets

A.1 Li^{2+} - H collision system

TABLE A.1: The GTO coefficients used to describe the electronic states of H

| B_1^H | | | B_2^H | | | B_3^H | | | B_4^H | | | B_5^H | | |
|---------|-----|-------------|---------|-----|-------------|---------|-----|-------------|---------|-----|-------------|---------|-----|-------------|
| i | l | α |
| 1 | 0 | 7.11700E-04 |
| 2 | 0 | 2.06393E-03 | 2 | 0 | 2.06393E-03 | 2 | 0 | 2.63329E-03 | 2 | 0 | 1.85042E-03 | 2 | 0 | 2.63329E-03 |
| 3 | 0 | 5.98539E-03 | 3 | 0 | 6.65783E-03 | 3 | 0 | 5.98539E-03 | 3 | 0 | 4.81109E-03 | 3 | 0 | 9.74317E-03 |
| 4 | 0 | 1.73576E-02 | 4 | 0 | 2.03634E-02 | 4 | 0 | 1.73576E-02 | 4 | 0 | 1.25088E-02 | 4 | 0 | 3.60497E-02 |
| 5 | 0 | 5.03371E-02 | 5 | 0 | 6.22829E-02 | 5 | 0 | 5.03371E-02 | 5 | 0 | 3.25230E-02 | 5 | 0 | 1.33384E-01 |
| 6 | 0 | 1.45977E-01 | 6 | 0 | 1.90496E-01 | 6 | 0 | 1.45977E-01 | 6 | 0 | 8.45597E-02 | 6 | 0 | 4.93521E-01 |
| 7 | 0 | 4.23335E-01 | 7 | 0 | 5.82645E-01 | 7 | 0 | 4.23335E-01 | 7 | 0 | 2.19855E-01 | 7 | 0 | 1.82603E+00 |
| 8 | 0 | 1.22767E+00 | 8 | 0 | 1.78206E+00 | 8 | 0 | 1.22767E+00 | 8 | 0 | 5.71624E-01 | 8 | 0 | 6.75630E+00 |
| 9 | 0 | 3.56025E+00 | 9 | 0 | 5.45055E+00 | 9 | 0 | 3.56025E+00 | 9 | 0 | 1.48622E+00 | 9 | 0 | 2.49983E+01 |
| 10 | 0 | 1.03247E+01 | 10 | 0 | 1.66709E+01 | 10 | 0 | 1.03247E+01 | 10 | 0 | 3.86418E+00 | 10 | 0 | 9.24938E+01 |
| 11 | 0 | 2.99417E+01 | 11 | 0 | 5.09890E+01 | 11 | 0 | 2.99417E+01 | 11 | 0 | 1.00469E+01 | | | |
| 12 | 0 | 8.68310E+01 | | | | 12 | 0 | 8.68310E+01 | 12 | 0 | 2.61218E+01 | | | |
| | | | | | | | | | 13 | 0 | 6.79168E+01 | | | |
| | | | | | | | | | 14 | 0 | 1.76584E+02 | | | |
| 1 | 1 | 1.04700E-03 |
| 2 | 1 | 3.24570E-03 | 2 | 1 | 3.24570E-03 | 2 | 1 | 3.24570E-03 | 2 | 1 | 5.19621E-03 | 2 | 1 | 5.19621E-03 |
| 3 | 1 | 1.00617E-02 | 3 | 1 | 1.00617E-02 | 3 | 1 | 1.00617E-02 | 3 | 1 | 2.57886E-02 | 3 | 1 | 2.57886E-02 |
| 4 | 1 | 3.11912E-02 | 4 | 1 | 3.11912E-02 | 4 | 1 | 3.11912E-02 | 4 | 1 | 1.27988E-01 | 4 | 1 | 1.27988E-01 |
| 5 | 1 | 9.66927E-02 | 5 | 1 | 9.66927E-02 | 5 | 1 | 9.66927E-02 | 5 | 1 | 6.35197E-01 | 5 | 1 | 6.35197E-01 |
| 6 | 1 | 2.99747E-01 | 6 | 1 | 2.99747E-01 | 6 | 1 | 2.99747E-01 | 6 | 1 | 3.15245E+00 | 6 | 1 | 3.15245E+00 |
| 7 | 1 | 9.29216E-01 | 7 | 1 | 9.29216E-01 | 7 | 1 | 9.29216E-01 | | | | | | |
| 8 | 1 | 2.88057E+00 | 8 | 1 | 2.88057E+00 | 8 | 1 | 2.88057E+00 | | | | | | |
| 1 | 2 | 1.17500E-02 | 1 | 2 | 1.17500E-02 | | | | 1 | 2 | 1.17500E-02 | | | |
| 2 | 2 | 3.52500E-02 | 2 | 2 | 6.10548E-02 | | | | 2 | 2 | 2.72722E-02 | | | |
| 3 | 2 | 1.05760E-01 | | | | | | | 3 | 2 | 6.32998E-02 | | | |
| 4 | 2 | 3.17250E-01 | | | | | | | 4 | 2 | 1.46921E-01 | | | |
| | | | | | | | | | 5 | 2 | 3.41010E-01 | | | |
| | | | | | | | | | 6 | 2 | 7.91497E-01 | | | |

TABLE A.2: The GTO coefficients used to describe the electronic states of Li^+ and Li^{2+}

| B_1^{Li} | | | B_2^{Li} | | | B_3^{Li} | | | B_4^{Li} | | | B_5^{Li} | | |
|------------|-----|-------------|------------|-----|-------------|------------|-----|-------------|------------|-----|-------------|------------|-----|-------------|
| i | l | α |
| 1 | 0 | 6.40530E-03 |
| 2 | 0 | 1.85754E-02 | 2 | 0 | 1.95910E-02 | 2 | 0 | 1.85754E-02 | 2 | 0 | 1.66538E-02 | 2 | 0 | 2.36996E-02 |
| 3 | 0 | 5.38686E-02 | 3 | 0 | 5.99205E-02 | 3 | 0 | 5.38686E-02 | 3 | 0 | 4.32998E-02 | 3 | 0 | 8.76886E-02 |
| 4 | 0 | 1.56219E-01 | 4 | 0 | 1.83271E-01 | 4 | 0 | 1.56219E-01 | 4 | 0 | 1.12580E-01 | 4 | 0 | 3.24448E-01 |
| 5 | 0 | 4.53035E-01 | 5 | 0 | 5.60546E-01 | 5 | 0 | 4.53035E-01 | 5 | 0 | 2.92707E-01 | 5 | 0 | 1.20046E+00 |
| 6 | 0 | 1.31380E+00 | 6 | 0 | 1.71447E+00 | 6 | 0 | 1.31380E+00 | 6 | 0 | 7.61038E-01 | 6 | 0 | 4.44169E+00 |
| 7 | 0 | 3.81002E+00 | 7 | 0 | 5.24381E+00 | 7 | 0 | 3.81002E+00 | 7 | 0 | 1.97870E+00 | 7 | 0 | 1.64342E+01 |
| 8 | 0 | 1.22767E+00 | 8 | 0 | 1.60385E+01 | 8 | 0 | 1.22767E+00 | 8 | 0 | 5.14461E+00 | 8 | 0 | 6.08067E+01 |
| 9 | 0 | 3.56025E+00 | 9 | 0 | 4.90549E+01 | 9 | 0 | 3.56025E+00 | 9 | 0 | 1.33760E+01 | 9 | 0 | 2.24985E+02 |
| 10 | 0 | 9.29227E+01 | 10 | 0 | 1.50038E+02 | 10 | 0 | 9.29227E+01 | 10 | 0 | 3.47776E+01 | 10 | 0 | 8.32444E+02 |
| 11 | 0 | 2.69476E+02 | 11 | 0 | 4.58901E+02 | 11 | 0 | 2.69476E+02 | 11 | 0 | 9.04217E+01 | | | |
| 12 | 0 | 7.81480E+02 | | | | 12 | 0 | 7.81480E+02 | 12 | 0 | 2.35096E+02 | | | |
| | | | | | | | | | 13 | 0 | 6.11252E+02 | | | |
| | | | | | | | | | 14 | 0 | 1.58925E+03 | | | |
| 1 | 1 | 9.42300E-03 |
| 2 | 1 | 2.92113E-02 | 2 | 1 | 2.92113E-02 | 2 | 1 | 2.92113E-02 | 2 | 1 | 4.67659E-02 | 2 | 1 | 4.67659E-02 |
| 3 | 1 | 9.05550E-02 | 3 | 1 | 9.05550E-02 | 3 | 1 | 9.05550E-02 | 3 | 1 | 2.32097E-01 | 3 | 1 | 2.32097E-01 |
| 4 | 1 | 2.80721E-01 | 4 | 1 | 2.80721E-01 | 4 | 1 | 2.80721E-01 | 4 | 1 | 1.15189E+00 | 4 | 1 | 1.15189E+00 |
| 5 | 1 | 8.70234E-01 | 5 | 1 | 8.70234E-01 | 5 | 1 | 8.70234E-01 | 5 | 1 | 5.71677E+00 | 5 | 1 | 5.71677E+00 |
| 6 | 1 | 2.69771E+00 | 6 | 1 | 2.69771E+00 | 6 | 1 | 2.69771E+00 | 6 | 1 | 2.83721E+01 | 6 | 1 | 2.83721E+01 |
| 7 | 1 | 8.36292E+00 | 7 | 1 | 8.36292E+00 | 7 | 1 | 8.36292E+00 | | | | | | |
| 8 | 1 | 2.59251E+01 | 8 | 1 | 2.59251E+01 | 8 | 1 | 2.59251E+01 | | | | | | |
| 1 | 2 | 1.05750E-01 | 1 | 2 | 1.05750E-01 | | | | 1 | 2 | 1.05750E-01 | | | |
| 2 | 2 | 3.17250E-01 | 2 | 2 | 5.49493E-01 | | | | 2 | 2 | 2.45450E-01 | | | |
| 3 | 2 | 9.51750E-01 | | | | | | | 3 | 2 | 5.69699E-01 | | | |
| 4 | 2 | 2.85525E+00 | | | | | | | 4 | 2 | 1.32229E+00 | | | |
| | | | | | | | | | 5 | 2 | 3.06909E+00 | | | |
| | | | | | | | | | 6 | 2 | 7.12348E+00 | | | |

A.2 Z^{Z-1} - H collision systems (spin effect study)

TABLE A.3: The GTO coefficients used to describe the electronic states of He, He⁺, Li⁺, Li²⁺, B³⁺, B⁴⁺ and C⁴⁺, C⁵⁺

| B_P^{He} | | | B_P^{Li} | | | B_P^{Be} | | | B_P^C | | | B_P^H | | |
|------------|----------|-------------|------------|----------|-------------|------------|----------|-------------|----------|----------|-------------|----------|----------|-------------|
| <i>i</i> | <i>l</i> | α | <i>i</i> | <i>l</i> | α | <i>i</i> | <i>l</i> | α | <i>i</i> | <i>l</i> | α | <i>i</i> | <i>l</i> | α |
| 1 | 0 | 1.88000E-02 | 1 | 0 | 1.88000E-02 | 1 | 0 | 1.17500E-01 | 1 | 0 | 1.69200E-01 | 1 | 0 | 5.00000E-03 |
| 2 | 0 | 3.12586E-02 | 2 | 0 | 3.12587E-02 | 2 | 0 | 1.95367E-01 | 2 | 0 | 2.81328E-01 | 2 | 0 | 1.20549E-02 |
| 3 | 0 | 8.28564E-02 | 3 | 0 | 8.28564E-02 | 3 | 0 | 5.17852E-01 | 3 | 0 | 7.45707E-01 | 3 | 0 | 2.90640E-02 |
| 4 | 0 | 3.30479E-01 | 4 | 0 | 3.30480E-01 | 4 | 0 | 2.06549E+00 | 4 | 0 | 2.97431E+00 | 4 | 0 | 7.00726E-02 |
| 5 | 0 | 8.57938E-01 | 5 | 0 | 8.57938E-01 | 5 | 0 | 5.36211E+00 | 5 | 0 | 7.72144E+00 | 5 | 0 | 1.68943E-01 |
| 6 | 0 | 2.22725E+00 | 6 | 0 | 2.22725E+00 | 6 | 0 | 1.39203E+01 | 6 | 0 | 2.00452E+01 | 6 | 0 | 4.07318E-01 |
| 7 | 0 | 5.78204E+00 | 7 | 0 | 5.78204E+00 | 7 | 0 | 3.61377E+01 | 7 | 0 | 5.20383E+01 | 7 | 0 | 9.82033E-01 |
| 8 | 0 | 1.50104E+01 | 8 | 0 | 1.50104E+01 | 8 | 0 | 9.38152E+01 | 8 | 0 | 1.35094E+02 | 8 | 0 | 2.36766E+00 |
| 9 | 0 | 3.89678E+01 | 9 | 0 | 3.89678E+01 | 9 | 0 | 2.43549E+02 | 9 | 0 | 3.50710E+02 | 9 | 0 | 5.70837E+00 |
| 10 | 0 | 1.01162E+02 | 10 | 0 | 1.01162E+02 | 10 | 0 | 6.32263E+02 | 10 | 0 | 9.10459E+02 | 10 | 0 | 1.37628E+01 |
| 11 | 0 | 3.95955E+02 | 11 | 0 | 3.95955E+02 | 11 | 0 | 2.47472E+03 | 11 | 0 | 3.56359E+03 | 11 | 0 | 3.31816E+01 |
| 12 | 0 | 6.81778E+02 | 12 | 0 | 6.81778E+02 | 12 | 0 | 4.26111E+03 | 12 | 0 | 6.13600E+03 | 12 | 0 | 8.00000E+01 |
| | | | | | | | | | | | | | | |
| 1 | 1 | 1.89778E-02 | 1 | 1 | 1.89778E-02 | 1 | 1 | 1.18611E-01 | 1 | 1 | 1.70800E-01 | 1 | 1 | 8.00000E-03 |
| 2 | 1 | 4.71633E-02 | 2 | 1 | 4.71633E-02 | 2 | 1 | 2.94771E-01 | 2 | 1 | 4.24470E-01 | 2 | 1 | 2.00792E-02 |
| 3 | 1 | 1.17210E-01 | 3 | 1 | 1.17210E-01 | 3 | 1 | 7.32560E-01 | 3 | 1 | 1.05489E+00 | 3 | 1 | 5.03968E-01 |
| 4 | 1 | 2.91288E-01 | 4 | 1 | 2.91288E-01 | 4 | 1 | 1.82055E+00 | 4 | 1 | 2.62159E+00 | 4 | 1 | 1.26491E-01 |
| 5 | 1 | 7.23904E-01 | 5 | 1 | 7.23904E-01 | 5 | 1 | 4.52440E+00 | 5 | 1 | 6.51513E+00 | 5 | 1 | 3.17480E-01 |
| 6 | 1 | 1.79904E+00 | 6 | 1 | 1.79904E+00 | 6 | 1 | 1.12440E+01 | 6 | 1 | 1.61913E+01 | 6 | 1 | 2.00000E+00 |
| 7 | 1 | 4.47094E+00 | 7 | 1 | 4.47094E+00 | 7 | 1 | 2.79433E+01 | 7 | 1 | 4.02384E+01 | | | |
| 8 | 1 | 1.11111E+01 | 8 | 1 | 1.11111E+01 | 8 | 1 | 6.94444E+01 | 8 | 1 | 1.00000E+02 | | | |
| | | | | | | | | | | | | | | |
| 1 | 2 | 4.70000E-02 | 1 | 2 | 4.70000E-02 | 1 | 2 | 2.93750E-01 | 1 | 2 | 4.23000E-01 | 1 | 2 | 3.52500E-02 |
| 2 | 2 | 1.41000E-01 | 2 | 2 | 1.41000E-01 | 2 | 2 | 8.81250E-01 | 2 | 2 | 1.26900E+00 | 2 | 2 | 1.05750E-01 |
| 3 | 2 | 4.23000E-01 | 3 | 2 | 4.22300E-01 | 3 | 2 | 2.64375E+00 | 3 | 2 | 3.80700E+00 | 3 | 2 | 3.17249E-01 |
| 4 | 2 | 1.26900E+00 | 4 | 2 | 1.26900E+00 | 4 | 2 | 7.93125E+00 | 4 | 2 | 1.14201E+01 | | | |

A.3 C⁴⁺ - He collision system

TABLE A.4: The GTO coefficients used to describe the electronic states of C³⁺ and C⁴⁺

| B_1^C | | |
|---------|-----|-------------|
| i | l | α |
| 1 | 0 | 0.55000E-01 |
| 2 | 0 | 0.12981E+00 |
| 3 | 0 | 0.30638E+00 |
| 4 | 0 | 0.72312E+00 |
| 5 | 0 | 0.17067E+01 |
| 6 | 0 | 0.40282E+01 |
| 7 | 0 | 0.95074E+01 |
| 8 | 0 | 0.22440E+02 |
| 9 | 0 | 0.52962E+02 |
| 10 | 0 | 0.12500E+03 |
| | | |
| 1 | 1 | 0.26000E+00 |
| 2 | 1 | 0.75000E+00 |
| 3 | 1 | 0.24495E+01 |
| 4 | 1 | 0.80000E+01 |

TABLE A.5: The GTO coefficients used to describe the electronic states of He and He⁺

| B_1^{He} | | |
|------------|-----|-------------|
| i | l | α |
| 1 | 0 | 1.22500E-02 |
| 2 | 0 | 2.90331E-02 |
| 3 | 0 | 1.16266E-01 |
| 4 | 0 | 4.65591E-01 |
| 5 | 0 | 1.86449E+00 |
| 6 | 0 | 7.46648E+00 |
| 7 | 0 | 2.99000E+01 |

A.4 F^{7+} - He collision system

TABLE A.6: The GTO coefficients used to describe the electronic states of F^{6+} and F^{7+}

| i | l | B_1^F | |
|-----|-----|-------------|--|
| | | α | |
| 1 | 0 | 1.68750E-01 | |
| 2 | 0 | 4.21887E-01 | |
| 3 | 0 | 9.95739E-01 | |
| 4 | 0 | 2.35015E+00 | |
| 5 | 0 | 5.54683E+00 | |
| 6 | 0 | 1.30917E+01 | |
| 7 | 0 | 3.08990E+01 | |
| 8 | 0 | 7.29279E+01 | |
| 9 | 0 | 1.72125E+02 | |
| 10 | 0 | 9.75000E+02 | |
| | | | |
| 1 | 1 | 8.45000E-01 | |
| 2 | 1 | 2.43750E+00 | |
| 3 | 1 | 7.96084E+00 | |
| 4 | 1 | 3.12000E+01 | |

TABLE A.7: The GTO coefficients used to describe the electronic states of He and He^+

| i | l | B_1^{He} | |
|-----|-----|-------------|--|
| | | α | |
| 1 | 0 | 1.22500E-02 | |
| 2 | 0 | 2.90331E-02 | |
| 3 | 0 | 1.16266E-01 | |
| 4 | 0 | 4.65591E-01 | |
| 5 | 0 | 1.86449E+00 | |
| 6 | 0 | 7.46648E+00 | |
| 7 | 0 | 2.99000E+01 | |

A.5 O⁶⁺ - He collision system

TABLE A.8: The GTO coefficients used to describe the electronic states of O⁵⁺ and O⁶⁺

| B_1^O | | |
|---------|-----|-------------|
| i | l | α |
| 1 | 0 | 3.00000E-01 |
| 2 | 0 | 7.50021E-01 |
| 3 | 0 | 1.77020E+00 |
| 4 | 0 | 4.17804E+00 |
| 5 | 0 | 9.86103E+00 |
| 6 | 0 | 2.32741E+01 |
| 7 | 0 | 5.49315E+01 |
| 8 | 0 | 1.29650E+02 |
| 9 | 0 | 3.05600E+02 |
| 10 | 0 | 1.73333E+03 |
| | | |
| 1 | 1 | 7.22222E-01 |
| 2 | 1 | 2.08333E+00 |
| 3 | 1 | 6.80414E+00 |
| 4 | 1 | 2.66667E+01 |

TABLE A.9: The GTO coefficients used to describe the electronic states of He and He⁺

| B_1^{He} | | |
|------------|-----|-------------|
| i | l | α |
| 1 | 0 | 1.22500E-02 |
| 2 | 0 | 2.90331E-02 |
| 3 | 0 | 1.16266E-01 |
| 4 | 0 | 4.65591E-01 |
| 5 | 0 | 1.86449E+00 |
| 6 | 0 | 7.46648E+00 |
| 7 | 0 | 2.99000E+01 |

A.6 C³⁺ - He collision system

TABLE A.10: The GTO coefficients used to describe the electronic states of C²⁺ and C³⁺

| $B_{C_1}^{3e}$ | | |
|----------------|-----|-------------|
| i | l | α |
| 1 | 0 | 5.55500E-02 |
| 2 | 0 | 1.78951E-01 |
| 3 | 0 | 5.76478E-01 |
| 4 | 0 | 1.85709E+00 |
| 5 | 0 | 5.98249E+00 |
| 6 | 0 | 1.92722E+01 |
| 7 | 0 | 6.20841E+01 |
| 8 | 0 | 2.00000E+02 |
| | | |
| 1 | 1 | 2.70000E-01 |
| 2 | 1 | 9.00000E-01 |
| 3 | 1 | 3.00000E+00 |
| 4 | 1 | 1.00000E+10 |
| | | |
| 1 | 2 | 2.05000E-01 |
| 2 | 2 | 6.95000E-01 |

TABLE A.11: The GTO coefficients used to describe the electronic states of He and He⁺

| $B_{He_1}^{3e}$ | | |
|-----------------|-----|-------------|
| i | l | α |
| 1 | 0 | 2.39000E-01 |
| 2 | 0 | 8.85323E-01 |
| 3 | 0 | 3.27948E+00 |
| 4 | 0 | 1.21481E+01 |
| 5 | 0 | 4.50000E+01 |
| | | |
| 1 | 1 | 3.45000E-02 |
| 2 | 1 | 2.45713E-01 |
| 3 | 1 | 1.75000E+00 |

Bibliography

- [1] D. R. Bates and B. L. Moiseiwitsch. **Inelastic Heavy Particle Collisions Involving the Crossing of Potential Energy Curves I: Charge transfer from H atoms to Be^{2+} , Si^{2+} and Mg^{2+} ions.** *Proceedings of the Physical Society. Section A*, 67(9):805–812, September 1954.
- [2] A. Dalgarno. **Inelastic Heavy-Particle Collisions Involving the Crossing of Potential Energy Curves II: Charge Transfer from H-atoms to Al^{3+} , B^{2+} , Li^{2+} and Al^{2+} .** *Proceedings of the Physical Society. Section A*, 67(11):1010–1017, November 1954.
- [3] M. Wardle and F. Yusef-Zadeh. **Supernova Remnant OH Masers: Signposts of Cosmic Collision.** *Science*, 296(5577):2350–2354, June 2002.
- [4] H. Massey. **Atomic and molecular collisions.** 1979.
- [5] A. H. Gabriel and H. E. Mason. **Solar physics.** 1:345–397, 1982.
- [6] H. S. W. Massey. **Applied Atomic Collision Physics: Atmospheric Physics and Chemistry.** Elsevier, December 2012.
- [7] R. C. Nichols Jr, R. H. Henderson, S. Huh, S. Flampouri, Z. Li, A. A. Bajwa, H. J. D’Agostino, D. C. Pham, N. P. Mendenhall, and B. S. Hoppe. **Proton therapy for lung cancer.** *Thoracic Cancer*, 3(2):109–116, 2012.
- [8] W. H. Barkas. **Particle behavior and emulsion applications,** 1973.
- [9] D. E. Post. **The Role of Atomic Collisions In Fusion.** In F. Brouillard and J. W. McGowan, editors, *Physics of Ion-Ion and Electron-Ion Collisions*, pages 37–99. Springer US, Boston, MA, 1983.
- [10] R. K. Janev. **ATOMIC COLLISIONS IN FUSION PLASMAS.** *Le Journal de Physique Colloques*, 50(C1):C1–421–C1–443, January 1989.
- [11] J. Lindl and B. Hammel. **Recent advances in indirect drive icf target physics.** In *20th IAEA Fusion Energy Conference*, 2004.

- [12] M. S. Tillack, A. D. Turnbull, C. E. Kessel, N. Asakura, A. M. Garofalo, C. Holland, F. Koch, Ch. Linsmeier, S. Lisgo, R. Maingi, R. Majeski, J. Menard, F. Najmabadi, R. Nygren, T. D. Rognlien, D. D. Ryutov, R. D. Stambaugh, P. C. Stangeby and D. P. Stotler. **Summary of the ARIES Town Meeting: ‘Edge Plasma Physics and Plasma Material Interactions in the Fusion Power Plant Regime’**. *Nuclear Fusion*, 53(2):027003, February 2013.
- [13] G. McCracken and P. Stott. **Chapter 7 - Inertial-Confinement Fusion**. In Garry McCracken and Peter Stott, editors, *Fusion (Second Edition)*, pages 67–81. Academic Press, Boston, January 2013.
- [14] M. Barat. **The Quasi-Molecular Model in Heavy Particle Collisions**. In F. J. Wuilleumier, editor, *Photoionization and Other Probes of Many - Electron Interactions*, NATO Advanced Study Institutes Series, pages 229–253. Springer US, Boston, MA, 1976.
- [15] J. B. Delos. **Theory of electronic transitions in slow atomic collisions**. *Reviews of Modern Physics*, 53(2):287–357, April 1981.
- [16] L. F. Errea, F. Guzmán, L. Méndez, B. Pons and A. Riera. **Ab initio calculation of charge-transfer and excitation cross sections in $\text{Li}^+ + \text{H}(1s)$ collisions**. *Phys. Rev. A*, 77:012706, Jan 2008.
- [17] D. S. F. Crothers and M. McCartney. **ION — a program to evaluate cross-sections for ionisation in ion-atom collisions**. *Computer Physics Communications*, 72(2):288–294, November 1992.
- [18] P. D. Fainstein, V. H. Ponce and R. D. Rivarola. **Single-electron ionisation of helium by anti-proton and proton impact**. *Journal of Physics B: Atomic, Molecular and Optical Physics*, 22(19):L559–L563, October 1989.
- [19] R. Abrines and I. C. Percival. **Classical theory of charge transfer and ionization of hydrogen atoms by protons**. *Proceedings of the Physical Society*, 88(4):861–872, August 1966.
- [20] M. Schulz, R. Moshhammer, W. Schmitt, H. Kollmus, R. Mann, S. Hagmann, R. E. Olson and J. Ullrich. **Correlated three-electron continuum states in triple ionization by fast heavy-ion impact**. *Physical Review A*, 61(2):022703, January 2000.
- [21] J. P. Hansen, A. Dubois and S. E. Nielsen. **Orientation and alignment in $\text{H}^+ - \text{H}$ collisions**. *Physical Review A*, 44(9):6130–6132, November 1991.

- [22] J. P. Hansen and A. Dubois. **Procedures for analytical and numerical calculation of Coulombic one- and two-centre integrals.** *Computer Physics Communications*, 67(3):456–464, January 1992.
- [23] J. Caillat, A. Dubois and J. P. Hansen. **On the discrepancies of the calculated $C^{5+}(n = 5)$ capture cross sections in C^{6+} -H collisions.** *Journal of Physics B: Atomic, Molecular and Optical Physics*, 33(20):L715–L720, September 2000.
- [24] J. Wang, J. P. Hansen and A. Dubois. **Neutralization and charge transfer in H^+ - H^- and H-H collisions.** *Journal of Physics B: Atomic, Molecular and Optical Physics*, 33(2):241–249, January 2000.
- [25] N. Sisourat, I. Pilskog and A. Dubois. **Nonperturbative treatment of multielectron processes in ion-molecule scattering: Application to He^{2+} - H_2 collisions.** *Physical Review A*, 84(5):052722, November 2011.
- [26] A. Ibaaz, R. E. Hernandez, A. Dubois and N. Sisourat. **Excitation into high-lying states in Li^{+3} -H collisions.** *Journal of Physics B: Atomic, Molecular and Optical Physics*, 49(8):085202, April 2016.
- [27] J. W. Gao, Y. Wu, N. Sisourat, J. G. Wang and A. Dubois. **Single- and double-electron transfer in low- and intermediate-energy C^{4+} +He collisions.** *Physical Review A*, 96(5):052703, November 2017.
- [28] J. W. Gao, Y. Wu, J. G. Wang, N. Sisourat and A. Dubois. **State-selective electron transfer He^+ +He collisions at intermediate energies.** *Physical Review A*, 97(5):052709, May 2018.
- [29] I. Madesis, A. Laoutaris, E. P. Benis, A. Lagoyannis, M. Axiotis and T. J. M. Zouros. **Zero-degree Auger Projectile Electron Spectroscopy of Li-like Ions obtained in Collisions of $1s2s$ 3S He-like Ions with Gaseous Targets.** *HNPS Advances in Nuclear Physics*, 24(0):1–15, April 2019.
- [30] D. L. Guo, J. W. Gao, S. F. Zhang, X. L. Zhu, Y. Gao, D. M. Zhao, R. T. Zhang, Y. Wu, J. G. Wang, A. Dubois, X. Ma. **State-selective single-electron capture in intermediate-energy C^{4+} + He collisions.** *Physical Review A*, 103(3):032827, March 2021.
- [31] C. J. Joachain. *Quantum collision theory*. Netherlands, 1975.

- [32] W. Fritsch and C. D. Lin. The semiclassical close-coupling description of atomic collisions: Recent developments and results. *Physics Reports*, 202(1):1–97, April 1991.
- [33] B. H. Bransden and M. R. C. McDowell. *Charge Exchange and the Theory of Ion-Atom Collisions*. International Series of Monographs on Physics. Oxford University Press, Oxford, New York, May 1992.
- [34] R. McCarroll and D. R. Bates. Resonance charge transfer between H(1s) and H⁺ calculated by means of an approximation based on an expansion in atomic eigenfunctions. *Proceedings of the Royal Society of London. Series A. Mathematical and Physical Sciences*, 264(1319):547–557, December 1961.
- [35] W. Fritsch and C. D. Lin. Atomic-Orbital Expansions for Describing Charge Transfer in Slow Ion-Atom Collisions. *Physica Scripta*, T3:241–243, January 1983.
- [36] R. McCarroll. Charge Exchange and Ionization in Ion-Atom Collisions. In Franco A. Gianturco, editor, *Atomic and Molecular Collision Theory*, pages 165–231. Springer US, Boston, MA, 1982.
- [37] R. Y. Cusson, R. K. Smith and J. A. Maruhn. Time-Dependent Hartree-Fock Calculation of the Reaction $^{16}\text{O} + ^{16}\text{O}$ in Three Dimensions. *Physical Review Letters*, 36(20):1166–1169, May 1976.
- [38] R. Y. Cusson and J. Maruhn. Dynamics of $^{12}\text{C} + ^{12}\text{C}$ in a realistic time-dependent, Hartree-Fock model. *Physics Letters B*, 62(2):134–138, May 1976.
- [39] K. T. R. Davies, V. Maruhn-Rezwani, S. E. Koonin and J. W. Negele. Test of the Time-Dependent Mean-Field Theory in Kr-induced Strongly Damped Collisions. *Physical Review Letters*, 41(9):632–635, August 1978.
- [40] S. E. Koonin, K. T. R. Davies, V. Maruhn-Rezwani, H. Feldmeier, S. J. Krieger, and J. W. Negele. Time-dependent Hartree-Fock calculations for $^{16}\text{O} + ^{16}\text{O}$ and $^{40}\text{Ca} + ^{40}\text{Ca}$ reactions. *Physical Review C*, 15(4):1359–1374, April 1977.
- [41] C. Bottcher. Accurate Quantal Studies of Ion-Atom Collisions Using Finite-Element Techniques. *Physical Review Letters*, 48(2):85–88, January 1982.

- [42] V. Maruhn-Rezwani, N. Grün and W. Scheid. **Numerical Solution of the Time-Dependent Schrödinger Equation and Application to H^+ -H.** *Physical Review Letters*, 43(7):512–515, August 1979.
- [43] M. Foster, J. Colgan and M. S. Pindzola. **Fully correlated electronic dynamics for antiproton impact ionization of helium.** *Phys. Rev. Lett.*, 100:033201, Jan 2008.
- [44] M. E. Riley and A. B. Ritchie. **Excitation and ionization in H(1s)-H(1s) collisions: II. Inclusion of electron exchange.** *Journal of Physics B: Atomic, Molecular and Optical Physics*, 33(22):5177–5190, nov 2000.
- [45] L. Sælen, T. Birkeland, N. Sisourat, A. Dubois and J. P. Hansen. **Nonperturbative treatment of single ionization of H_2 by fast highly-charged-ion impact.** *Phys. Rev. A*, 81:022718, Feb 2010.
- [46] M. S. Pindzola, M. Fogle and P. C. Stancil. **Line ratios for x-ray emission in O^{8+} collisions with H and He atoms.** *Journal of Physics B: Atomic, Molecular and Optical Physics*, 51(6):065204, mar 2018.
- [47] J. P. Hansen and A. Dubois. **Excitation in H(1s) - H(1s) collisions.** *Journal of Physics B: Atomic, Molecular and Optical Physics*, 31(20):L861–L865, 1998.
- [48] D.R. Bates and R. McCarroll. **Electron capture in slow collisions.** *Proceedings of the Royal Society of London. Series A. Mathematical and Physical Sciences*, 245(1241):175–183, June 1958.
- [49] L. F. Shampine and M. K. Gordon. *Computer solution of ordinary differential equations: the initial value problem.* W.H. Freeman, San Francisco, 1975. OCLC: 1093545.
- [50] J. Caillat. *Etude théorique des processus électroniques au cours de collisions ion-atome et ion-molécule.* These de doctorat, Paris 6, January 2003.
- [51] J. Caillat, N. Sisourat, A. Dubois, I. Sundvor and J. P. Hansen. **Orientation effects in He^{2+} - H_2^+ collisions at intermediate collision energies.** *Physical Review A*, 73(1):014701, January 2006.
- [52] I. Rabadán, L. Méndez, J. W. Gao, Y. Wu and J. G. Wang. **Ab initio calculation of electron-capture cross sections in H^+ +BeH collisions.** *Physical Review A*, 96(3):032714, September 2017.

- [53] L. F. Errea, J. D. Gorfinkiel, A. Macías, L. Méndez and A. Riera. **Implementation of the sudden approximation eikonal method in ion - diatom collisions.** *Journal of Physics B: Atomic, Molecular and Optical Physics*, 30(17):3855–3872, September 1997.
- [54] S. E. Nielsen, J. P. Hansen and A. Dubois. **Propensity rules for orientation in singly-charged ion-atom collisions.** *Journal of Physics B: Atomic, Molecular and Optical Physics*, 23(15):2595–2612, August 1990.
- [55] N. Sisourat. *Etude théorique de phénomènes d'interférences au cours de collisions atomiques et moléculaires.* These de doctorat, Paris 6, January 2008.
- [56] J. Gao. *Two-electron processes and correlation effects in ion-atom collisions: a close-coupling approach at intermediate energies.* These de doctorat, Sorbonne université, May 2019.
- [57] G. Labaigt. *Etude théorique de processus multi-électroniques au cours de collisions atomiques et moléculaires.* These de doctorat, Paris 6, September 2014.
- [58] S. F. Boys and A. C. Egerton. **Electronic wave functions - I. A general method of calculation for the stationary states of any molecular system.** *Proceedings of the Royal Society of London. Series A. Mathematical and Physical Sciences*, 200(1063):542–554, February 1950.
- [59] C. M. Reeves and M. C. Harrison. **Use of Gaussian Functions in the Calculation of Wavefunctions for Small Molecules. II. The Ammonia Molecule.** *The Journal of Chemical Physics*, 39(1):11–17, July 1963.
- [60] R. C. Raffanetti. **Even-tempered atomic orbitals. II. Atomic SCF wavefunctions in terms of even-tempered exponential bases.** *The Journal of Chemical Physics*, 59(11):5936–5949, December 1973.
- [61] Nicolas Sisourat and Alain Dubois. *7. Semiclassical close-coupling approaches*, pages 157–178. De Gruyter, 2019.
- [62] J. Caillat, A. Dubois and J. P. Hansen. **Semiclassical Close-Coupling Description of Electron Transfer in Multicharged Ion-Atom Collisions.** In Jean Maruani, Christian Minot, Roy McWeeny, Yves G. Smeyers and Stephen Wilson, editors, *New Trends in Quantum Systems in Chemistry and Physics: Volume 2 Advanced Problems and Complex Systems Paris*,

- France, 1999*, Progress in Theoretical Chemistry and Physics, pages 121–131. Springer Netherlands, Dordrecht, 2002.
- [63] J. Caillat, A. Dubois, I. Sundvor and J.-P. Hansen. **Classical and semi-classical calculations of electron transfer cross sections in keV-energy ion-molecule collisions.** *Physical Review A*, 70(3):032715, September 2004.
- [64] M. M. Basko, A. J. Kemp and J. M. Vehn. **Ignition conditions for magnetized target fusion in cylindrical geometry.** *Nuclear Fusion*, 40(1):59–68, January 2000.
- [65] J. Lindl. **Development of the indirect-drive approach to inertial confinement fusion and the target physics basis for ignition and gain.** *Physics of Plasmas*, 2(11):3933–4024, November 1995.
- [66] R. J. Fonck, D. S. Darrow and K. P. Jaehnig. **Determination of plasma-ion velocity distribution via charge-exchange recombination spectroscopy.** *Physical Review A*, 29(6):3288–3309, June 1984.
- [67] R. C. Isler. **An overview of charge-exchange spectroscopy as a plasma diagnostic.** *Plasma Physics and Controlled Fusion*, 36(2):171–208, February 1994.
- [68] M. G. von Hellermann, G. Bertschinger, W. Biel, C. Giroud, R. Jaspers, C. Jupen, O. Marchuk, M. O. Mullane, H. P. Summers, A. Whiteford and K.-D. Zastrow. **Complex Spectra in Fusion Plasmas.** *Physica Scripta*, T120:19–29, January 2005.
- [69] V. A. Evtikhin, I. E. Lyublinskij, A. V. Vertkov, V. I. Pistunovich, V. A. Pozharov, D. Yu Prokhorov, L. G. Golubchikov and V. M. Koryavin. **The liquid lithium fusion reactor.** *Fusion energy 1996. V. 3. Proceedings of the 16. international conference*, 1997.
- [70] V. A. Evtikhin, I. E. Lyublinski, A. V. Vertkov, S. V. Mirnov and V. B. Lazarev. **Technological aspects of lithium capillary-pore systems application in tokamak device.** *Fusion Engineering and Design*, 56-57:363–367, October 2001.
- [71] I. E. Lyublinski and A. V. Vertkov. **Experience and technical issues of liquid lithium application as plasma facing material in tokamaks.** *Fusion Engineering and Design*, 85(6):924–929, November 2010.

- [72] J. T. Hogan, C. E. Bush and C. H. Skinner. **Lithium effects in plasmas. Report on the Workshop held at Princeton, New Jersey, United States of America, 17-18 October 1996.** *Nuclear Fusion*, 37(5):705–711, 1997.
- [73] A. Kramida, Yu. Ralchenko, J. Reader and NIST ASD Team, 2020. **NIST Atomic Spectra Database** (ver. 5.8), [Online]. Available: [2021, September 29]. National Institute of Standards and Technology, Gaithersburg, MD.
- [74] W. Seim, A. Muller, I. Wirkner-Bott and E. Salzborn. **Electron capture by Li^{i+} ($i=2,3$), N^{i+} and Ne^{i+} ($i=2,3,4,5$) ions from atomic hydrogen.** *Journal of Physics B: Atomic and Molecular Physics (1968-1987)*, 14(18):3475, September 1981.
- [75] M. B. Shah, T. V. Goffe and H. B. Gilbody. **Electron capture and loss by fast lithium ions in H and H_2 .** *Journal of Physics B: Atomic and Molecular Physics*, 11(7):L233–L236, April 1978.
- [76] W Fritsch and C. D. Lin. **Comment on "atomic-basis calculations for the two-electron system $\text{Li}^{2+}\text{-H}$ ".** *Physics Letters A*, 127(8):425–426, March 1988.
- [77] L. F. Errea, L. Mendez, A. Riera, M. Yáñez, J. Hanssen, C. Harel and A. Salin. **Charge exchange in $\text{Li}^{2+}(1s) + \text{H}(1s)$ collisions. a molecular approach including two-electron translation factors.** *Journal de Physique*, 46(5):719–726, May 1985.
- [78] L. L. Yan, L. Liu, J. G. Wang, R. K. Janev and R. J. Buenker. **Electron capture processes in $\text{Li}^{2+} + \text{H}$ collisions.** *The European Physical Journal D*, 69(1):26, January 2015.
- [79] L. Liu, X. Y. Li, J. G. Wang and R. K. Janev. **Cross sections for electron capture and excitation in collisions of Li^q+ ($q=1, 2, 3$) with atomic hydrogen.** *Physics of Plasmas*, 21(6):062513, June 2014.
- [80] A. L. Ford, J. F. Reading and R. L. Becker. **Coupled-channel calculations of ionisation and charge transfer in $\text{p}+\text{Li}^{+,2+}$ and transfer in $\text{Li}^{2+,3+}+\text{H}(1s)$ collisions.** *Journal of Physics B: Atomic and Molecular Physics (1968-1987)*, 15(18):3257, September 1982.
- [81] D. S. F. Crothers and N. R. Todd. **One-electron capture by fast multiply charged ions in H: q^3 scaling.** *Journal of Physics B: Atomic and Molecular Physics*, 13(11):2277–2294, June 1980.

- [82] M. Purkait. Classical/quantum correspondence in state selective charge transfer and ionization cross-sections for Li^{q+} ($q=1-3$) ions with neutral hydrogen. *Nuclear Instruments and Methods in Physics Research Section B: Beam Interactions with Materials and Atoms*, 207(2):101–106, June 2003.
- [83] N. Bohr and J. Lindhard. On the properties of a gas of charged particles. *K. Dan. Vidensk. Selsk. Mat.-Fys. Medd*, 27(7), 1954.
- [84] M. R. C. McDowell and J. P. Coleman. *Introduction to the theory of ion-atom collisions*. North-Holland Pub. Co., Amsterdam, 1970. OCLC: 96092.
- [85] A. Szabo and N. S. Ostlund. *Modern Quantum Chemistry: Introduction to Advanced Electronic Structure Theory*. Dover Publications, 1996.
- [86] C. A. Ramirez and R. D. Rivarola. Electron excitation of hydrogenic targets in collisions with ions or atoms. *Journal of Physics B: Atomic, Molecular and Optical Physics*, 26(21):3835–3846, November 1993.
- [87] J. P. Hansen, L. Kocbach, S. A. Synnes, J. B. Wang and A. Dubois. Origin of the structures in the excitation cross sections in ion-atom collisions. *Phys. Rev. A*, 57:R4086–R4089, Jun 1998.
- [88] A. Müller. Electron-ion collisions: Fundamental processes in the focus of applied research. In Ennio Arimondo, Paul R. Berman and Chun C. Lin, editors, *Advances In Atomic, Molecular and Optical Physics*, volume 55, pages 293–417. Academic Press, January 2008.
- [89] N. Stolterfoht, R. D. DuBois and R. D. Rivarola. *Electron Emission in Heavy Ion-Atom Collisions*. Springer Series on Atomic, Optical and Plasma Physics. Springer-Verlag, Berlin Heidelberg, 1997.
- [90] R. K. Janev and H. Winter. State-selective electron capture in atom-highly charged ion collisions. *Physics Reports*, 117(5):265–387, January 1985.
- [91] W. G. Graham, W. Fritsch, Y. Hahn and J. A. Tanis, editors. *Recombination of Atomic Ions*. Nato Science Series B:. Springer US, 1992.
- [92] T. J. M. Zouros. Resonant Transfer and Excitation Associated with Auger Electron Emission. In W. G. Graham, W. Fritsch, Y. Hahn and J. A.

- Tanis, editors, *Recombination of Atomic Ions*, NATO ASI Series, pages 271–300. Springer US, Boston, MA, 1992.
- [93] E. P. Benis, I. Madesis, A. Laoutaris, S. Nikolaou, A. Dubois, T. W. Gorczyca and T. J. M. Zouros. Population of the states in collisions of mixed-state ($1s^2\ ^1S$, $1s2s\ ^3S$) B^{3+} and C^{4+} ion beams with He and H_2 targets. *X-Ray Spectrometry*, 49(1):54–59, 2020.
- [94] J. A. Tanis. Electron transfer and projectile excitation in single collisions. *Nuclear Instruments and Methods in Physics Research Section A: Accelerators, Spectrometers, Detectors and Associated Equipment*, 262(1):52–61, December 1987.
- [95] J. A. Tanis. Interactions involving two electrons in ion-atom collisions. *Nuclear Instruments and Methods in Physics Research Section B: Beam Interactions with Materials and Atoms*, 40-41:70–76, April 1989.
- [96] J. M. Feagin, J. S. Briggs and T. M. Reeves. Simultaneous charge transfer and excitation. *Journal of Physics B: Atomic and Molecular Physics*, 17(6):1057–1068, March 1984.
- [97] N. Stolterfoht. Dielectronic processes and electron correlation in energetic ion-atom collisions. *Nuclear Instruments and Methods in Physics Research Section B: Beam Interactions with Materials and Atoms*, 53(4):477–492, April 1991.
- [98] W. Fritsch and C. D. Lin. Analysis of Electron Correlation in Simultaneous Electron Transfer and Excitation in Atomic Collisions. *Physical Review Letters*, 61(6):690–693, August 1988.
- [99] H. Bachau, R. Gayet, J. Hanssen and A. Zerarka. Transfer and excitation in ion-atom collisions at high impact velocities: a unified continuum distorted wave treatment of resonant and non-resonant modes in a four-body approach. II. Application to the collision $S^{15+}(1s)+H(1s)$. *Journal of Physics B: Atomic, Molecular and Optical Physics*, 25(4):839–852, February 1992.
- [100] R. Gayet, J. Hanssen and L. Jacqui. Transfer and excitation in ion-atom collisions at high impact velocities. III. Application of the CDW-4B theory to an almost symmetrical system: He^+-He . *Journal of Physics B: Atomic, Molecular and Optical Physics*, 28(11):2193–2208, June 1995.

- [101] R. Gayet, J. Hanssen, L. Jacqui and M. A. Ourdane. **Transfer and excitation in ion - atom collisions at high impact velocities: IV. Application of the CDW - 4B theory to an almost symmetrical system: He⁺-He.** *Journal of Physics B: Atomic, Molecular and Optical Physics*, 30(9):2209–2219, May 1997.
- [102] T. J. M. Zouros, D. Schneider and N. Stolterfoht. **State-selective observation of resonant and non-resonant transfer-excitation in 50-500 keV ³He⁺+H₂ collisions.** *Journal of Physics B: Atomic, Molecular and Optical Physics*, 21(21):L671–L676, November 1988.
- [103] A. Itoh, T. J. M. Zouros, D. Schneider, U. Stettner, W. Zeitz and N. Stolterfoht. **Transfer excitation in He⁺+He collisions studied by 0 degrees electron spectroscopy.** *Journal of Physics B: Atomic and Molecular Physics*, 18(23):4581–4587, December 1985.
- [104] N. Stolterfoht. **Dielectronic processes and electron correlation in energetic ion-atom collisions.** *Nuclear Instruments and Methods in Physics Research Section B: Beam Interactions with Materials and Atoms*, 53(4):477–492, April 1991.
- [105] D. Brandt. **A simple classical model for the impact parameter dependence of electron capture.** *Nuclear Instruments and Methods in Physics Research*, 214(1):93–96, August 1983.
- [106] J. K. Swenson, Y. Yamazaki, P. D. Miller, H. F. Krause, P. F. Dittner, P. L. Pepmiller, S. Datz and N. Stolterfoht. **Observation of Resonant Transfer and Excitation to Specific LS-Coupled States in O⁵⁺ + He Collisions by High-Resolution, 0° Auger-Electron Spectroscopy.** *Physical Review Letters*, 57(24):3042–3045, December 1986.
- [107] J. M. Feagin, J. S. Briggs and T. M. Reeves. **Simultaneous charge transfer and excitation.** *Journal of Physics B: Atomic and Molecular Physics*, 17(6):1057–1068, March 1984.
- [108] M. Clark, D. Brandt, J. K. Swenson and S. M. Shafroth. **Nonresonant Electron Transfer and Projectile K-Electron Excitation in Ion-Atom Collisions.** *Physical Review Letters*, 54(6):544–546, February 1985.
- [109] D. H. Lee, P. Richard, J. M. Sanders, T. J. M. Zouros, J. L. Shinpaugh and S. L. Varghese. **Electron capture and excitation studied by state-resolved KLL Auger measurement in 0.25-2 MeV/u F⁷⁺(1s² ¹S, 1s2s ³S) + H₂/He**

- collisions. *Nuclear Instruments and Methods in Physics Research Section B: Beam Interactions with Materials and Atoms*, 56-57:99–103, May 1991.
- [110] E. P. Benis, I. Madesis, A. Laoutaris, S. N. and T. J. M. Zouros. **Mixed-State Ionic Beams: An Effective Tool for Collision Dynamics Investigations.** *Atoms*, 6(4):66, December 2018.
- [111] M. H. Chen, B. Crasemann and H. Mark. **Deexcitation of light Li-like ions in the $1s2s2p$ state.** *Phys. Rev. A*, 27:544–547, Jan 1983.
- [112] D. Schneider, R. Bruch, W. H. E. Schwar, T. C. Chang and C. F. Moore. **Identifications of Auger spectra from 2-MeV foil-excited carbon ions.** *Phys. Rev. A*, 15:926–934, Mar 1977.
- [113] M. H. Chen. **Dielectronic satellite spectra for He-like ions.** *Atomic Data and Nuclear Data Tables*, 34(2):301–356, March 1986.
- [114] J. M. Anthony, S. M. Shafroth, Malika Benhenni, E. N. Strait, T. Zouros, L. Hendrick and D. Peterson. **PRODUCTION OF DOUBLY CORE EXCITED CONFIGURATIONS IN C^{4+} PROJECTILES THROUGH RESONANT TRANSFER EXCITATION.** *Journal de Physique Colloques*, 1987, 48 (C9), pp.C9-301-C9-306.
- [115] D. H. Lee, P. Richard, J. M. Sanders, T. J. M. Zouros, J. L. Shinpaugh and S. L. Varghese. **KKL resonant transfer excitation to $F^{6+}(1s2l2l')$ intermediate states.** *Physical Review A*, 44(3):1636–1643, August 1991.
- [116] J. W. Gao, Y. Wu, J. G. Wang, A. Dubois and N. Sisourat. **Double Electron Capture in $H^+ + H^-$ Collisions.** *Physical Review Letters*, 122(9):093402, March 2019.
- [117] T. J. M. Zouros, D. H. Lee and P. Richard. **Projectile $1s \rightarrow 2p$ excitation due to electron-electron interaction in collisions of O^{5+} and F^{6+} ions with H_2 and He targets.** *Physical Review Letters*, 62(19):2261–2264, May 1989.
- [118] W. Wu, K. L. Wong, R. Ali, C. Y. Chen, C. L. Cocke, V. Frohne, J. P. Giese, M. Raphaelian, B. Walch, R. Dörner, V. Mergel, H. Schmidt-Böcking and W. E. Meyerhof. **Experimental separation of electron-electron and electron-nuclear contributions to ionization of fast hydrogenlike ions colliding with He.** *Physical Review Letters*, 72(20):3170–3173, May 1994.

- [119] H. Kollmus, R. Moshhammer, R. E. Olson, S. Hagmann, M. Schulz and J. Ullrich. **Simultaneous Projectile-Target Ionization: A Novel Approach to $(e, 2e)$ Experiments on Ions.** *Physical Review Letters*, 88(10):103202, February 2002.
- [120] M. Benhenni, S. Shafroth, J. Swenson, M. Schulz, J. Giese, H. Schöne, C. Vane, P. Dittner and S. Datz. **Angular distribution of Auger electrons emitted through the resonant transfer and excitation process following $O^{5+}+He$ collisions.** *Physical Review Letters*, 65(15):1849–1852, October 1990.
- [121] M. Benhenni, S. M. Shafroth and J. K. Swenson. **Alignment effects in fast ion-atom collisions.** *Nuclear Instruments and Methods in Physics Research Section B: Beam Interactions with Materials and Atoms*, 86(1):28–37, March 1994.
- [122] I. Madesis, A. Laoutaris, T. J. M. Zouros, S. Nanos and E. P. Benis. **Projectile electron spectroscopy and new answers to old questions: Latest results at the new atomic physics beamline in Demokritos, Athens.** In *State-of-the-Art Reviews on Energetic Ion-Atom and Ion-Molecule Collisions*, volume Volume 2 of *Interdisciplinary Research on Particle Collisions and Quantitative Spectroscopy*, pages 1–31. WORLD SCIENTIFIC, August 2019.
- [123] E. P. Benis and T. J. M. Zouros. **Determination of the $1s2l2l'$ state production ratios ${}^4P^\circ/{}^2P$, ${}^2D^\circ/{}^2P$ and ${}^2P_+/{}^2P_-$ from fast $(1s^2, 1s2s^3S)$ mixed-state he-like ion beams in collisions with H_2 targets.** *Journal of Physics B: Atomic, Molecular and Optical Physics*, 49(23):235202, November 2016.
- [124] I. Madesis, A. Laoutaris, T. J. M. Zouros, E. P. Benis, J. W. Gao and A. Dubois. **Pauli Shielding and Breakdown of Spin Statistics in Multi-electron Multi-Open-Shell Dynamical Atomic Systems.** *Physical Review Letters*, 124(11):113401, March 2020.
- [125] T. J. M. Zouros, C. P. Bhalla, D. H. Lee and P. Richard. **Effects of alignment and interference in resonant transfer and excitation for F^{6+} and O^{5+} collisions with H_2 in 0° Auger measurements.** *Physical Review A*, 42(1):678–681, July 1990.

- [126] T. J. M. Zouros, B. Sulik, L. Gulyás, and K. Tökési. **Selective enhancement of $1s2s2p\ ^4P_J$ metastable states populated by cascades in single-electron transfer collisions of $F^{7+}(1s^2 / 1s2s\ ^3S)$ ions with he and H_2 targets.** *Phys. Rev. A*, 77:050701, May 2008.
- [127] C. Can, T. W. Tunnell and C. P. Bhalla. **K-shell Auger rates for multiply-ionized atoms. II. Fluorine.** *Journal of Electron Spectroscopy and Related Phenomena*, 27(1):75–81, January 1982.
- [128] D. Brandt. **Resonant transfer and excitation in ion-atom collisions.** *Phys. Rev. A*, 27:1314–1318, Mar 1983.
- [129] K. Ishii, A. Itoh, and K. Okuno. **Electron-capture cross sections of multiply charged slow ions of carbon, nitrogen, and oxygen in He.** *Physical Review A*, 70(4):042716, Oct 2004.
- [130] G. Laurent, M. Tarisien, X. Fléchar, P. Jardin, L. Guillaume, P. Sobocinski, L. Adoui, A. Bordenave-Montesquieu, D. Bordenave-Montesquieu, J.-Y. Chesnel, F. Frémont, D. Hennecart, E. Liénard, L. Maunoury, P. Moretto-Capelle, and A. Cassimi. **Coincident auger electron and recoil ion momentum spectroscopy for low-energy ion–atom collisions.** *Nuclear Instruments and Methods in Physics Research Section B: Beam Interactions with Materials and Atoms*, 205:546–549, 2003. 11th International Conference on the Physics of Highly Charged Ions.
- [131] N. Stolterfoht, K. Sommer, D.C. Griffin, C.C. Havener, M.S. Huq, R.A. Phaneuf, J.K. Swenson, and F.W. Meyer. **Studies of electron correlation effects in multicharged-ion-atom collisions involving double capture.** *Nuclear Instruments and Methods in Physics Research Section B: Beam Interactions with Materials and Atoms*, 40-41:28–32, 1989.
- [132] W. Fritsch and C. D. Lin. **Atomic-orbital expansion study for the (quasi-) two-electron collision system $O^{6+} + He$ and $C^{6+} + He$.** *Journal of Physics B: Atomic and Molecular Physics*, 19(17):2683–2694, sep 1986.
- [133] J. A. Tanis, D. Schneider, S. Chantrenne, M. H. Prior, R. Herrmann, R. Hutton, and G. Schiwietz. **Origin of cusp electrons in slow ($v \sim 0.4$ a.u.) $O^{6+} + He$ collisions.** *Phys. Rev. A*, 42:5776–5779, Nov 1990.
- [134] J. A. Tanis, E. M. Bernstein, M. W. Clark, S. M. Ferguson, and R. N. Price. **Target ionization accompanied by projectile electron loss in fast $O^{6,7+} + He$ collisions.** *Phys. Rev. A*, 43:4723–4726, May 1991.

- [135] T. R. Dillingham, J. Newcomb, James Hall, Philip L. Pepmiller, and Patrick Richard. **Projectile k -auger-electron production by bare, one-, and two-electron ions.** *Phys. Rev. A*, 29:3029–3038, Jun 1984.
- [136] V. A. Zaytsev, I. A. Maltsev, I. I. Tupitsyn, V. M. Shabaev and V. Y. Ivanov. **Complex rotated relativistic configuration-interaction calculations of $1s2l2l'$ states in O^{5+} ion.** *Optics and Spectroscopy*, 128(3):307–314, March 2020.
- [137] A. Laoutaris, I. Madesis, E. P. Benis and T. J. M. Zouros. **Production of $C^{4+}(2s2p\ ^3P)$ hollow states in collisions of 6-18 MeV $C^{4+}(1s^2, 1s2s\ ^3S)$ mixed-state beams with gas targets.** *HNPS Advances in Nuclear Physics*, 26(0):133–138, April 2019.
- [138] S. Lepp and R. McCray. **X-ray sources in molecular clouds.** *The Astrophysical Journal*, 269:560, June 1983.
- [139] R. K. Janev, T. Kato and J. G. Wang. **Catalytic mechanism of divertor plasma recombination provided by hydrocarbon impurities.** *Physics of Plasmas*, 7(11):4364–4367, November 2000.
- [140] S. I. Krasheninnikov, A. Yu. Pigarov and D. J. Sigmar. **Plasma recombination and divertor detachment.** *Physics Letters A*, 214(5):285–291, May 1996.
- [141] W. S. Melo, M. M. Sant’Anna, A. C. F. Santos, G.M. Sigaud and E. C. Montenegro. **Electron loss and single and double capture of C^{3+} and O^{5+} ions in collisions with noble gases.** *Physical Review A*, 60(2):1124–1134, Aug 1999.
- [142] Y. Wu, Y. Y. Qi, J. Yan, J. G. Wang, Y. Li, R. J. Buenker, D. Kato and P. S. Krstic. **Low-energy electron capture in collisions of C^{3+} with He.** *Physical Review A*, 80(2):022715, August 2009.
- [143] A. C. F. Santos, G. M. Sigaud, W. S. Melo, M. M. Sant’Anna and E. C. Montenegro. **Absolute cross sections for electron loss, electron capture, and multiple ionization in collisions of C^{3+} with noble gases.** *Physical Review A*, 82(1):012704, July 2010.
- [144] L. D. Gardner, J. E. Bayfield, P.M. Koch, I. A. Sellin, D. J. Pegg, R. S. Peterson, M. L. Mallory and D. H. Crandall. **Electron-capture collisions at keV energies of boron and other multiply charged ions with atoms and molecules. I. Ar, H_2 , and He.** *Physical Review A*, 20(3):766–778, Sep 1979.

-
- [145] T. Iwai, Y. Kaneko, M. Kimura, N. Kobayashi, S. Ohtani, K. Okuno, S. Takagi, H. Tawara and S. Tsurubuchi. **Cross sections for one-electron capture by highly stripped ions of B, C, N, O, F, Ne and S from He below 1 keV/amu.** *Physical Review A*, 26(1):105–115, July 1982.
- [146] M. Lennon, R. W. McCullough and H. B. Gilbody. **State-selective electron capture by C^{2+} , C^{3+} , N^{2+} and Ar^{2+} ions in rare gases.** 16(12):2191–2204, June 1983.
- [147] X. Zhu, Private communication (2021)
- [148] J. P. Hansen, A. Dubois and S.E. Nielsen. **Partial cross sections and correlation effects in B^{3+} - He collisions.** *Physical Review A*, 45(1):184–189, Jan 1992.